UNIVERSITY OF SOUTHAMPTON

FACULTY OF PHYSICAL AND APPLIED SCIENCES

Physics and Astronomy

Engineering Nonlinearities in Organic and Hybrid Microcavities.

by

Niccolo Somaschi

Thesis for the degree of Doctor of Philosophy

January 2014

Ad Ambrogio e tutti coloro che lo hanno amato.

UNIVERSITY OF SOUTHAMPTON

ABSTRACT

FACULTY OF PHYSICAL AND APPLIED SCIENCES
Physics and Astronomy

Doctor of Philosophy

ENGINEERING NONLINEARITIES IN ORGANIC AND HYBRID MICROCAVITIES.

by Niccolo Somaschi

Semiconductor microcavities represent a rich playground for the investigation and exploitation of fundamental light–matter interaction as well as opto–electronic devices. Due to strong interaction of confined photons with electronic excitations new quasiparticles are formed, known as exciton–polaritons. These new eigenstates play a key role in a various number of intriguing effects like Bose-Einstein condensation and superfluidity due to their light–matter duality which unifies at the same time small effective mass and strong inter–particles interaction. Meanwhile, research achievements in the study of organic light emitting diodes and organic trasistors combined with strong advancements of the fabrication technologies has propelled the organic photonic and electronic field.

In the present thesis the physics of organic microcavities is explored with particular attention at the limiting factors which prevent from the observation of cooperative nonlinear phenomena. Such structural and material issues are addressed by following new engineeristic approaches. The inclusion of different organic dyes in the cavity active region is demonstrated to enhance polariton population density by direct intracavity pumping or either provide new efficient channels for particles relaxation.
Inspired by a similar design, an hybrid organic–inorganic microcavity which exploits coupling of organic with inorganic quantum well excitons (Frenkel and Wannier–Mott) in a light emitting diode scheme is presented. Within this system, the optical cavity mode simultaneously couples to both excitonic transitions for the formation of mixed polariton states. The new bosonic eigenstates which arise from photon–mediated hybridiazation of Frenkel and Wannier-Mott excitons are predicted to exhibit large radius, small saturation density and large oscillator strength. Results from the optical characterization enlighten the enhancement of nonlinear properties of such hybrid polaritons while observation of strong coupling regime under electrical injection suggests the possibility for an effective exploitation of such unique polaritonic features in a electro–optic device.

Acknowledgements

Piu' di tutti e sopra tutti, questo e stato possibile grazie a Claudio e Franca.

Declaration of Authorship

I, Niccolo Somaschi , declare that the thesis entitled *Engineering Nonlinearities in Organic and Hybrid Microcavities.* and the work presented in the thesis are both my own, and have been generated by me as the result of my own original research. I confirm that:

- this work was done wholly or mainly while in candidature for a research degree at this University;
- where any part of this thesis has previously been submitted for a degree or any other qualification at this University or any other institution, this has been clearly stated;
- where I have consulted the published work of others, this is always clearly attributed;
- where I have quoted from the work of others, the source is always given. With the exception of such quotations, this thesis is entirely my own work;
- I have acknowledged all main sources of help;
- where the thesis is based on work done by myself jointly with others, I have made clear exactly what was done by others and what I have contributed myself;
- parts of this work have been published as: [1]

Signed:.....

Date:.....

Contents

List of Figures

List of Tables

List of Publications

- *Ultrafast Polariton Population Build-up Mediated by Molecular Phonons in Organic Microcavities.* Niccolo Somaschi, Leonidas Mouchliadis, Dave Coles, Ilias Perakis, David G. Lidzey, Pavlos. G. Lagoudakis and Pavlos G. Savvidis. *Applied Physics Letter* **99**, 143303 (2011)

- *Characterizing the Electroluminescence Emission from a Strongly-coupled Organic Semiconductor Microcavity LED.* Nikos Christogiannis, Niccolo Somaschi, Paolo Michetti, Dave Coles, Pavlos G. Lagoudakis and David G. Lidzey. *Advanced Optical Materials*, **1**, 503 (2013)

- *Superlinear Polariton Emission of Hybrid Organic-Inorganic Microcavities.* Niccolo Somaschi, Simos Tsintzos, Dave Coles, David G. Lidzey, Zacharia Hatzopoulos, Pavlos G. Lagoudakis and Pavlos G. Savvidis. UNPUBLISHED.

- *Polariton Optical Nonlinearities and Reverse Saturable Absorption in Disordered J-aggregate Cyanine Dyes.* Niccolo Somaschi, Leonidas Mouchliadis, Noel Healy, Anna C. Peacock, Ilias Perakis, Pavlos G. Savvidis and Pavlos. G. Lagoudakis. UNPUBLISHED.

- *Energetic Relaxation in a Microcavity Containing Two Strongly–coupled J–aggregated Cyanine Dyes.* Dave Coles, Niccolo Somaschi, Caspar Clark, Pavlos G. Lagoudakis, Pavlos G. Savvidis and D. G. Lidzey. UNPUBLISHED.

- *Polariton Lasing in a Strongly Coupled Hybrid Dielectric Mirror Semiconductor Microcavity.* Panos Tsotsis, Peter Eldridge, Simos Tsintzos, Niccolo Somaschi, Zacharias Hatzopoulos, Pavlos G. Lagoudakis and Pavlos G. Savvidis. UNPUBLISHED.

Abbreviations

DBR	**D**istributed **B**ragg **R**eflector
BEC	**B**ose-**E**instein **C**ondensation
CCD	**C**harge **C**oupled **D**evice
EM	**E**lectro**M**agnetic field
MC	**M**icro**C**avity
LP/MP/UP	**L**ower / **M**iddle / **U**pper **P**olariton
VCSEL	**V**ertical **C**avity **S**urface **E**mitting **L**aser
GaAs	Gallium-arsenide
CdTe	Cadmium-telluride
GaN	Gallium-nitride
SiO_2	Silicon-dioxide
Ta_2O_5	Tantalum-pentoxide

1 Introduction

From photosyntesis to respiration, processes of light absoprtion, energy transformation and its consecutive transfer represent elementary and essential reactions that recur in any biological living system. As introduced in early 1931 by Yakov Frenkel [4], electronic excitation is regarded as the first step in the process of light absorption and as the basic medium that allows energy to be shared between different molecules without any request of direct coupling. Being electron and hole pairs, excitons do not contribute to electrical transport because they carry no charge. Nevertheless, their mobility is responsible for any energy transport mechanism, fundamental not only in solids (semiconductor and insulators) but also in meso and nanoscopic systems like molecular cyanine aggregates [5] and complex molecules in photosynthetic systems of bacteria and higher plants where excitons are responsible for light harvesting [6]. As such, depending on the compounds where they reside in, exciton particles can show different properties (interaction strength and size) which therefore relate to the optical response of those materials. The intensity of the physical effects which arise when excitons interact and exchange energy with light chages accordingly. Cooperative spontaneous emission [7–9], optical nonlinearities [10, 11] and optical bistability [12] can be studied in both organic and inorganic semiconductors but with distinctive and peculiar behaviours in each case. Although photons lie on the complete opposite extreme because of their bosonic nature and absence of mass, under particular conditions they can interact and mix with excitons to form a new and unique phase where excitonic and photonic behaviours cohexist at the same time.

General purpose of this thesis is the engineering of optoelectronic devices based on organic active layers which exploit light and matter interaction for the observation of strong coherent emission and nonlinear phenomena. Particularly, photonic devices which embed J–aggreagates cyanine dyes are described, fabricated and characterized; their potential for use as active medium in laser devices is exploited by means of engineering designs which also comprehend the implementation of inorganic semiconductors.

The field of optics and photonics have increasingly gained attention from the research community especially since the invention of the laser occured in the 1960s. In parallel, development and discovery of new phenomena and technologies which encompass different scientific areas (from medicine to biology and physics) have followed the expansion of the field. As part of this process, research on organic semiconductors which started in the late 1950s with studies on electrical conductivity of polymers has been redirected to optics and photonics in the 1970s with the implementation of solution based dyes as gain medium in laser devices. Such laser systems underwent a fast improvement which finally led to their commercialization due to remarkable quantum efficiencies and stability accompanied by the possibility to cover the visible spectrum [13,14]. Subsequently, during the 1980s and early 1990s, a big technological step was achieved with the development of organic light emitting diodes (OLEDs) [15,16]. In those systems organic compounds originally synthetized for laser dyes have found a commercial application in the solid state as thin films, employed in OLED devices both as electrical transport layers and light emitting layers [17]. Following the expansion of the new technology, mechanism of exciton recombination and transport (Forster resonant energy transfer, FRET) and in general physics of Frenkel (organic) type excitons has been furthermore investigated, understood and expanded aimed at the efficiency improvement of those devices [18]. On the other hand, inorganic semiconductors were succesfully implemented in one of the first and most groundbreaking discovery of the century, the transistor, presented in 1947 by William Shockley, John Bardeen and Walter Brattain. After that moment, a steadily improvement of processing technologies occurred and inorganic semiconductors started to assume the major role in the semiconductor industry as basic compounds for commercial devices. Specifically, through molecular beam epitaxy (MBE) which enables ultrapure, precise–thickness growth of alternating inorganic semiconductor layers we assisted to a constant downscale of the device size and consequently to an esponential growth of the transistor number implemented in a integrated circuit [19]. This represented the birth of the digital age and turning point for the revolution of the information technology [20–22].

During the 1992 a new phase of research in photonic and more generally in solid state physics was triggered by the first experimental evidence of strong light matter coupling. Starting from the design of a VCSEL laser [23] and motivated by the theoretical concept of coupling between atoms and cavities [24], Weisbuch *et al.* [25] demonstrated the possibility to form new states, the so called polaritons, by enclosing a stack of inorganic semiconductors layers in a planar cavity, i.e. between two highly reflective mirrors. The characteristic reflectivity spectra of the optical cavity mode defined by a single dip in a frequency wide high reflectance region was replaced by a doublet, mark of the strong interaction of the excitonic transition with the electric field across the structure. Furthermore, the angle resolved excitation/detection scheme implemented for the purpose showed the great ease of accessibility to the entire polariton energy dispersions opening

new prospective and practical means for the investigation and exploitation of the new physics just discovered.

Not much time passed before many others reasearch groups both theoretically and experimentally, proved the extraordinary potentiality of the system. Because to their light–matter duality, theoretical possibility for polariton to form a Bose–Einstein condensate (BEC) acted as input for the investigation of their bosonic character into various forms. First exampe was the innovative concept proposed by Imamoglou and coworkers [26] which enlighten the possibility to exploit coherent light emission from a nonequilibrium condense state of exciton—polaritons for the realization of a functional "polariton laser" device. Just a couple of years later bosonic nature of exciton–polaritons was definetely ascertained by Savvidis [27] and Baumberg [28] who observed stimulated scattering of polariton particles in a pump–probe experiment. Besides, practical evidence of Bose–Einstein condensation of polariton was reported firstly in 2006 by Kasprzak *et al.* and subsequently followed by many others [29–31]. These fundamental achievements triggered and opened the way to new prospective for realization of practical devices as well as fundamental studies of the matter [32–35]. In between all, it is worth mentioning the concept of superfluidity [36, 37], closely connected to Bose–Einstein condensation and subject of constant investigation from various directions [38–41].
Common characteristic of all these systems (II-VI CdTe and III-V GaAs inorganic semiconductor based microcavities), with the only exception of GaN semiconductors, is the cryogenic operation temperature required for the observation of strong coupling regime. Weak interaction strength which bound together electrons and holes in Wannier–Mott (inorganic) excitons limits the operation temperature to that range which avoid dissociation of excitons due to the thermal energy. For this reason organic semiconductors started to gain increasing consideration from the research comunity, as alternative platform for polariton microcavities where strong coupling regime can be achieved at room temperature. The motivation is due to the large binding energy characteristic of organic Frenkel type excitons, which arises from their strong molecular localization and that is considerably higher than the thermal energy at room temperature (k_BT ≈26meV at T=300K).

The first demonstration of strong coupling at room temperature was presented by Lidzey *et al.* [42] who fabricated a planar microcavity whose active medium was made by a thin film of organic dye. Similar to the work of Weisbuch *et al.* [25], Lidzey measured reflectivity spectra at various angles where the appearance of a doublet undoubtedly proved the formation of polariton particles in a clear strong coupling regime. Since then, the polariton field showed an even further expansion pointed towards the progress of microcavity quality and especially of the fabrication of organic polariton devices. Strong motivation and effort are still underway and this thesis is a part of it.
Under the previous considerations, it is important and interesting to underline that the first demonstration of strong coupling regime under electrical excitation was achieved

with an organic based microcavity structure. Tischler and coworkers [43] fabricated a full organic cavity LED based on the well developed design of a light–emitting–diode (transport and emitting layers), which was embedded in between two mirrors to form the active region of the cavity. Thickness and layers positions were chosen in such a way to allow for efficient electrical injection and recombination as well as exciton–cavity mode strong coupling. The fact that such important result was achieved with a microcavity device based on organic materials three years before the equivalent inorganic microcavity LED [44] enlighten the suitability of organic compounds for the realization of functional polariton devices. The reason which motivated this success has to be found in the ease of processing, room temperature operation and furthermore to the possibility to chemically design the compound to match particular wavelengths in the entire visible spectrum.
Following this motivating achievement, advancement of the processing technologies permited to improve dramatically the quality of organic based microcavities. If the first structures were fabricated by using metallic mirrors, the possibility to deposit dielectric distributed Bragg reflectors with ultra high reflectance allowed for the achievement of stronger and more define polaritonic emission which also gave the oppurtunity for a more deep investigation of polariton mechanisms and properties [1, 45–47]. Nevertheless, the actual organic microcavities suffer of different limitations which are especially related to the nature of the active layer: structural inhomogeneity and molecular disorder of the organic dyes (J–aggregate cyanine dyes) together with difficulties in the efficient excitation of the microcavity system which also results in photobleaching issues. An indication of these problematics is suggested by the fact that the only report of polariton nonlinear emission in a organic microcavity was achieved by implementing a molecular crystalline structure as active layer [48].

In the work we are here presenting, material problems and design obstacles are addressed with the aim to enhance device quality towards the highly advance technological state of microcavities based on inorganic semiconductors. Strong coupling regime in J–aggregate microcavities is investigated by mean of various spectroscopic techniques which enlighten both polariton and organic compound properties.
The experimental analysis begins in chapter 3 with investigation of intrinsic optical nonlinearities of a J–aggregate cyanine dye which findings are interpreted and supported by mean of a theoretical description. Subsequently, the organic dye is embedded in a microcavity structure and characterized. Polariton emission is spectrally and time resolved for a complete and detailed view on polariton formation and relaxation dynamics. The important contribution of molecular vibrations is enlighten and their effect on the relaxation mechanism is reproduced with a theoretical simulation of the full microcavity polariton system.
The results from the investigation of nonlinearities and optical/time resolved characterization of J–aggregate dye in a film and in a microcavity underline once more how the intrinsic nature of the compound and particular structural design limit the achievement

of high polariton population densities required for the occurrence of any nonlinear process. To overcome these limitations different cavity designs are implemented. At first, the realization of two different microcavity structures which separately implement alternative pumping schemes and introduce additional relaxation pathways that favourite condensation of polariton particles, are addressed. Description of sample fabrication, characterization and discussion of the observed improvements are all presented in chapter 4.

With the same aim but following a different route is developed chapter 5 where the issues related to organic compounds will be takled by considering the different approach proposed by Agranovich *et al.* [49,50]. In these pioneering studies it was predicted that the combination of organic and inorganic excitons in a unique cavity can lead to the formation of hybrid polaritons which combines favorable properties of both excitonic species. The theoretical concept expanded in the first part of the chapter, is then followed by a description of the fabrication steps which required fine combination of inorganic and organic semiconductor processing techniques. Characterization of each single element of the structure is presented to provide the basis for the complete analysis and description of the full device in the strong coupling regime. Subsequently, investigation of optical nonlinearities is pursued with direct comparison to the results obtained from the identical study of separate inorganic and organic microcavities. This new design structure is presented not only as a way to overcome organic microcavities limitations but to propose as well a platform where inorganic polariton nonlinearities are further more enhanced and where observation of additional interesting features, such as negative polariton dispersion (section 5.3.1) can be also exploited.
As a starting point, in the following chapter 2 the physics of planar microcavity structures will be described and the main characteristics and differences between organic and inorganic excitons introduced. This will lead to the concept of light–matter coupling and more specifically to a discussion of polariton particles in strongly coupled systems. Furthermore, detailed description of the experimental setup, designed and exploited along this work, will be presented in Appendix A (7).

2 Light and Matter Coupling

2.1 Introduction

Light–matter interaction in semiconductor microcavities which results, under defined conditions, in the formation of exciton–polaritons, will be theoretically described in the present chapter. Particularly, each component which participates in the process will be separately analysed. We will start with a description of planar microcavity structures and follow with a general introduction of the excitonic properties of the condensed matter. Organic and inorganic based microcavity systems will be studied along this work and for this reason, a description of both class of semiconductors is here presented to better understand the polariton physics and features which are driven by the intrinsic properties of each compound. Polariton formation mechanism and general properties of organic and inorganic exciton–polariton will be therefore highlighted in the final part of the chapter to permit a full comprehension of more complex processes presented and discussed further on in the thesis.

2.2 Semiconductor Planar Microcavities

The study of physical phenomena and exciton–polation properties performed in this work is based on the light confinement effect provided by Fabry-Perot planar microcavities, which represent the playground structure, i.e. basic element which recurs in every sample investigated.
A semiconductor planar microcavity can be described as a vertical structure containing thin slabs of semiconductor materials located between two highly reflective mirrors that usually consist of metallic films, $III-V$ type semiconductors or dielectric stacks tailored to form a so called *distributed Bragg reflectors*. These DBRs are multiple repeats of alternating pairs of materials characterized by high refractive index contrast. Modification of the thickness of such layers ($\lambda/4$) allows to frequency tailor the high reflectance

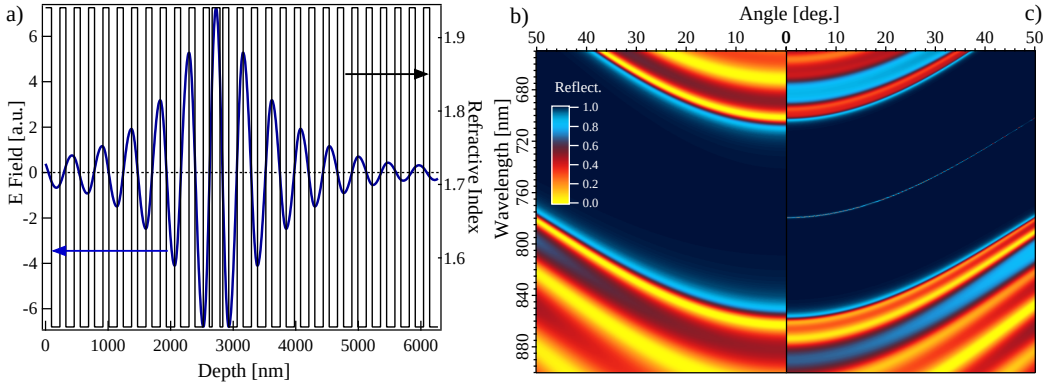

Figure 2.1: a) Electric field across the structure defined by refractive index values of the materials involved (SiO_2 and Ta_2O_5). Angle–resolved reflectance images of the bottom DBR (b) and empty microcavity structure (c) which displays in the stop band centre the parabolic dispersion of the cavity mode. The simulation of electric field and reflectivity was performed via transfer matrix method.

region, the so called stop band, around the wavelength λ of the exciton embedded in the cavity medium. Photon quantization in the vertical direction z (direction of growth) can be achieved in these Fabry–Perot resonators with resulting modification of the cavity photon dispersion, with respect to the photon in free space, according to $k_z L_{cav} = N\pi$, where L_{cav} is the effective length of the cavity chosen to be half–integer multiple of λ ($m\lambda/2$). Under these conditions, vertical confinement allows the cavity to possess an in–plane (parabolic) dispersion defined by the following:

$$E(k_{||}) = \frac{\hbar c}{n_{cav}} k_0 = \frac{\hbar c}{n_{cav}} \left[\left(\frac{N\pi}{L_{cav}} \right)^2 + k_{||}^2 \right]^{1/2} \tag{2.1}$$

where n_{cav} is the refractive index of the cavity medium and the total wave vector k_0 is such that $k_0^2 = k_z^2 + k_{xy}^2$ ($k_{xy} = k_{||}$). Model, design and study of these structures can be easily performed by using the standard Transfer Matrix approach [51] which is based on the calculation of the propagation of the electromagnetic field (EM) across the structure. An example of DBR reflectivity spectra and full cavity reflectance simulated with the transfer matrix method are presented in figure 2.1 and refer to the full dielectric cavity described in chapter 5. From position λ and cavity mode linewidth $\delta\lambda$ is possible to extract the overall microcavity quality factor Q ($Q = \lambda/\delta\lambda$) which directly relates to photon and hence, polariton lifetime: $\tau = \hbar/\delta\lambda$.

2.3 Organic and Inorganic Excitons

By definition, an exciton can be simply described as an interacting electron–hole pair which is bound by Coulomb force and generated by absorption of light or by relaxation

of free electrons and holes from high energy excited states. They are electrically neutral but due to their mobility they are responsible for any process which involves transport of energy. Accordingly to the electron–hole separation, which relates to the compound where they reside in, excitons are divided in Wannier–Mott [52] and Frenkel [4]. The first are commonly found in inorganic semiconductors while the second in organics. This distinction orginates from the competition of two distinctive processes: the electron–hole interaction strength and the hopping rate between molecules or atoms in the surroundings [53]. While overlap between electron and hole orbitals on the molecules in the proximity relates to the hopping rate, Coulomb interaction contrasts this motion by tighting electron and hole together in a limited space.

In the next sections we will specifically describe material properties and related excitonic features of organic J–aggregate cyanine dyes and inorganic semiconductor quantum wells, primary active compounds employed in organic and inorganic based microcavities.

2.3.1 Frenkel Excitons in J–aggregate Compounds

For the first time observed in alkali halides by Apker and Taft in 1950 [54], Frenkel type excitons are characterized by high binding energies (order of 0.1-1eV) and small electron–hole separation which is limited to one lattice constant (≈1nm). Under this condition, Coulomb interaction, which dominates over the hopping rate, is too strong to allow for a physical separation and therefore electrons and holes in Frenkel excitons occupy the same molecule. This molecular excitation is then represented by an electron on the lowest unoccupied molecular orbital (LUMO) and a hole on the highest occupied molecular orbital (HOMO) [2] strongly bound in such a way that their states appear as discrete levels below the continuum which describe free electrons/holes (absence of Coulomb force). Nevertheless, propagation of Frenkel excitons is still possible due to interaction of transition dipoles of individual molecular excitations. This can be seen as long–range energy transfer between neighbouring molecules which is also responsible for the formation of an excitonic band despite no occurence of charge overlap.

The concept of Frenkel excitations can be extended without loss of generality to molecular crystals, aggregates (both dimers and linear periodic chains involving N molecules) and self–assembled structures. Particularly to the final scope of the present work we will now restrict the discussion on molecular J–aggregates.
The so called J–aggregates of cyanine (polymethine) dyes refers to any aggregation of molecules in which the width of the optical absorption band strongly decreases and red–shift with a rise in the compound concentration [55–57]. The reason for this effect has to be ascribed to the fact that under molecular aggregation, the electron transition of individual molecules tightly couples through their Frenkel excitonic interaction with formation of abnormally sharp and intense band (J–band) [58], i.e. the transition dipole of the entire aggregate is larger than that of the molecule considered singularly

(monomer). Since their first discovery in the 1936 by Jelley (Jelly/J–aggregate) [59, 60] and indipendently Scheibe [61, 62], this class of organic compounds has been a focus of extensive studies during the last fifty years and lately also implemented in various commercial applications. The reason is moslty due to the unique spectral characteristics, combined with relative simple fabrication methods (spin–casting, Langmuir–Blodgett and layer–by-layer LBL deposition) [63–65], which could be exploited in a manifold of practical uses for light energy transformation. Abnormally narrow spectral width (completely unusual for organic materials), large oscillator strength [66, 67] and giant cubic susceptibility [68, 69] allows J–aggregates compounds to be implemented as laser active media, optical sensitizers, photoconducting materials, fluorescent tags, highly polarizable systems for nonlinear optics and primers for polymerization reactions [70].

The physical model describing the long–wave shift and enhanced band intensity can be built up by considering the dipole–dipole interaction of a linear chain of two–level point molecules which exhibits a "head–to–tail" orientation [71, 72]. To better comprehend the N molecules interacting system we start the discussion by introducing the concept of a physical dimer [2, 73]. We consider a pair of identical molecules, denoted as 1 and 2, which are close enough to allow interaction between electrons and nuclei but at the same time separated by a distance that neglets orbitals overlap. Under this hypothesis we can describe their electronic excitations as Frenkel/molecular excitons and assume a two level system: S_0 as ground while S_1 as excited state. The Hamiltonian of the dimer H_{dim} would be represented as the sum of the kinetic energies of electron and nucleis of each molecule H_n and all the Coulomb interactions arising from the dipole–dipole coupling V_{12}:

$$H_{dim} = H_1 + H_2 + V_{12}. \tag{2.2}$$

From a diagonalization of the total system we then obtain that the originally degenerate molecular excited states mixes and splits into two new delocalized states with energy separation related to the interaction term V_{12}. Furthermore, the overall transition dipole μ_{tot} will be strongly orientation dependent as represented by a combination of the single components:

$$\boldsymbol{\mu_{tot}} = (\boldsymbol{\mu_1} \pm \boldsymbol{\mu_2}) / \sqrt{2}. \tag{2.3}$$

In case of translational equivalence, i.e. molecules oriented parallel one to the other, the transition moments can be either parallel or antiparallel allowing only one optical transition (figure 2.2 **b**). Whereas in case the molecules are not translationally equivalent both excited states will be nonvanishing, i.e. optically allowed (figure 2.2 **a**).
A similar discussion could be extended in case of a J–aggregate chain of N monomers. Super–radiant emission of the exciton states can be accomplish in case the local excitations in each monomer comprising the molecular chain are spread throughout the aggregate forming collective excitonic states . This is possible due to Forster energy

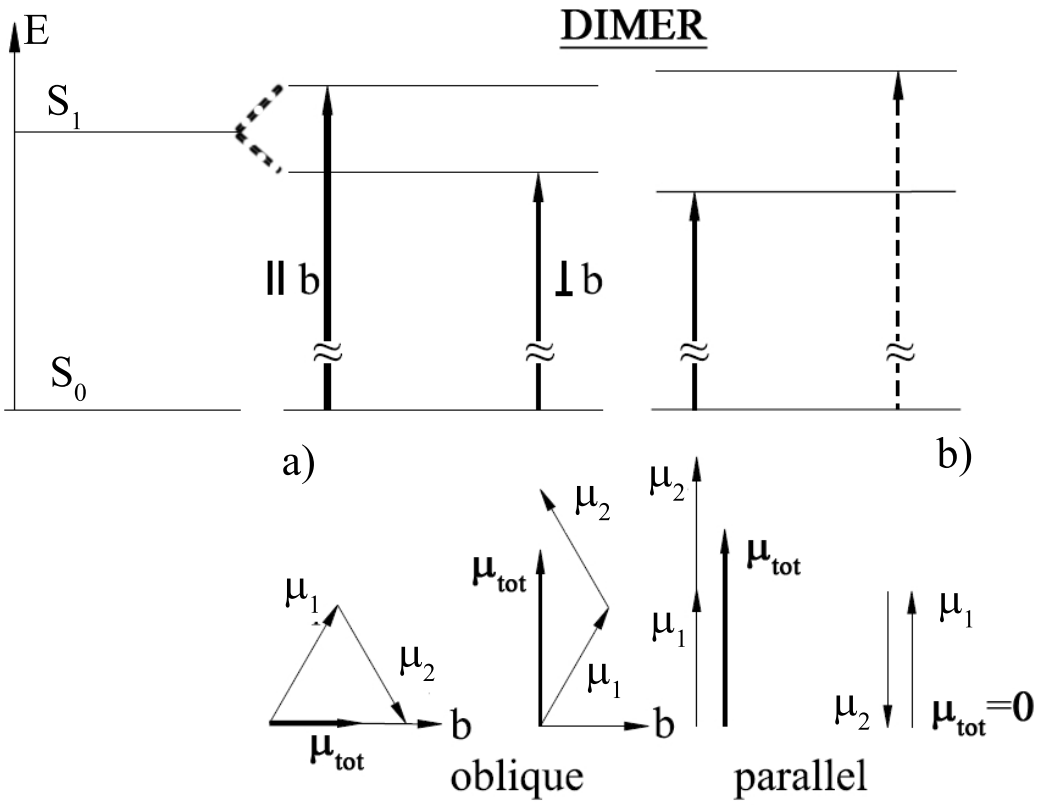

Figure 2.2: Energy level modification which occurs in a dimer system with related schematic representation of total transition dipole μ_{tot} orientation and magnitude in case of oblique (a) and parallel (b) alignement of the single dipole moments μ_1 and μ_2 [2].

transfer between different sites in the aggregate which is usually of dipole–dipole character [66,67]. The 1D coupled exciton model is described by the Frenkel Hamiltonian [57]

$$H_F = \sum_{n}^{N} E_n P_n^{\dagger} P_n + \sum_{n,m \ (n \neq m)}^{N} J_{nm} P_n^{\dagger} P_m \tag{2.4}$$

where the excitation energy of site n is $E_n = \varepsilon_0 + \delta_n$, with ε_0 being the transition energy of an isolated molecule and δ_n the fluctuation of this energy for each molecule within the chain. P_n and $P_n^{\dagger}$ are the Pauli annihilation and creation operators while J_{nm} represents the dipole–dipole intermolecular interaction between the n^{th} and m^{th} molecule on the segment. Here $J > 0$ only in case of nearest–neighbor coupling whereas $J = 0$ for any other interaction. Diagonalization of the Hamiltonian leads to the eigenfrequencies of the one–exciton band at the k^{th} state represented as $\Omega_k = \omega + 2Jcos\,(\pi k/N + 1)$, while the oscillator strength of each dipole transition from the ground state to $k = 1$ state, in the approximation of large N is given by [57]:

$$\mu_{J-agg}^2 \approx 0.81(N+1)\mu_{mon}^2. \tag{2.5}$$

Practical consequence of equation 2.5 is the localization of the oscillator strength towards

the low–lying excitonic states of the J–aggregate [66] which results in the experimental observation of both spectral narrowing and long–wave shift of the absorption peak compared to that of a single monomer (frequency shift of the order of 50-60 nm). Since the net oscillator strength intensity and redistribution on the chain depends on the number of coherently coupled dye molecules, the level of disorder in such compounds is of crucial importance for a correct understanding of the process of light absorption and coupling. A detailed discussion of this problem will be faced in chapter 3.
From a combination of all the characteristics and physical mechanisms discussed above, J–aggregate compounds were succesfully implemented in a microcavity structure by Lidzey *et al.* [42] with achievement of strong photon–exciton coupling at room temperature. This extraordinary and pioneering result has been possible due to the strong oscillator strength of Frenkel excitons in molecular aggregates which remain bound even at 300 Kelvin and permit to obtain gigantic Rabi splitting values (up to 300 meV) much larger than the room temperature thermal noise (≈26 meV), limiting factor for GaAs and CdTe quantum well based microcavities.

2.3.2 Wannier–Mott Excitons in Quantum Wells

Complete different situation occurs in inorganic semiconductors where the high dielectric constant acts as screening effect of the electron–hole Coulomb interaction. From this basis Wannier and Mott [52] developed the concept of the named excitons which can be ascribed with weak Coulomb binding energy (≈1meV) and large charge overlap between neighbouring atoms, i.e. electron and hole hopping on different crystal cells. Mean electron–hole distance is therefore larger than the typical lattice constant (>10nm) and for this reason one can conveniently regard the system as a continuum characterized by a serie of hydrogen–like states where electrons and holes move freely (in conduction and valence band) within the effective mass approximation [74].

More interesting phenomena could be investigated by spatial confinement of Wannier–Mott excitons in thin layers of semiconductors surrounded by different materials characterized by higher band gap. Such confinement quantises the energy states and modifies both exciton wavefunction and density of states (figure 2.3). The binding energy of excitons in quantum wells (2D) increases to four times the value in 3D bulk semiconductors [75] and for this reason absorption and photoluminescence can be observed even at room temperature. Therefore, implementing quantum wells in a microcavity structure allows for resonant coupling of high electric field with the "trapped" excitons and at the final stage permits the achievement of strong light–matter coupling. As a consequence from extremely large Bohr radius which favors overlap and their mutual interaction, Wannier–Mott excitons present small saturation density and strong optical nonlinearities which are then reflected into polariton particles when coupling with photons occurs. Despite weak oscillator strength values compared to that of Frenkel type excitons, these

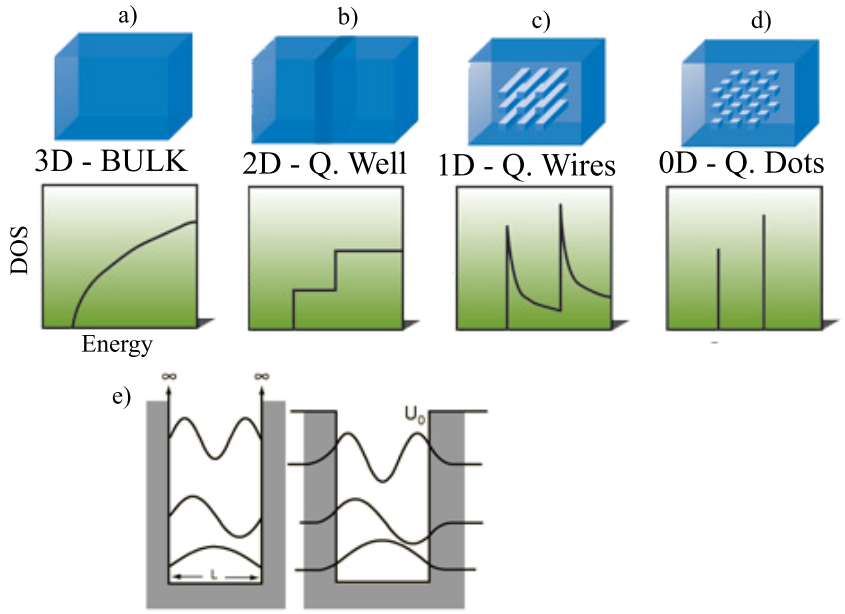

Figure 2.3: Density of states (DOS) calculated for various confinement geometries: (a) a bulk semiconductor/3D system, (b) semiconductor quantum well/2D, (c) 1D system such as quantum wires and for (d) a 0D/quantum dots system. Specifically for a 2D system, quantised wave functions of a particle in a box of width L are displayed in (e) for both cases of infinite and finite barriers (U_0).

properties allow for the observation of nonlinear cooperative phenomena in high Q inorganic microcavities.

A possible route to unify favourable properties of Frenkel and Wannier–Mott excitons in a unique excitonic specie was proposed in 1997 by Agranovich *et al.* [49] and consists in the hybridization of both excitons in mixed organic and inorganic structures. A detailed description of the concept just introduced will be attain in chapter 5 where it will be fully exploited in a hybrid organic–inorganic microcavity.

2.4 The Polariton Picture

After describing the process of light confinement and properties of the electrical excitation in organic and inorganic semiconductor it is now possible to proceed by considering confined excitons in a microcavity structure for the observation of strong light–matter coupling. A strongly coupled microcavity can be realized by design quantum well/J–aggregate exciton position at the antinode of the electric field which propagates through the cavity region, embedded in between two high reflectance DBR mirrors. This is schematically shown in figure 2.4 for both an organic and inorganic based microcavity. Such interaction leads to the formation of new eigenstates called exciton–polaritons,

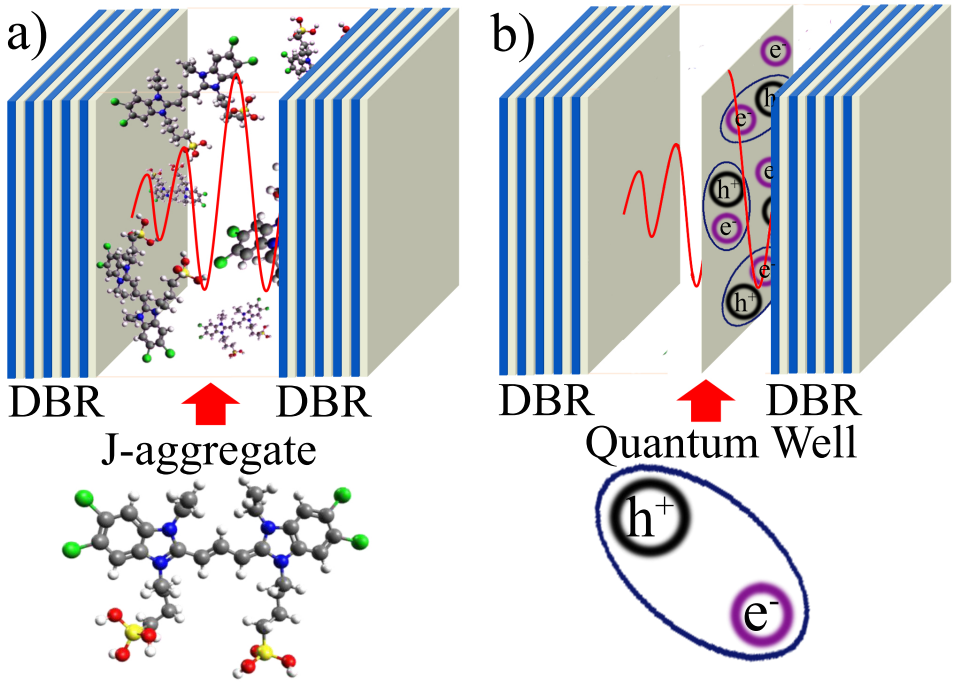

Figure 2.4: Schematic representation of two microcavity structures which embed (a) an organic J–aggregate layer and (b) an inorganic quantum well at the electric field antinode (red line).

described by two energy distributions (Upper and Lower Polariton) which appears in substitution of the exciton and cavity modes (figure 2.5).

The process of strong light matter coupling which results in polariton formation, could be understood as follow. If we consider a medium which possess a strong response to the electromagnetic wave (EM) incident upon it (i.e. photon and matter resonances are equal, $\omega_{cav} = \omega_{ex}$), a large polarization is induced in response to this excitation process. However, when the exciton annihilates the energy is radiated back into the exciting field: a photon with the same energy E and momentum k is emitted. The photon is then reabsorbed by the medium and this periodic energy exchange between ligth and matter continues. Essentially the material absorbs, reemits and then reabsorbs again the same photon until the excitation is lost by scattering processes or the photon escapes out of the cavity. Since an observer cannot define precisely whether the energy in the system exists as a photon or as a polarization in the material, the energy is instead stored in both, creating a quasi–particle consisting simultaneously of light and matter: the exciton–polariton. This mechanism can be physically described by a simplie but precise model which consists in assuming polariton particles as the new eigenstates that arise from the coupling of two oscillators (one exciton and one photon) with independent resonances, ω_{cav} and ω_{ex}, and which oscillate at a modified frequency $\omega_{L,U}$ in case their mutual interaction is strong enough [76]:

$$(\omega_{L,U} - \omega_{ex} + i\gamma_{ex})(\omega_{L,U} - \omega_{cav} + i\gamma_{cav}) = V^2. \tag{2.6}$$

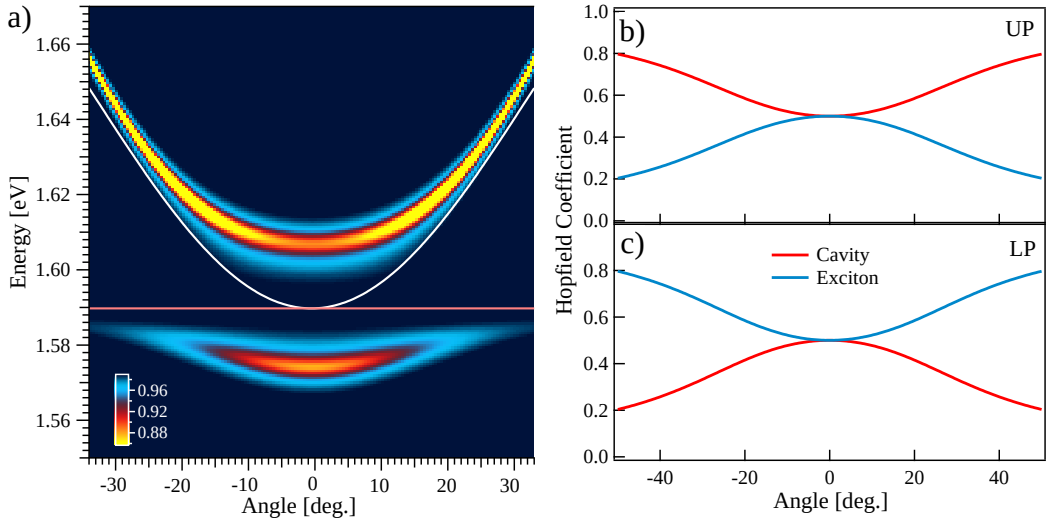

Figure 2.5: a) Dispersion image for a strongly coupled microcavity simulated by mean of a coupled oscillator model. b, c) Hopfield coefficients for upper and lower polariton branch which enlighten cavity and exciton mixing fractions as function of angle. Uncoupled cavity and exciton distributions are also displayed on top of (a) as white and red lines.

As already introduced, ω_{cav} and ω_{ex} define uncoupled cavity and exciton eigenfrequencies while γ_{ex} and γ_{cav}, damping terms, the energy broadening of exciton and empty cavity mode. Besides, V represents the interaction strength.
Resulting from exciton–photon coupling, the solution of equation 2.6 is given by

$$\omega_{L,U} = \frac{\omega_{ex} + \omega_{cav} - i(\gamma_{ex} + \gamma_{cav})}{2} \pm \sqrt{V^2 + \frac{1}{4}(\omega_{ex} - \omega_{cav} - i(\gamma_{ex} - \gamma_{cav}))^2}. \qquad (2.7)$$

At resonance, $\omega_{cav} = \omega_{ex}$, pure real solutions would be obtained only in case the rate of exciton–photon energy transfer is larger than the singular dephasing times: $2V > \gamma_{ex} - \gamma_{cav}$. This condition correspond to the regime of strong coupling where lower and upper polariton branches are formed. Accordingly, in case $2V = \gamma_{ex} - \gamma_{cav}$, the square root becomes immaginary and the transition to weak coupling occurs. In this regime, the solutions are defined by the pure uncoupled exciton and cavity mode. As described by equation 2.7, the new polariton eigenmodes are a coherent superposition of light and matter with a composition that varies with the parallel wave vector $k_{||}$. These mixing terms are the Hopfield coefficients of the new polariton modes and eigenstates of the system in 2.6 [77].
As discussed in section 2.2 cavity mode dispersion is strongly dependent on the in–plane wavevector while exciton distribution can be assumed flat for a wide range of k around 0. Following equation 2.1, the photon energy which is quantized on k_z, can be described

by:

$$\omega_{cav}(k_{||}) = \omega_{cav}(0)\left(1 + \frac{\hbar^2 c^2 k_{||}^2}{\omega_{cav}^2(0) n_{eff}^2}\right) \tag{2.8}$$

where n_{eff} is the effective refractive index of the structure and $\omega_{cav}(0) = c/n_{eff}L_{cav}$ the photon energy at $k_{||} = 0$. However, the in–plane wavevector can also be related to the external angle of incidence of light θ which is shining the structure, by

$$k_{||} = \frac{\omega(k)}{c} sin\theta \tag{2.9}$$

from which directly follows the final expression for the uncoupled cavity mode as function of θ:

$$\omega_{cav}(\theta) = \omega_{cav}(0)\left(1 - \frac{sin^2\theta}{n_{eff}^2}\right)^{-1/2}. \tag{2.10}$$

The significance of the present equation is that under strong coupling regime, formation of two polariton branches occurs, which dispersions vary over the in–plane wave vector following a typical anticrossing behaviour at the exciton–photon resonance, a specific point where polaritons are exactly half light and half matter. The magnitude of this separation will be given by twice the interaction strength $2V$, the Rabi splitting.
Polariton dispersion curves can be directly accessed by mean of angle tuning experiments: reflectance, transmission or photoluminescence can be collected introducing an in–plane component to the photon by moving the detector away from normal incidence.

2.5 Organic and Inorganic Microcavities

Along the present chapter we have demonstrated that polariton particles exist as mixture of light and matter and for this reason it follows that excitonic properties charateristic of a particular material dress the polariton particles and determine their features. Particularly, while the photonic component defines the polariton radiative decay rate, the exciton fraction relates to their ability to scatter and in general interact with the environment [78].

As a matter of fact, the main difference between the two classes of semiconductor resides in the substantial structural disorder typical of J–aggregate compounds which alter dramatically the polariton picture with respect to microcavities structures based on crystalline inorganic materials: Frenkel excitons behave as incoherent excitations while Wannier–Mott like Bloch waves which are described by well defined wavevector and group velocity. Therefore, in a J-aggregate based microcavity the majority of the electronic excited states do not strongly couple to the cavity photons and hence can be regarded as essentially incoherent and localized.
The consequence of structural disorder on the polariton states in organic microcavities has been estensively investigated [3, 79–83]. From a macroscopic approach introduced

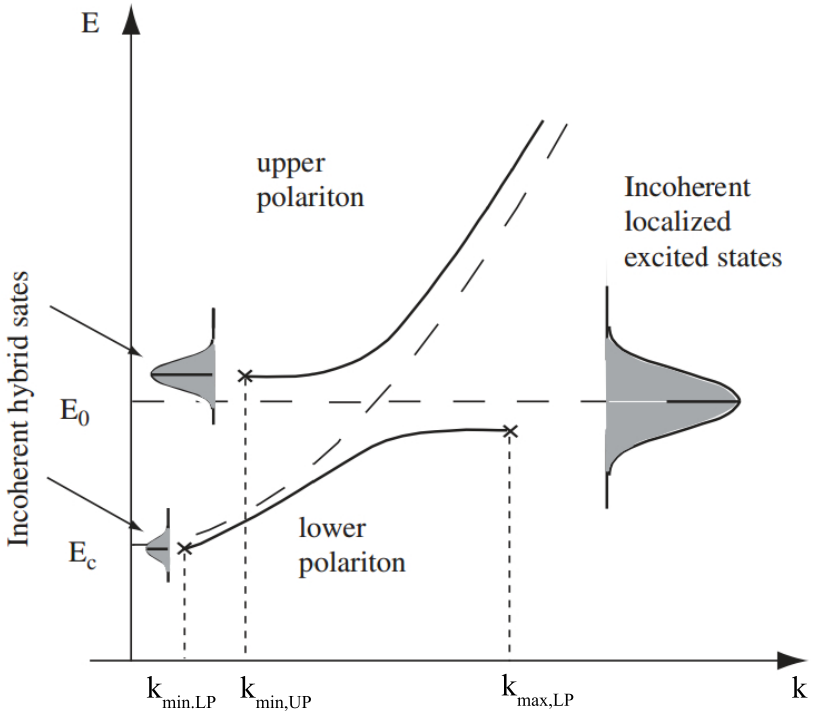

Figure 2.6: Polariton dispersions for a microcavity containing a disordered J–aggregate medium [3].

by Agranovich *et al.* [79] in 2003 which took into account molecular disorder in a phenomenological way through the intrinsic energy broadening of the exciton spectrum, a subsequent work conducted by Michetti and La Rocca few years later expanded the previous description in the frame of a microscopic model [80]. By introducing explicitly the translational symmetry breaking effect, the competition between exciton localization due to the high degree of disorder and the strong light–matter coupling was understood in detail with a representation of coexisting states with different character depending of the spectral and momentum region analysed.

In the strong coupling regime, if the exciton–photon interaction induces the formation of delocalized polariton states with a well defined wavevector, on the other hand, structural disorder responsible of exciton scattering and phase breaking forces the localization of those states, which hence lose the plane–wave shape of polaritons. The resulting incoherent states are found to reside both at large wavevectors and near the bottom of the upper and lower branch, where the momentum uncertainty becomes significant ($\delta k = k$) [79, 80]. The new polariton picture is displayed in figure 2.6 as extracted from reference [3]. In the former case, close to the exciton energy ($k > k_{max}$), remarkable density of uncoupled states may remain present, as also evident from the observation of dispersionless luminescence between the upper UP and lower LP polariton (chapter 3.3). These states are incoherent, similar to the excited states in the noncavity material, and are not affected by the strong coupling. On the other hand, the former case ($k \to 0$) relates to those states that are still cavity polaritons in the sense that they

carry significant photon–exciton mixture although the wavevector is no more a "good" quantum number, i.e. not well defined ($k < k_{min}$). Despite of this, the physics of strong light–matter coupling as previously described is not altered.

Processes of formation and relaxation of exciton–polaritons in strongly coupled inorganic microcavities have been largely investigated and understood as due to mutual exciton–exciton scattering and interaction with low energy (acoustic) phonons [78,84]. Through these mechanisms, injection of carriers by optical or electrical pumping is followed by relaxation of polaritons through the system down to the bottom of the lower branch ($k_{||} = 0$) where, due to their bosonic nature, they can condensate with macroscopic occupation densities [29, 85, 86]. It is worth noting that this process is generally slow (>1ns) and inefficient due to the formation of a bottleneck region at the point where the photonic character of lower branch polaritons becomes predominat over the excitonic fraction [87–89].

On the other hand, presence of substantial degree of structural disorder and high energy molecular vibrations modify and alter the polariton relaxation dynamics in organic based microcavities. These strong vibrational modes, as detailed explained in chapter 3.3 and references [49, 90, 91], allow for strong and effective exciton–phonon coupling especially with the large density of incoherent states providing an additional means for polariton state population. As such, the following scenario can be pictured as consequence of these considerations. Under nonresonant optical excitation, the majority of the incident radiation which couples through the mirrors contributes to the formation of high energy incoherent states. Then, fast relaxation mediated by interaction with acoustic phonons occurs with increase of population at the low energy tail of the Gaussian distribution which refers to uncoupled excitons; the so called exciton reservoir (ER) is hence formed. Subsequently, radiative decay from these incoherent states directly pumps the coherent upper and lower branch polariton states in resonance with the exciton energy. In case of weak coupling regime, this photoluminescence emission simply radiates out of the mirror following the cavity dispersion. With extremely short lifetime, the upper polaritons nonradiatively decay back into the large number of incoherent states (ER). Such process was demonstrated to be very fast and effective [45,79] explaining the weaker population density found in the upper branch with respect to the lower [92]. In contrast, polariton population of the lower branch states which are not optically pumped by the exciton reservoir occurs via relaxation mechanisms, such as exciton–exciton scattering and exciton–phonon scattering.

However, thermalization of polariton particles at low wavevectors is generally much harder to achieve compared to inorganic based MCs. This is due expecially to the large amount of uncoupled excitons which reduces the overall polariton population and despite the presence of high energy molecular vibrations which act as efficient channel to reduce bottleneck effects and speed up the relaxation process (≈100ps) [1, 45].

3 Organic Microcavities

3.1 Introduction

Since the first observation of strong coupling in an organic based microcavity [42], many different attempts have been done and different organic compounds were implemented as active medium: porphyrin dyes, J-aggregate cyanine dyes and small molecules [93–95]. Despite many interesting results have been achived, the most used and exploited material is at the moment represented by J-aggregate cyanine dyes: long aggregation of monomers (up to 1000) which possess intense and sharp absorption band (J-band), high radiative rates and very small Stoke shift [58]. Dipole–dipole interaction of individual monomers of the chain leads to energy transfer throughout the chain and delocalization of the eigenstates. In contrast, intrinsic disorder due to fluctuations in the onsite energy of the monomers tends to localize the eigenstates at specific segments of the chain. The resulting interplay between these two competing trends together with the coupling to the cavity field results in extended polaritonic states where several monomers contribute through their excitonic components. Although, on the total amount of excitonic states only few of them are coherently coupled and possess required oscillator strength to participate in the polariton formation (*bright states*). The majority (>70%) are optically inactive, in this sense *dark*, and form the ensemble of uncoupled states, i.e. the exciton reservoir (ER) [79]. The overall polariton density of states is thus enormously small with respect to the initial excitonic population.

Recalling from chapter 2.5, the process of polariton formation in organic microcavities optically or electrically excited, can be described as follows. Excitons created at high energy states by the pump immediately relax (within few fs) into the low energy tail of the ER Gaussian distribution through scattering with acoustic phonons [81]. The optical cavity mode creates a coherent polarization in the active region which interacts with the collective molecular states. If this interaction is strong enough light–matter coupling occurs with typical Rabi splitting and formation of delocalized polariton eigenstates. The rest of the excitonic states in the ER remain incoherent and localized on the molecular

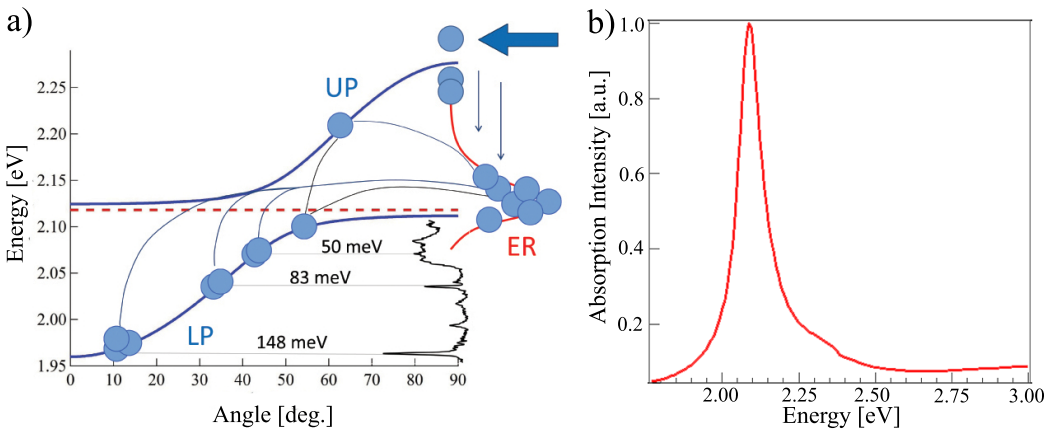

Figure 3.1: a) Simplified scheme of polariton formation and relaxation in organic based microcavities. Excitons formed at high energy by nonresonant pumping immediately relax into the uncoupled exciton reservoir (ER). Relaxation into upper (UP) and lower (LP) branches occur via phonon assisted scattering (Raman spectra shown). b) Absorption spectra of the TDBC J–aggregate cyanine dye.

sites because uncoupled to light (figure 3.1 **a**). Besides, as explained in detail in the following sections 3.3, high energy molecular phonons provide an additional means for population of polariton states through their interaction with excitons and subsequent vibrationally assisted scattering into the lower branch dispersion .In general, the scattering dynamics from ER and between UP and LP branches, together with exciton and polariton lifetimes depend on cavity quality factor, dye concentration and nature of the dye molecule used as active medium.

The large amount of uncoupled excitons that sit inactive in the reservoir represent the strongest limitation for observation of any kind of nonlinear process (parametric amplification, lasing and Bose–Einstein condensation). This is why the polariton density of states which can be normally achieved remains always below the population threshold required for occurrence of such phenomena. To deeply understand and solve the problem one has to look at the molecular length over which the exciton wavefunction is coherent. For each type of J–aggregate molecule the coherence length is determined by the interplay between the intermolecular excitation transfer interaction, the static and dynamic (scattering by nuclear motions) disorder and the inelastic scattering [58, 96]. The correlation of this specific value to the process of interaction and coupling of collective excitonic states with the cavity photons would provide a realistic picture of the available exciton "bright" states population and, at a later stage, of the polariton density.

Following this idea, the chapter starts with a study of the intrinsic third order optical nonlinearities of a specific J–aggregate cyanine dye. The calculation of molecular coherence length will be directly inferred from the experimental measurements and connected to the corresponding degree of disorder which has to be taken into account for the modeling of a strongly coupled microcavity system. J–aggregate based microcavities will be then explored via angle–resolved photoluminescence and pump–probe spectroscopy.

Experimental results will be shown and related discussion presented with particular attention on polariton formation and phonon–mediated scattering. All the results and discussion presented below come from an intense and productive collaboration with Dr. Leonidas Mouchliadis and Prof. Ilias Perakis which provided the theoretical support used here to interpret the experimental data and model J–aggregate and microcavity behaviors.

3.2 J-aggregate Nonlinearities

A thin film of J–aggreagate cyanine dye 5,6-dichloro-2-[[5,6-dichloro-1-ethyl-3- (4-sulfobutyl)-benzimidazol-2-ylidene] propenyl]-1-ethyl-3-(4-sulfobutyl) - benzimidazolium hydroxide, sodium salt (TDBC) is firstly characterized and subsequently used as active compound for the realization of microcavity structures. Absorption spectra of the TDBC film is defined by 51 meV linewidth and maxima located at 2.10 eV (figure 3.1 **b**). Here we make use of the single beam Z–scan technique (extensively described in Appendix A 7.1) which permits to precisely measure sign and magnitude of third order optical nonlinearities ($\chi^{(3)}$) of the material investigated. By moving the sample along the focus of a pumping Gaussian beam, the transmittance variation is recorded at each step. From this curve, nonlinear refractive index and nonlinear absorption (when present) can be directly extracted. Additionally, exciton coherence length can be inferred by power dependence study of the absorption variation.
The thin film characterized in our study was obtained by spin casting onto a quartz substrate few μl solution of the J–aggregate dye (concentration of 4.2 mg/ml) suspended in a water based polyvinylalcohol matrix (33 mg/ml). Refractive index ($n_0 = 4$) and thin film thickness (400nm $\pm$ 2nm) were measured by high precision scanning ellipsometer within a range of 0.77 eV up to 6.2 eV.

3.2.1 Theory

In the polariton picture, a consistent description of nonlinear phenomena is based on the interaction of intense electromagnetic radiation with high electronic excitation densities produced in the medium. The study of characteristic third order optical nonlinearities (nonlinear absorption and refraction) of the active material will also enlighten on the process of population redistribution over two or more excited states.
We first start by describing our system (TDBC J–aggregate film) as an ensemble of discrete monomers each one defined by three energetic levels: ground state S_0, first S_1 and second excited state S_2 (figure 3.2 **a**). In the process of light absorption, electronic species in the ground state can be promoted to a first excited level that serves as the lower state of a second electric dipole allowed transition before excitons decay back to the ground level. This mechanism is called *Excited State Absorption* (ESA) and can

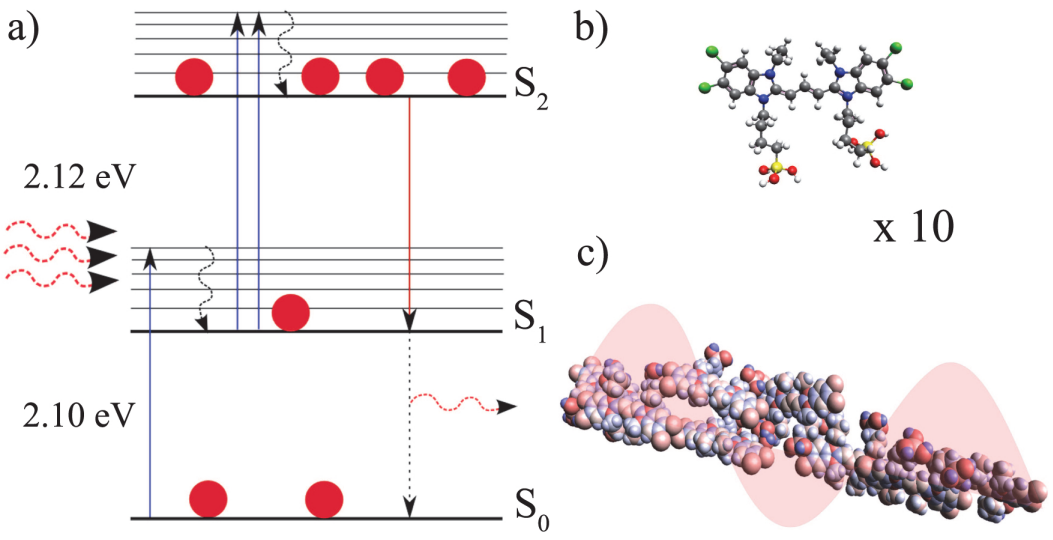

Figure 3.2: a) Energy level diagram for the TDBC J–aggregate molecule (b), displayed together with a schematic rapresentation of the exciton wavefunction spread over a calculated average of 10 monomers (c).

be conveniently described by absorption cross sections of ground (σ_{01}) and first excited state (σ_{12}) which are related to the dipole matrix elements $|\mu_{01}|^2$ and $|\mu_{12}|^2$. In this case, the ESA coefficient is:

$$\alpha_{12} = \sigma_{12} N_1 \tag{3.1}$$

with N_1 the exciton concentration on S_1:

$$\frac{dN_1}{dt} = \frac{\alpha_{01}}{h\nu} I. \tag{3.2}$$

Here $h\nu$ is the photon energy which produces the excitation, I the irradiance and α_{01} is the linear absorption coefficient of the ground state, described also via cross section σ_{01} times the density of the absorbing elements N_0 on the state. To study the effect of ESA on the transmitted intensity we first integrate such equation and introduce the total fluence $F(t)$,

$$N_1 = \frac{\alpha_{01}}{h\nu} \int_{-\infty}^{0} I(t')dt' = \frac{\alpha_{01}}{h\nu} F(t). \tag{3.3}$$

By plug the above, in the following equation of irradiance variation

$$\frac{dI}{dz} = -\sigma_{01} N_0 I - \sigma_{12} N_1 I \tag{3.4}$$

we then obtain

$$\frac{dF}{dz} = -\sigma_{01} N_0 F(t) - \frac{\sigma_{01}\sigma_{12}}{2h\nu} N_0 F^2(t). \tag{3.5}$$

In the particular case where excited state absorption cross section is larger than the ground state one ($\sigma_{12} > \sigma_{01}$) the process of light absorption is modified in the sense that increasing input yelds increasing loss: the first excited state (S_1) absorption becomes predominant with respect to the ground state absorption and thus an increase of population

at higher excited levels (S_2) occurs at the expenses of S_1. These high energy states are in most cases dark because of ultrafast non radiative decay mechanism. As such the overall photoluminescence is subjected to an important decrease at high power densities. This effect is described in literature as *Reverse Saturation of Absorption* (RSA) [97–100] and relates directly to the intrinsic optical properties of the J–aggregate dye under study. In this sense exciton–exciton annihilation, important mechanism which has been adopted as first cause for absorption and PL quenching observed for the TDBC J–aggregate dye [101], must be reconsidered in the light of this optical limiting behaviour. As such, being RSA the predominant effect, exciton–exciton annihilation would represents only a second order process in the optical response of reverse saturable absorbers excited by intense optical stimulus.

In presence of RSA the far–field intensity deviation from a Gaussian distribution is caused not only by nonlinear refraction, as the Z–scan theory explains, but also by nonlinear absorption. Considering the third order optical nonlinearity $\chi^{(3)}$ as:

$$\chi^{(3)} = \chi_R^{(3)} + i\chi_I^{(3)}, \tag{3.6}$$

the nonlinear refractive index n_2 and the nonlinear absorption coefficient α_2 are related to the real and imaginary part of $\chi^{(3)}$ by the Kramers–Kroning relations [102, 103]:

$$\chi_{Re}^{(3)} = 2n_0^2\epsilon_0 c n_2, \tag{3.7}$$

$$\chi_{Im}^{(3)} = \frac{n_0^2\epsilon_0 c\lambda}{2\pi}\alpha_2. \tag{3.8}$$

We now follow the theoretical description of the Z-scan technique reported in the literature [104, 105] which solves the equation of fluence 3.5 over the spatial extent of a Gaussian beam pulse, to obtain the normalized transmittance for an open aperture Z–scan measurements:

$$T = \frac{ln(1+\frac{q_0}{1+x^2})}{\frac{q_0}{1+x^2}} \tag{3.9}$$

where [104–106]

$$q_0 = \frac{\alpha_{01}\sigma_{12}F_0 L_{eff}}{2h\nu} = \alpha_2 I_0 L_{eff} \tag{3.10}$$

and $x = z/z_0$. F_0 (I_0) is the fluence (irradiance) of the laser at the focus, l is the sample thickness and

$$L_{eff} = (1 + e^{\alpha_{01}l})/\alpha_{01}. \tag{3.11}$$

Equation 3.10 was used to extract, directly from the experimental curves, the values of excited state absorption cross section (σ_{12}) and of the nonlinear absorption coefficient α_2. Combined with the nonlinear refractive index extracted from a close aperture Z–scan, in the way described in Appendix A (7.1), we could calculate the third order optical nonlinearities $\chi^{(3)}$ in virtue of 3.7 and 3.8.

Despite the fact that Z–scan measurements provide precise values of excited state absorption cross section and nonlinear coefficients α_2 and n_2 simply from the analysis of the experimental curves, an extended analysis which also considers reverse saturation of absorption and exciton relaxation over the molecular energy levels is pursued. This model, based on the three level system described at first at the beginning of the section, is used in fact to calculate the temporal evolution of population redistribution among the energetic states. More specifically, considering that the origin of optical nonlinearities $\chi^{(3)}$ is related to the intensity–dependent population density of the excited levels, excitation and decay mechanisms which govern electronic distribution (N_0, N_1 and N_2) on the three energetic states (S_0, S_1 and S_2) can be described by a set of three coupled differential equations [107, 108]:

$$\begin{cases} \frac{\partial N_0}{\partial t} = -\frac{\sigma_{01} I}{\hbar\omega} N_0 + \gamma_{10} N_1 \\ \frac{\partial N_1}{\partial t} = \frac{\sigma_{01} I}{\hbar\omega} N_0 - \frac{\sigma_{12} I}{\hbar\omega} N_1 - \gamma_{10} N_1 + \gamma_{21} N_2 \\ \frac{\partial N_2}{\partial t} = \frac{\sigma_{12} I}{\hbar\omega} N_1 - \gamma_{21} N_2 \end{cases} \tag{3.12}$$

where γ_{10} and γ_{12} represent decay rates from S_1 to S_0 and from S_2 to S_1 respectively. Relaxation from S_2 to S_0 is neglected and as commonly treated [99,108], γ_{12} is assumed to be larger than γ_{10}. Accordingly to the description of a reverse saturable absorber, large excited state absorption cross section with respect to the ground state one ($\sigma_{12} > \sigma_{10}$) has also to be considered as indicated by the experimental results. Moreover, steady state solutions of the time dependent absorption variation, described as:

$$a(t) = [N_0 \sigma_{01} + N_1 \sigma_{12}], \tag{3.13}$$

are used to reproduce the observed reverse saturation of absorption behaviour with high accuracy. We now relate nonlinear absorption and nonlinear refractive index to the population density for each state and express the two coefficients via the following [107, 108]:

$$\begin{cases} \alpha_2 = \frac{1 + K_a \frac{I}{I_s}}{1 + \frac{I}{I_s}} \sigma_{01} N_0 \\ n_2 = \frac{1 + K_r \frac{I}{I_s}}{1 + \frac{I}{I_s}} \eta_{01} N_0. \end{cases} \tag{3.14}$$

Here $I_s = h\nu\gamma_{10}/\sigma_{01}$ is the saturation intensity and the quantities K_a and K_r, respectively the ratio of absorption cross section and refractive volume of the excited state to that of the ground state: $K_a = \sigma_{12}/\sigma_{01}$ and $K_r = \eta_{12}/\eta_{01}$. To fully understand the importance of the equations in 3.14 we must consider that nonlinear refraction of a specific material is similar to the nonlinear absorption in the sense that it also results from the excitonic transitions between molecular energy levels. Under this consideration nonlinear refractive index can be related to the population difference between the levels and represented via the constant of proportionality η, the refractive volume [109]. From equations 3.14 we can then distinguish between reverse saturable absorption ($K_a > 1$) or saturable absorption ($K_a < 1$) and at the same time relate the sign of the nonlinear

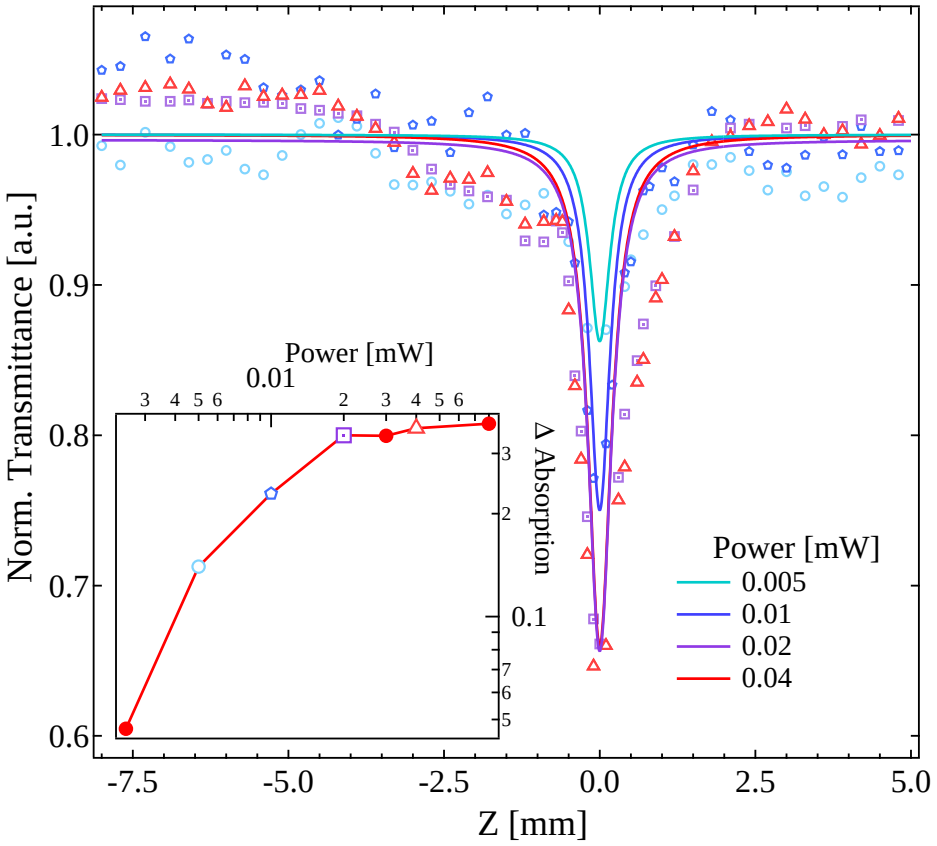

Figure 3.3: Experimental (symbols) and modeled (solid lines) Z–scan transmission signals at different power intensities for a TDBC film. Absorption saturation as function of pump power is shown as inset.

refractive index to the molecular energy level occupancy by K_r. If excited state refrangibility is greater than that of the ground state, $K_r > 1$, than the total refractivity increases ($n_2 > 0$) while decreases ($n_2 < 0$) if smaller, i.e. $K_r < 1$ [109].

Results of the theoretical analysis are summarized and discussed in the following section.

3.2.2 Results and Discussions

The first important consideration refers to the shape of the characteristic open aperture transmittance curves displayed in 3.3 and obtained by optically pumping the TDBC film with a pulse beam at 2.138 eV and 80 MHz repetition rate. In here, the sign of the absorption peak at the focal point of the focussed beam ($Z = 0$), indicates maximum film absorption in the presence of maximum incident light, i.e. reverse saturation of absorption (RSA). As expected, value of ground state absorption cross section has been found to be much smaller than the excited state one: $\sigma_{01} = 1.01x \times 10^{-14} cm^2$ versus $\sigma_{12} = 5.68 \times 10^{-13} cm^2$ with resulting ratio of $K_a = 56$, in accordance with the RSA case. Ground state cross section was calculated from the linear absorption coefficient, $\alpha_{01} = \sigma_{01} N_A C = 2.8 \times 10^4 cm^{-1}$ (N_A is the Avogadro number and C is the concentration in

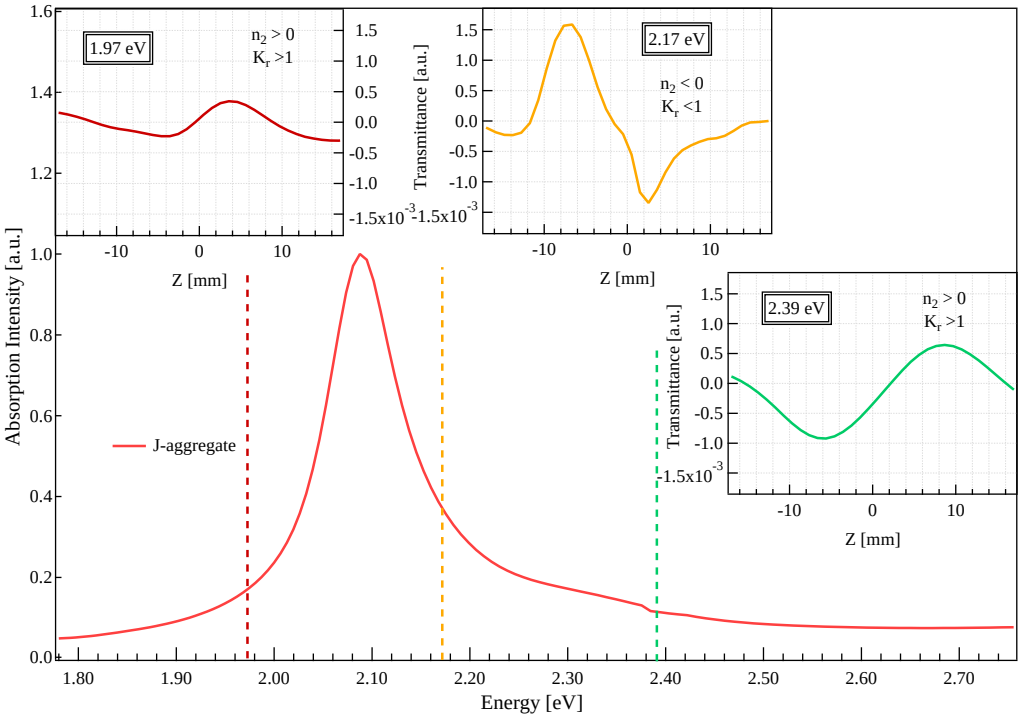

Figure 3.4: Absorption spectra for a TDBC J–aggregate film (red line). Close aperture Z–scan curves which present nonlinear refractive index changes of sign, are shown as insets for three different pump energies.

mol/cm^{-3}) while that of the excited state was extracted from the Z–scan transmittance curve following the process described in the previous section (equation 3.10). Nonlinear absorption coefficient is calculated in the same way and its value has found to be $\alpha_2 = 2.9 \times 10^2 cm/W$ ($\chi^{(3)}_{Im} = 1.14 \times 10^{-4} cm^2/V^2$).

Informations about the degree of disorder and exciton wavefunction delocalization characteristic of the TDBC cyanine dye are deduced experimentally by performing near resonance (2.138 eV) Z–scan at different power intensities. When saturation of absorption is reached, 0.02 mW (0.08 nJ) in our case (figure 3.3), the number of photons absorbed by the system becomes equal to the number of collective excitations. Therefore a comparison between the molecular and photon density at the saturation point leads to the number of molecules simultaneously excited by a single photon, i.e. the number of molecules coherently coupled together. From our calculation, based on molecular weight, dye concentration and power intensity at saturation, we obtain a coherence length value of 10 molecules. This value well agrees with previously reported results [110, 111] also related to a J–aggregate dye characterized by a very similar molecular structure, hence showing that the optical properties of the film are determined only by the microstructure of the J–aggregate dye and not by the film morphology. The truthfulness of our interpretations is stressed even more by the high fidelity of experimental (symbols) and simulated (solid lines) transmittance curves displayed together in figure 3.3.

Additional indication on third order nonlinearities could be extrapolated by the analysis of the close aperture Z–scan characteristic which provides direct indications on the nonlinear refrangibility of the compound. The shape of the transmittance curve is in fact related to the sign of n_2 which physically identifies a self–focusing or self–defocusing behaviour [100, 104]. When various excitation pump energies are used, distinctive changes of sign in corrispondance of well define positions on the TDBC absorption spectra are observed: positive at 1.97 eV, negative at 2.17 eV and again positive at 2.39 eV (figure 3.4). Accordingly to the description of nonlinear refractive index illustrated in the previous section, the alternance of sel–focusing and self–defocusing behaviour also defines a population density oscillation between ground and first excited state. At 2.39 eV, the close aperture transmittance is defined by a valley–peak shape which indicates a positive nonlinear refractive index, $n_2 = 3.86 \times 10^{-6} cm^2/W$ ($\chi^{(3)}_{Re} = 3.28 \times 10^{-7} cm^2/V^2$, self focusing behaviour) and a value of $K_r > 1$. The density of population of the first excited state, which is related to the refractive volume ratio K_r, is bigger in respect to the ground one. A similar behaviour occurs at 1.97 eV where a value of $n_2 = 1.10 \times 10^{-6} cm^2/W$ is calculated ($\chi^{(3)}_{Re} = 8.57 \times 10^{-8} cm^2/V^2$).

A different situation occurs for an excitation energy of 2.17 eV, very close to the first resonance (2.10 eV) and characterized by almost double absorption intensity. A negative nonlinear refractive index is measured, $n_2 = -5.84 \times 10^{-6} cm^2/W$ ($\chi^{(3)}_{Re} = -4.96 \times 10^{-7} cm^2/V^2$), and correspective refractive volume ratio, $K_r < 1$, indicates higher occupation of the ground state in respect to that in S_1. This behaviour does not directly depend on the wavelength of the excitation beam but mostly on the total absorption of the dye and hence on the RSA strength, which varies dramatically at the energy positions we have investigated. As result, the population distribution among the three energy levels is strongly affected whitin the same range of radiation intensities which remains always below the saturation point. The demonstration of this behavior is provided by the changes in the density of states N_0, N_1, N_2 shown in figure 3.5 and extracted from the system in 3.12 where a continuous excitation source is implied.

By definition of reverse saturable absorption, each photon introduced in the system is more likely to be absorbed by particles already excited in the first energy level rather than excite another one from the ground state. The extra energy introduced in the system is devoted to depopulate S_1 by moving the excitons that reside in it to the second excited level S_2 which at steady state is the one that carry most of the excitation. At equilibrium the system falls in a regime where the exciton density ratio between first excited and ground state depends on the combination of characteristic absorption cross sections σ_{01}, σ_{12}, decay rates γ_{21}, γ_{10} and excitation beam energy $\hbar\omega$, as described by the rate equations in 3.12. Therefore the evolution in time of the population occupation of each level, displayed in figure 3.5, confirms this assumption and provides an additional means for the interpretation of the observed oscillations of excited/ground state population ratio related to the sign of n_2.

When the pump beam energy is 1.97 eV, we experimentally observe that the equilibrium

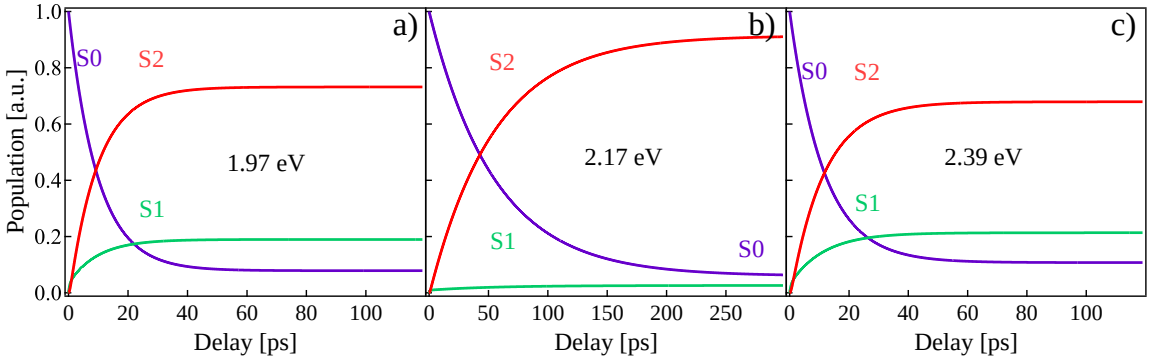

Figure 3.5: Time evolution of the population densities N_0, N_1 and N_2 in each of the three states S_0, S_1 and S_2 as extracted from the rate equation system introduced in 3.12 for three different pumping energies: (a) 1.97 eV, (b) 2.17 eV and (c) 2.39 eV.

between excitation/relaxation processes results in the presence of higher exciton density in the first excited state compared to the ground one. Theoretical simulations presented in figure 3.5 **a** describe the identical scenario: at steady state, reached after 100 ps from the arrival of the pump ($t = 0$), S_2 carries most of the population while S_1 appears weakly (20%) but at the same time more populated with respect to S_0 ($\approx 10\%$). As expected, reverse saturation of absorption governs the general energy levels dynamics by driving the biggest exciton amount (70%) on the nonradiative S_2 level just after few ps from the arrival of the pump. With an excitation energy of 2.39 eV (graph **c**), exciton redistribution throughout the levels follows a similar behavior to the one just described with the only slight reduction of N_2 in favour of both N_0 and N_1.
On the other side, close to TDBC resonance (2.17 eV) where dye absorption remarkably increases, nonlinear refractive index is found to be negative and as consequence refrangibility ratio $K_r < 1$. Calculation of N_0, N_1 and N_2 displayed in 3.5 **b** confirms once more the experimental results. The S_2 level remains the most populated state as expected from RSA while excitation density in S_1 strongly reduces to reach a percentage that at steady states results weaker than the one found in S_0, approximately constant. Furthermore we observe that steady state equilibrium is reached only after $\approx$250 ps from the arrival of the pump indicating a much slower response of the dye in respect to the previous cases (figure 3.5 **a,c**) where this delay was found to be less than the half ($\approx 100ps$). This behaviour directly results from the stronger RSA effect observed near the peak resonance where higher S_1 absorption retards the achievement of the steady state S_2 population density expected. The calculation of N_0, N_1 and N_2 as function of time t presented in figure 3.5 is extracted from the system in 3.12 for a fixed value of pumping beam intensity I set below the saturation point.

The conclusions we can deduce from this analysis is that despite the TDBC J–aggregate possesses relatively high optical nonlinearities and oscillator strength, reduced molecular

coherence length and especially reverse saturation of absorption seem to limit its qualitative behaviour in the presence of intense illumination. Therefore, its role in a more complex system, as a planar microcavity could be, needs a revised theoretical investigation which put its basis into a realistic parameter of the intrisic degree of disorder. Only in this way it would be possible to fully exploit the potentialities of J–aggregate based microcavities towards the observation of collective nonlinear phenomena.

3.3 Polariton Formation and Decay Mechanism

After the study of the intrisic structural and optical properties of the TDBC J–aggregate dye we follow the discussion with an investigation of the exciton–polariton dynamics in organic based microcavities.
The microcavity samples under analysis were provided by the group of Prof. David Lidzey at the University of Sheffield and consist of 220 nm J–aggregate TDBC thin film, stacked in between two dielectric Distributed Bragg Reflectors (DBR) mirrors composed of 11 $\lambda/4$ pairs of SiO_2 and Ta_2O_5. Oxygen plasma sputtering deposition (Helia Photonics company) has made possible the realization of high finesse optical cavity mirrors with quality factor of ≈ 300 and respective polariton radiative lifetime of 100 fs. On the other hand, the organic active layer was prepared by dispersing the TDBC cyanine dye in a polyvinylalcohol (PVA) water based matrix (33 mg/ml). The solution was subsequently spin casted onto the bottom DBR mirror previously treated with oxygen plasma bath to remove any organic contaminant. The TDBC dye concentration was varied in between different samples to modify effective oscillator strength and hence tune the Rabi splitting energy as the exciton–photon interaction takes place.

3.3.1 Ultrafast Phonon Assisted Polariton Build Up

The optical characterization of the planar microcavities was at first performed by means of room temperature angle–resolved photoluminescence spectroscopy (Appendix A 7.2). For the purpose a nonresonant quasi–CW pump excitation at 2.33 eV (7.58 kHz repetion rate and 0.51 nm pulse width) was implemented. By tilting the sample with respect to the excitation/collection lens we were able to image on a charge coupled device (CCD) detector the angular photoluminescence emission in a range of angles from 0^o up to 60^o. With such configuration it was possible to characterize the lower polariton branch entirely till the anti–crossing point which in the case of strong Rabi splitting occurs at high wavevectors. At the same time linearly polarized detection, perpendicular to the molecular transition dipole moment, was used to meet the resonant condition for the polarization–dependent Raman scattering process. This effect, which has been shown to play a crucial role in the polariton decay process, is due to the strong birefringence of the spin casted film which results from the allignement of the molecular aggregates

in the matrix [58, 91, 112]. In strongly coupled organic microcavities in fact, discrete high energy vibrational modes characteristic of the organic active medium, interact with electronic excitations and provide an efficient relaxation channel into lower energy polariton states where the spectral separation from the lowest tail of the exciton reservoir matches the molecular vibrations energies. As a result, high population densities and intensity maxima are observed in the LP photoluminescence emission in correspondance with phonon peaks visible in the Raman spectra when scaled to the ER energy (figure 3.6). Interestingly, the possibility to exploit manifold detuning conditions by a simple scan over the sample surface permits to activate different vibrational modes depending on the availability of polariton "trap" states in the lower branch.
To confirm our findings and fully explain the process, we developed a theoretical model of the system and solve the Heisenberg equation of motion which describes the time-dependent lower polariton branch occupation. The linear model of a molecular aggregate comprising hundreds (N) of monomers is described by the Frenkel Hamiltonian [67, 113] which takes into account that localized excitations are spread throughout the aggregate by means of dipole–dipole intermolecular forces. By introducing the bosonic operator $b^{\dagger}_{\nu i}$ which creates the νth collective excitation in the ith aggregate (over a total of N_{agg}), we hence obtain the J–aggregate ensemble Hamiltonian:

$$H_{agg} = \sum_{\nu,i}^{N,\,N_{agg}} \epsilon_{\nu i} b^{\dagger}_{\nu i} b_{\nu i} \tag{3.15}$$

which describes the collective excitonic states defined at specific segments of the linear chain. Besides, commonly assumed molecular disorder is here introduced by considering energy fluctuation with a Gaussian distribution [114, 115]. At this point we dropped the nonlinear exciton–exciton interaction term to focus the attention on the linear response.

When considering a microcavity system and subsequent photon coupling term we obtain a description of the final exciton–polaritons as delocalized eigenstates of the microcavity that interact with the localized collective excitations of each aggregate (ER) [79] through absorption or emission of vibrational quanta, also localized at each monomer of each aggregate. The resulting Hamiltonian is:

$$\begin{aligned} H_{LP} = \sum_{k} E^{LP}_{k} P^{\dagger}_{k} P_{k} + \sum_{\nu i} \epsilon_{\nu i} b^{\dagger}_{\nu i} b_{\nu i} + \sum_{\lambda i} \omega_{\lambda i} c^{\dagger}_{\lambda i} c_{\lambda i} + \sum_{\nu\nu'\lambda i} g^{\lambda i}_{\nu\nu'} b^{\dagger}_{\nu i} b_{\nu' i} (c^{\dagger}_{\lambda i} + c_{\lambda i}) + \\ \sum_{kk'\lambda i} g^{\lambda i}_{kk'} P^{\dagger}_{k} P_{k'} (c^{\dagger}_{\lambda i} + c_{\lambda i}) + \sum_{k\nu\lambda i} [g^{\lambda i}_{k\nu} P^{\dagger}_{k} b_{\nu i} + g^{\lambda i *}_{k\nu} b^{\dagger}_{\nu i} P_{k}] (c^{\dagger}_{\lambda i} + c_{\lambda i}) \end{aligned} \tag{3.16}$$

where the first three terms introduce respectively lower polariton branch, uncoupled reservoir excitons and phonons bath. The subsequent terms describe the separate coupling of phonons with ER states and lower branch polaritons while the last defines the exciton–polariton interaction mediated by the phonons bath. While exciton–photon

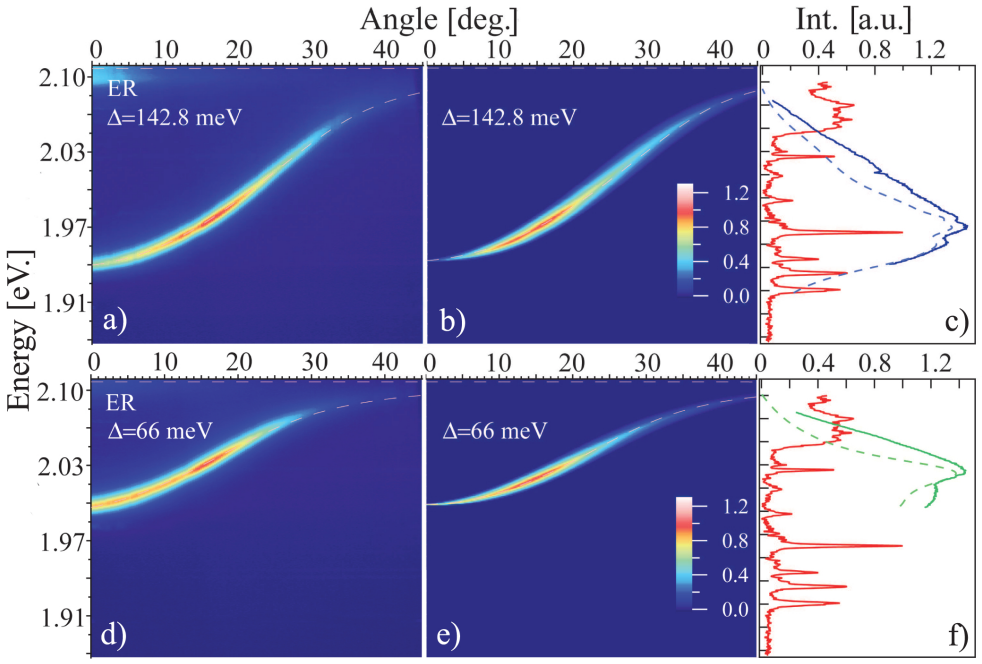

Figure 3.6: a, d) Normalized contour plots of the measured PL intensity for two different exciton-photon detuning values. b, e) Modeled photoluminescence intensity calculated in steady state condition. c, f) Raman spectra (red line) and integrated PL profiles extracted from respective measured (solid line) and simulated (dashed line) PL contour plots.

coupling was obtained by considering only the lowest exciton eigenstate in the Lifshitz tail of the J-band of each aggregate, the phonon energies used in our simulations were extracted from the measured J–aggregate Raman spectra (red line in figure 3.6 **c** and **f**) and scaled to the ER energy (peak of the Boltzman distribution). The Heisenberg equation of motion of the lower polariton population was then coupled to the phonon–assisted density matrices which were treated in steady state by introducing their dephasing time which guarantees energy conservation condition [116]. The contour plots and profiles of figure 3.6 which present a comparison between experimental and simulated PL emission at two different detunings show the excellent accordance of our model.

The following step of the analysis consisted in the time–dependence study of the lower polariton population. To compare temporal photoluminescence dynamics of the real system with the one extracted from the theoretical model through the steady solutions of the Heisenberg equation of motion, we perfomed transient pump–probe spectroscopy on the lower polariton branch by exploiting the setup fully described in Appendix A (7.4). The microcavity structure was excited non–resonantly using a pump pulse of sub-100 fs width and 250 kHz repetition rate, at energy of 3.1 eV. The entire lower polariton dispersion was resonantly scanned by adjusting the energy of the probe beam accordingly (1.91 eV and 1.968 eV) while, for each LP position, the transmitted signal was recorded with a balance detection scheme at various time delays. By using sub–35 fs time resolution we hence obtained detailed temporal curves from which informations

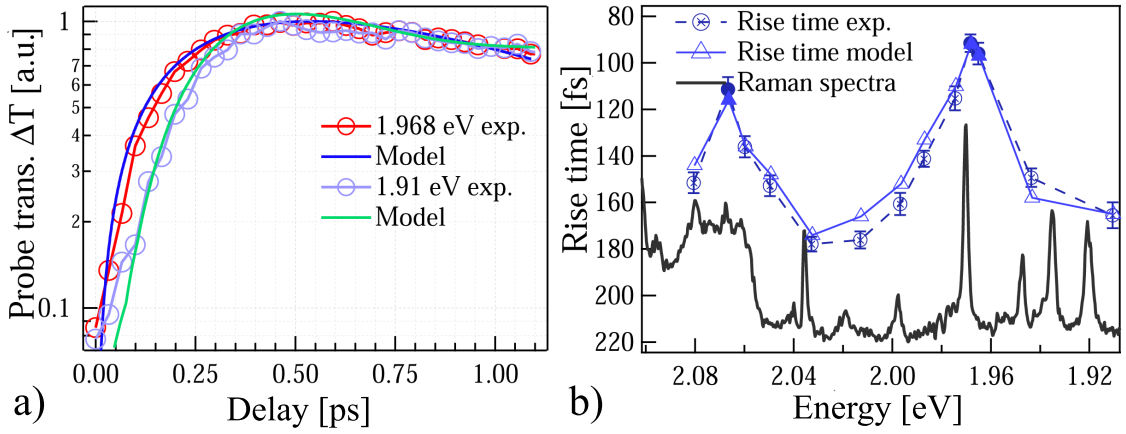

Figure 3.7: a) Variation of the transmitted signal intensity at different time delays, in and off resonance with the vibronic states. Modeled (solid line) and measured (circles line). b) Rise time values extracted from experimental (dashed line) and simulated (solid line) decay signals as presented in (a). Raman spectra is also displayed as a black line for comparison, scaled to the exciton reservoir energy.

on the polariton formation and decay were extracted. As such, by fitting the rise time of the measured transmitted signal we could confirm the theoretical simulation in which build-up times of the order of hundreds femtoseconds were predicted (figure 3.7). The slower decay tail was not directly reproduced by the simulation and therefore its characteristic lifetime, on the 10's of ps, was simply measured from the experimental data by a single decay exponential fit. While the ultrafast component reflects polariton build–up times from delocalized bright exciton states, signal decay relates to the scattering rate from all exciton reservoir states into the lower branch. More surprisingly, as shown in figure 3.7 **b**, a remarkable enhancement of the relaxation time into those LP states which met resonance conditions for scattering through molecular phonons was observed.
Both simulation and experimental findings indicate that vibrationally–assisted relaxation mechanisms prevail over other scattering processes and provide at the same time the most effective channel for macroscopic population of specific polariton states on the lower branch dispersion.

3.3.2 Effect of Molecular Disorder on the Light–matter Coupling

To account for the effect of high level of structural disorder on the light–matter coupling process we connect the number of coherently coupled molecules, experimentally measured in section 3.2.2, to the disorder parameter included in the model of the uncoupled J–aggregate system, introduced at first in chapter 2.3.1 (equation 2.4).
On a J–aggregate chain collective excitonic states can form through the mutual coupling of different localized excitations which possess on–site energy distributions defined by uncorrelated Gaussian with mean zero. The spread of the fluctuations, i.e. the variance

of the Gaussian (Δ), reflects the degree of disorder in the system which can be described by the dimensionless quantity d:

$$d = \frac{\Delta}{J} \tag{3.17}$$

where $J > 0$ is the nearest–neighbor coupling ($J = 0$ for any other interaction) [57, 113, 117]. The influence of molecular disorder is investigated by a study of the normalized oscillator strength (OSC) distribution [113] over the ensemble of collective states, assumed to be 100, together with the Participation Number (PN) which defines the number of molecules on which the exciton wavefunction is delocalized (figure 3.8). Here OSC is calculated by rescaling the oscillator strength of each molecule to the total number of states (100) over which is dispersed [113]. In the ideal case displayed in figure 3.8 **a** for $d = 0.1$, the oscillator strength is found to be localized on the low energy side of the molecular chain while exciton wavefunction extended on an average of 70 molecules (PN≈70) [114]. As the degree of disorder increases, the eigenenergies are strongly modified and important redistribution of OSC over the aggregate chain occurs. What follows is the corresponding optical activation of several excitonic states, previously optically inactive ("dark"), which acquire significant oscillator strength and contribute towards the strong coupling. In turn, the participation number decreases as the higher disorder induces localization. The number of coherently coupled molecules, identified with the value of 10 by Z–scan measurements, was directly used as an input to determine the level of system disorder d, which in sharp contrast to the commonly chosen value of d=0.1 has to be assume as 0.8 (figure 3.8 **d**).

There are two main consequences for the process of exciton–photon coupling that such analysis suggests. The first, unexpected, relates to the redistribution of the oscillator strength along the molecular chain. In fact, strong level of disorder allows for high energy states in the exciton reservoir to acquire enough oscillator strength to interact and couple with the electromagnetic field of the cavity and give rise to collective polariton eigenstates. Secondly and yet very important, is the fact that a highly disordered system which accomplish strong localization of the collective excitonic eigenstates directly cause an increase in the exciton–exciton mutual interaction coefficient. As the excitons are shared among only few monomers the phase space filling is achieved much easier with a corresponding increase of the nonlinear interaction. This can explain the high third–order optical nonlinearities experimentally observed for the TDBC cyanine dye which yet does not allow for the occurence of any polaritonic nonlinear phenomena.

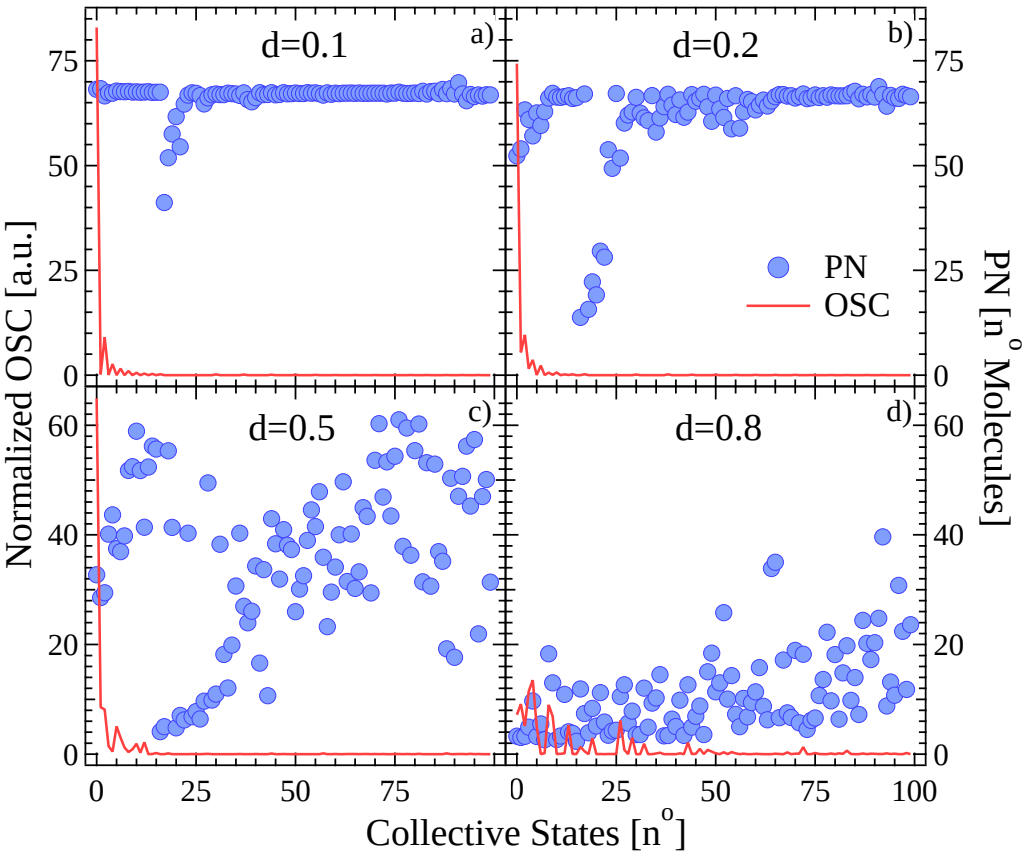

Figure 3.8: Normalized oscillator strength (OSC, red line) and Participation Number (PN, blue circles) distribution along the aggregate chain formed by 100 monomers. Each panel (**a**, **b**, **c** and **d**) relates to a different degree of disorder d.

4 Alternative Approaches

4.1 Introduction

As observed in the previous chapter, despite J-aggregate compounds possess relatively pronounced intrinsic nonlinearities, presence of reverse saturation of absorption limits the optical response of the dye and subsequent polariton properties when imbedded in a microcavity. To overcome these limitations we undertake an engineering approach which consists in the modification of the presented design with the introduction of additional organic compounds in the active region of the cavity to promote polariton thermalization on lower lying states by enhancement of the J–aggregate pumping efficiency as well as the relaxation mechanisms. In the first case the addition of a host dye characterized by strong emission and absorption maxima located far away from the high reflectance stop band allows for efficient intracavity pumping of the strongly coupled exciton–polariton states. The host polymer possesses weak oscillator strength and as such, does not contribute or alter strong coupling characteristic. On the other side, by including into the microcavity a second J-aggregate dye with different exciton energy, we allow for the formation of hybrid polaritons which retain properties of both coupled excitons. The presence of two exciton reservoirs as well as the emergence of an additional middle polariton branch increases the relaxation efficiency into the lower polariton states by opening new effective pathways.

We start our discussion with the intracavity pumped microcavities which are investigated by mean of angle resolved photoluminescence additionally combined with a study of the polariton occupation. Differently, the hybrid organic–organic microcavities are introduced with a description of the structure design and fabrication process, then characterized via reflectivity, photoluminescence excitation and time–resolved measurements.

All the samples analyzed and presented in this chapter were kindly provided by the group of Prof. David Lidzey at the University of Sheffield.

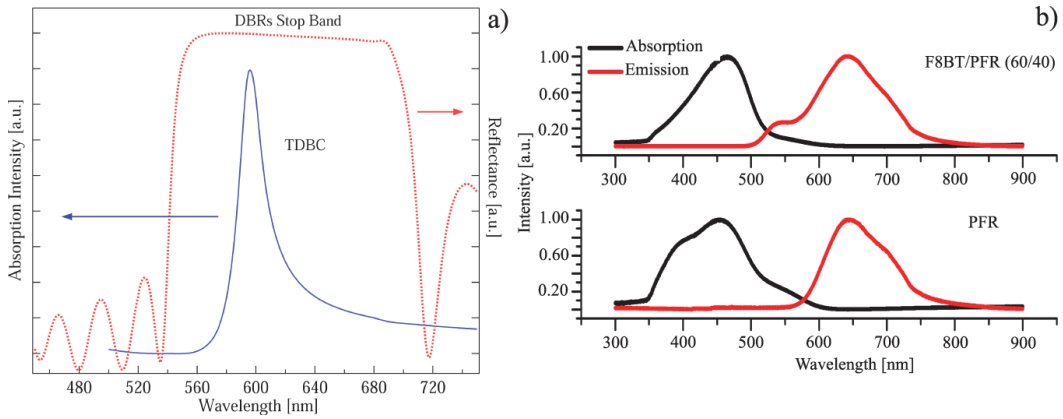

Figure 4.1: a) Absorption and reflectance spectra of the TDBC J–aggregate dye and bottom dielectric mirror used in the microcavity structure. b) Emission and absorption spectra of the polyfluorene dyes F8BT and PFR in a blend film and for PFR singularly.

4.2 Intracavity Pumped OMCs

One of the fundamental requirements for the achievement of coherent emission in inorganic and organic based microcavities is the fabrication of high quality mirrors (high Q factor) characterized by extremely high reflectance which endow polariton particles with long lifetime. By following such approach, one has to consider that J–aggregate compounds, most used semiconductor for organic microcavities, are characterized by very narrow absorption spectra and small stoke shift. Besides, absorption maxima is located inside the stop band and as such, efficient optical pumping is extremely difficult to achieve in high Q organic cavities. The possiblity to introduce a host dye which acts as cavity spacer and possesses strong emission in proximity of the maximum J–aggregate absorption permits to overcome the problem and to introduce at the same time additional advantages. Due to spectral overlap of the dye emission with the LP dispersion, direct pumping of polariton states occurs with important effect on the uncoupled exciton (ER) population which is consequently reduced. This represents an extremely favourable condition for enhancement of the polariton density of states towards the threshold required for observation of nonlinear processes. Remarkably, the maximum absorption energy of such dyes which is positioned far outside of the high reflectance region allows for simpler and most active optical excitation. To visually describe the situation just introduced we report in figure 4.1 **a** absorption spectra of the TDBC J–aggregate and DBR stop band reflectance together with emission/absorption spectra of the chosen pumping dyes (figure 4.1 **b**).

The first set of cavities was realized with a blended film of two polyfluorene dyes, commercially labeled F8BT and PFR (in percentage of 60 and 40 respectively) while the second set simply made by using PFR dye alone. All the samples were fabricated with dielectric distributed Bragg reflectors mirrors with identical characteristics of the one used for J–aggregate based microcavities analized in chapter 3; this to maintain similar

Q factor (about 300) and hence coupling conditions. Specifically, both mirrors consist of 11 alternated pairs of SiO_2 and Ta_2O_5 deposited by oxygen plasma sputtering on a glass substrate and on top of the organic layers. On the other hand, the cavity region was realized by spin casting the organic solutions directly on the bottom DBR: water based solution for the TDBC J–aggregate dye, previously introduced, while toluene based for the host dyes. In both cases the sample was heated on a hot plate at the temperature of 70^o Celsius for ≈3 minutes to assure complete solvent evaporation. The resulting active region is hence formed by two well defined films which absorption and emission features are described by a combination of the spectral characteristic of each compound. By changing the rotational speed we could also accomplish various film thickness values and therefore allow for a manifold detuning conditions. As it will be subsequently showed in the experimental discussion, this procedure would permit to tune energy position of the lower branch states and consequently couple maximum dye emission at ≈1.937eV (640nm) to chosen LP wavevectors for the most efficient pumping condition.

4.2.1 Characterization

All the microcavity samples were studied by means of angle resolved photoluminesce spectroscopy. This was performed by combining the experimental setup shown in Appendix A (7.2) with an excitation pulsed beam at 3.1 eV and 100 kHz repetition rate, shone on the sample at an angle of $\approx 30^o$ to avoid the collection of the scattered light. Besides, the sample, kept at room temperature, was vertically tilted to permit light collection in a solid angle centered at $\approx 10^o$. PL emission of the full dispersion, from low to high wavevectors, is in this way collected and complete information on polariton thermalization is accessible.
Photoluminescence images for microcavity samples containing both kind of host dyes (F8BT/PFR and PFR) and for different detuning conditions are displayed in figure 4.2. Panel **a** and **b** refer to small negative detuning values where upper polariton branch is also slightly visible, while **c** and **d** represent two very negative detuned cavities. In the latter cases the anticrossing point is located at high angles and therefore not clearly visible from the images. Using the coupled harmonic oscillator model a Rabi splitting value of approximately 130 meV was extracted for all the samples studied. From a first look at the images in figure 4.2 it is clear that there is strong polariton emission at the bottom of the LP branch, which suggests high occupation densities near $k_{||} = 0$ compared to the less bright high wavevector states. This remarkable feature is an indication of the effective intracavity pumping which sustains direct population of exciton–polariton states. Bypassing relaxation and subsequent scattering into and from the reservoir of uncoupled excitons (ER), as usually occurs under nonresonant optical pumping, thermalization and condensation of polariton particles at the bottom of the lower branch is very much favourite: the nonradiative decay losses which occur in the ER are reduced with strong enhancement of the polariton density of population. As observed in the images of figure

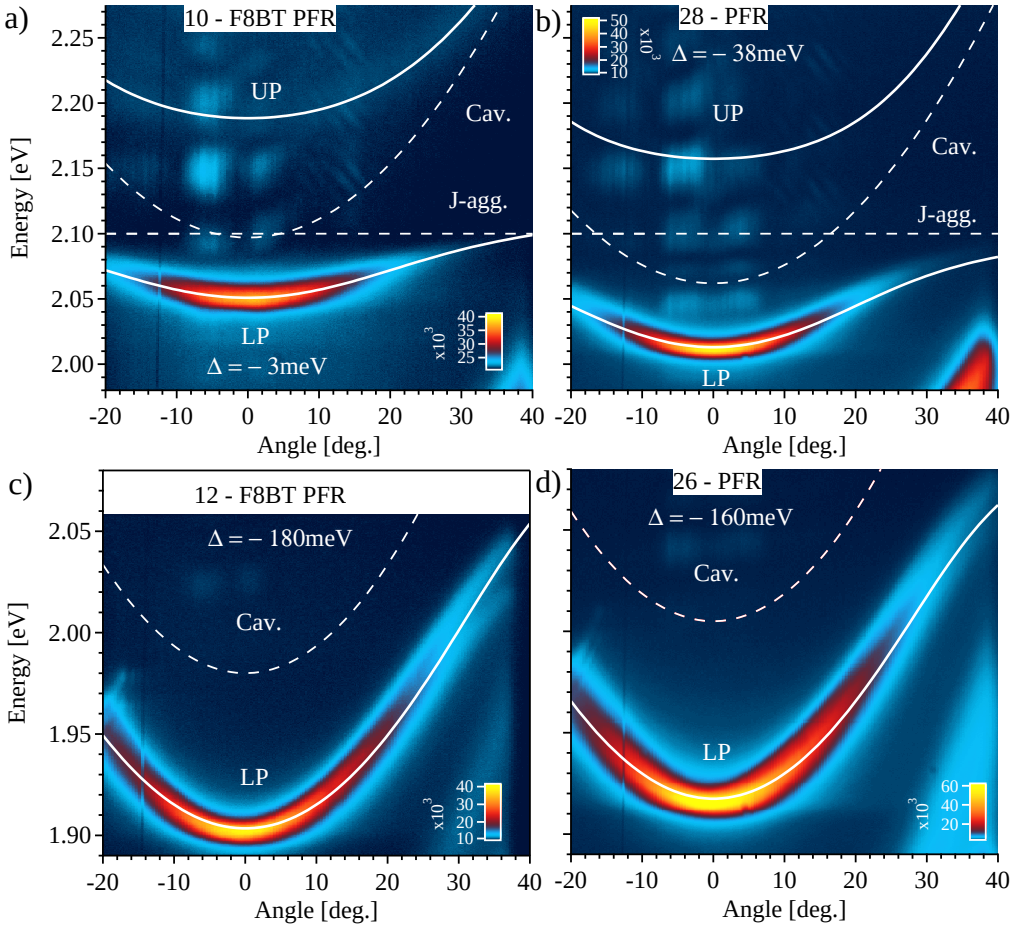

Figure 4.2: Angle resolved photoluminescence images for four different samples at various detuning conditions and hosting dye: (a), (c) containing the F8BT/PFR blend while (b) and (d) the PFR dye alone. J–aggregate exciton position, cavity and polariton branches, extracted from the coupled oscillator model, are also displayed as white dotted and continuous lines.

4.2 where a wide range of cavity detuning is explored, broad spectral linewidth of the host dye (≈0.25 eV) guarantees efficient polariton pumping even in those cases (small negative detuning) where LP bottom states are distant from the F8BT/PFR emission maxima (≈1.937 eV). Nevertheless, calculation of exciton–polariton occupation along the lower branch dispersion suggests that some detuning conditions are effectively more favourable than others. Measured photoluminescence polariton intensity along the LP is converted to the relative particle occupation number by taking into account the photonic/excitonic fraction, as known as the Hopfield coefficients, which changes with the increase of $k_{||}$, especially in case of very negative detuned cavities. As such, the observed counts of the lower branch polariton PL are extracted and subsequently divided by the photonic component calculated from the coupled oscillator matrix [118].

The obtained results are presented in figure 4.3 **a**. Here, the highest occupation number observed (purple line) is related to sample 26 which possesses a cavity detuning of -160 meV. Under this condition the lower polariton states are positioned at an energy of

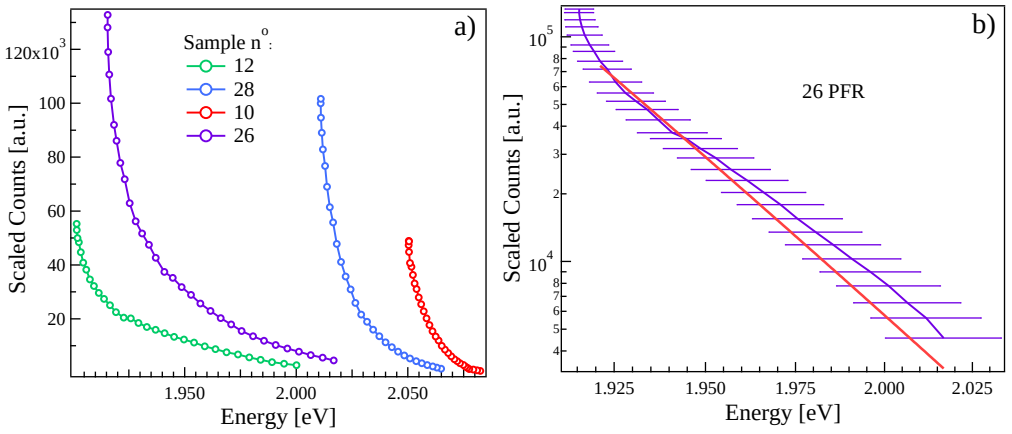

Figure 4.3: a) Lower branch exciton–polariton occupation number for the four structures previously introduced. b) LP occupation number of sample 26 fit with the Maxwell–Boltzmann distribution (red line) calcuted with a temperature of 345 Kelvin. Error bars refer to the lower branch linewidth.

≈1.92 eV, only 17 meV distant from the PFR emission maxima (1.937 eV) and thus providing the maximum pumping efficiency. Such detuning value specifically defines the most favourable condition for radiative population of polariton states and moreover provides indications on the correct approach to follow for further design improvements. It is worth mentioning that the second most efficient cavity detuning condition does not correspond to the detuning value of -180 meV but to a small negative one (-38 meV), where LP bottom states are located at the shoulder of the PFR emission spectra. We attribute this behaviour to the fact that in the case of Δ=-180 meV, resonant pumping of high wavevector states limits the fast thermalization at the bottom of the branch due to the inefficient polariton relaxation mechanism observed at low $k_{||}$. In such states in fact, particle character is dominated by the photonic fraction which reduces polariton scattering efficiency with consequent bottleneck formation [87].

To study the thermalization process into $k_{||} = 0$ we fit the occupation density curve extracted from the PL emission intensity of sample 26 with the Maxwell–Boltzmann (M–B) distribution $N(E_k) \propto e^{-E_k/k_BT}$ (E_k is the polariton energy and $N(E_k)$ indicates the number of particles per state at that specific energy). Figure 4.3 **b** displays the obtained results. Although there is a good agreement at the high energy tail of the LP dispersion, the high temperature value extracted from the fit (T=345 Kelvin) suggests that the polariton gas is not completely thermalized. This can be due to the mirror losses and to the big cavity size which reduce the overall Q factor and eventually the polariton lifetime.

Nevertheless, strong increase of population density on the states near $k_{||} = 0$, which is observed to occur near and above the polariton condensation threshold [29, 48], underline the effective improvement accomplished via the novel pumping scheme.

Following the positive trend of the obtained results we proceed with the investigation of angle resolved photoluminescence emission dependence on the optical excitation power.

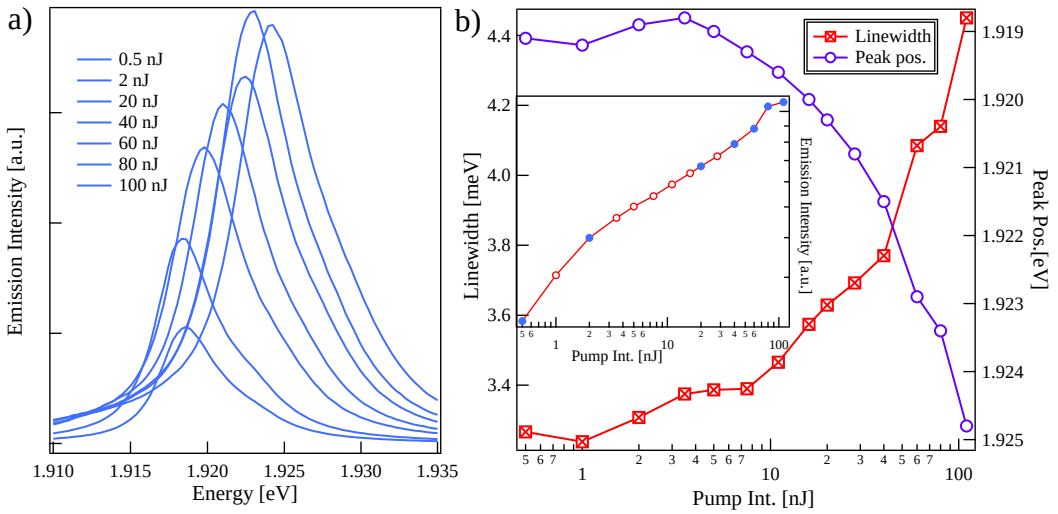

Figure 4.4: a) Photoluminescence profiles extracted at $k_{||} = 0$ on the lower polariton branch at different excitation powers. b) Peak position and profile linewidth as function of the applied power. Peak intensity dependence is also shown as inset.

No changes on the experimental setup were implemented. Figure 4.4 shows the results for this analysis on sample 26. Identical measurements were performed on all the remaining structures with the achievement of very similar results despite different detuning conditions. Evident from the pumping energy dependence of the emission intensity, linewidth and peak position, photoluminescence saturation is found to occur before the density threshold for stimulated scattering can be reached. In fact, by increasing the excitation power, polariton emission grows at first linearly and then sublinearly until a point where the system goes to the weak coupling regime (≈40 nJ). After that point PL intensity slightly increases due to the purely photonic contribution of the cavity mode and as a consequence peak position blueshifts and profile linewidth at $k_{||} = 0$ broadens.
Even if dye intracavity pumping strongly enhances the polariton states population and favours subsequent partial thermalization, small quantum yield of the host dyes and large cavity thickness does not allow polariton condensation. As a result, the intense pulse energies applied bring the system to the weak coupling regime which follows photobleaching of the J–aggregate molecules. This behaviour is also observed in classical organic microcavities which do not include additional emitting polymers. PL saturation and photobleaching occur by using either CW or pulsed excitations. Nevertheless, the remarkable improvement achieved by the inclusion of the emitting polymer and suggested by the presented results is related to the strong increase of the polariton population at zero wavevectors. This effect is uniquely due to the efficient pumping of the J–aggregate dye by means of the additional emitter which populates polariton states bypassing the loss mechanisms related to the exciton reservoir.

4.3 Hybrid Organic-Organic MCs

If from one side the polariton density in J–aggregate based microcavities, as showed in the previous section, can be strongly enhanced by mean of intracavity pumping mediated by an additional host dye, population distribution and relaxation pathways through the branches require further and deep investigations in order to overcome the basic limitations characteristic of these systems.
We present in this section a study of a novel planar microcavity structure which contains two organic J–aggregate dyes with different exciton energies, mixed together and simultaneously strongly coupled to the optical cavity mode with resulting formation of hybrid organic polaritons. The importance of the system resides in the fact that in such configuration, the particular polariton distribution has been found to favour the lower polariton branch population suggesting a strong relaxation pathway from higher energy states down to $k_{||} = 0$, through the exciton reservoirs. As explained in detail in the following part, angle resolved photoluminescence combined with photoluminescence excitation spectroscopy and reflectivity measurements enlighten such relaxation dynamics. Furthermore, additional time–decay analysis defines the characteristic scattering lifetimes and underlines the negligible contribution to the relaxation dynamics provided by direct Forster energy transfer process between the two different J–aggregate species which form the blended film.

4.3.1 Device Structure and Fabrication Process

The presence of two J–aggregate excitons in the active region of a strongly coupled planar microcavity allows for the formation of hybrid organic polaritons which simultaneously retain excitonic properties of both compounds as well as the photonic features of the optical mode responsible for the coupling. As previously reported for cavities made by two different energies quantum wells [119] or organic materials [120], such system can be studied via the three elements coupled harmonic oscillator where one photon couples at the same time with two uncoupled excitons:

$$\begin{bmatrix} E_c(\theta) & V_{ex1} & V_{ex2} \\ V_{ex1} & E_{ex1} & 0 \\ V_{ex2} & 0 & E_{ex2} \end{bmatrix} \begin{bmatrix} \alpha_\gamma \\ \alpha_{ex1} \\ \alpha_{ex2} \end{bmatrix} = E(\theta) \begin{bmatrix} \alpha_\gamma \\ \alpha_{ex1} \\ \alpha_{ex2} \end{bmatrix}. \tag{4.1}$$

Here, $E_c(\theta)$ is the cavity mode energy defined as $E_c(\theta) = E_0(1 - sin^2\theta/n)^{-1/2}$ where E_0 and n represent cutoff energy and cavity refractive index; V_{ex1} and V_{ex2} describe the interaction potentials between the photonic and excitonic modes while $E_{ex1/2}$ are the energies of unperturbed excitons. The solutions of the coupled matrix are defined by three polariton dispersions (upper, middle and lower) with energies given by $E(\theta)$. Branch anticrossing is expected to occur at the two uncoupled exciton energies and at the

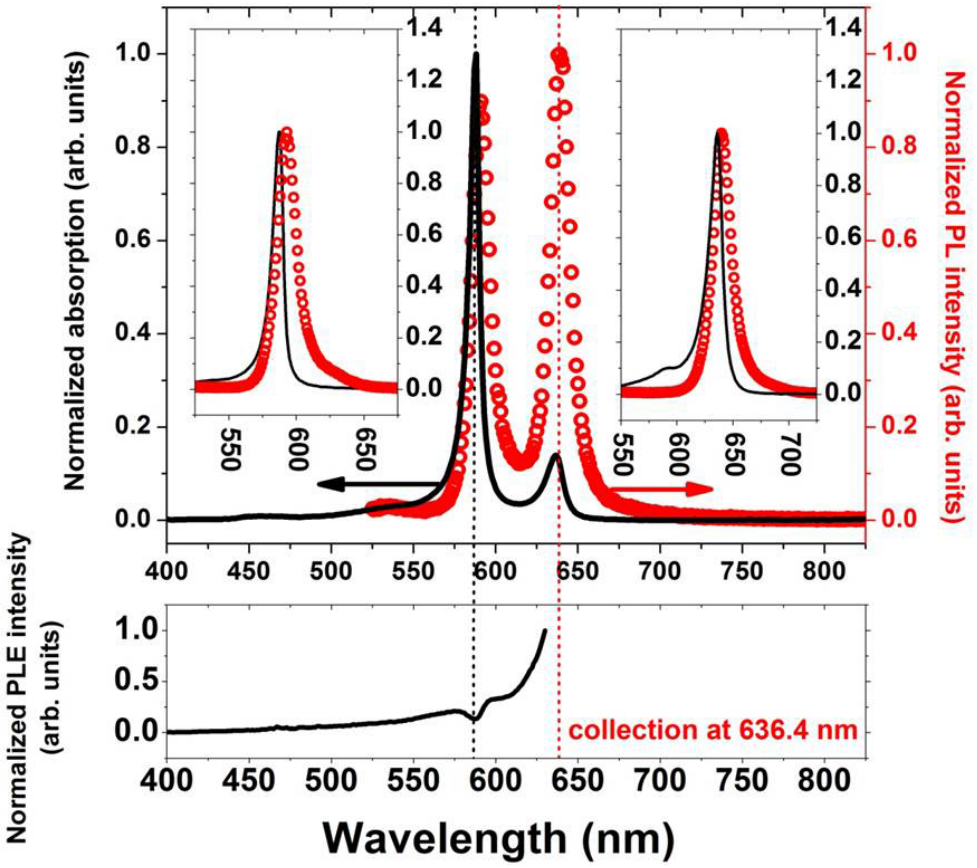

Figure 4.5: Normalized absorption (black line) and PL spectra (red circles) of a mixture of TDBC and NK–2707 in a gelatine matrix (ratio 3:1) with the absorption and PL of separate TDBC and NK-2707 films shown in the left and right insets respectively. The PLE spectrum, with detection at the PL peak of NK–2707 (636.4nm), is also shown in the bottom part of the graph.

specific wavevector which defines photon–exciton resonance. The complete description of photonic and excitonic weightings at each $k_{||}$ is given by the three mixing coefficient α_{γ}, α_{ex1} and α_{ex2}, basis functions of the coupled matrix. Full characterization of polariton energies and properties will be presented and discussed in the following section.

The microcavity structure studied here consists of two thermally evaporated silver mirrors (200 nm and 30 nm thickness for bottom and top) which comprise in between them the organic film formed by a mixture of both molecules. The two J–aggregate dyes used in this work are the previously described TDBC and the 5-chloro-2-[3-[5-chloro-3-(3-sulphopropyl-2(3H)-benzothiazolylidene]-2-methyl-l-propenyl]-3-(3-sulphopropyl) benzothiazolium hydroxide inner salt compound with triethylamine (NK-2707, Hayashibara Biochemical). Both dyes were individually dissolved in aqueous gelatine solutions (75 mg/ml) with a concentration of 5 mg/ml. After optical characterization the solutions were mixed together in the ratio 3:1 (TDBC:NK-2707) to scale the overall PL contribution due to smaller fluorescence quantum yield possesed by TDBC with respect to

NK-2707. The active layer is hence obtained by spin casting the resulting mixture on the bottom thick silver mirror. Absorption and emission spectra of both dyes are presented in figure 4.5 **b** (black line and red circles): TDBC exciton is positioned at 590 nm with a FWHM linewidth of 9.2 nm (16.1 nm FWHM of the photoluminescence spectra) while NK-2707 exciton shows maximum absorption at 636 nm with relative absorption and PL linewidth of 14.4 nm and 18.2 nm. As displayed in the central inset, by mixture of the dyes in a 3:1 ratio we could obtain similar PL intensities despite higher TDBC absorption maxima (6 times bigger than NK-2707) due to its greater concentration. The choosen configuration permitted to form an optical cavity where the confined $3\lambda/2$ mode is negatively detuned for both excitons

4.3.2 Characterization

The microcavity structures are optically characterized through photoluminescence (PL) and photoluminescence excitation (PLE) spectroscopy. In addition, normalized reflectivity R is also recorded with the same optical setup, fully described in Appendix A 7.5. In this way cavity absorption A was recovered by assuming absence of light transmission through the thick bottom mirror: $A = 1 - R$. The reason for such kind of measurements lies on the fact that PLE spectroscopy of a particular polariton state, in this case $k_{||} = 0$ on the lower polariton branch, is dependent upon the amount of light that can coupled into that state through the mirrors and from higher energy/wavevector states. Therefore, PLE is related to both the photonic and excitonic component of the polariton particle while reflectivity (absorption) only relates to the ability of the polariton state to couple to light, defined by its photonic weight. As such, by removing the photonic element simply dividing the PLE spectra by the calculated absorption spectra, only dependent on the photonic fraction, we can recover uniquely the contribution related to the excitonic component of the polariton, responsible of any particle–particle interaction. Therefore, the pure scattering efficiency from each state into the bottom of the lower branch is obtained.
After the initial characterization of both dyes, isolated and mixed, via absorption and PL spectroscopy, we performed PLE on a reference film of the J–aggregates blend with collection on the NK–2707 exciton energy to study possible molecular energy transfer. As reported in figure 4.5 **c**, the small dip in intesity located at the TDBC absorption peak suggests the very weak or even absence of energy transfer between the dyes outside the cavity. This conclusion is furthermore supported in the next section when time decay curves of both mixture and single dye films will be presented: the small change in the TDBC lifetime when blended with NK–2707 indicates that the former does not act as donor and neither the latter as acceptor. We speculate that the limited energy transfer between the components in the control film results from the fact that phase–separation in the blend film creates almost "pure" aggregates of TDBC and NK–2707 that are phase–separated within the insulating gelatine matrix with a length–scale sufficiently

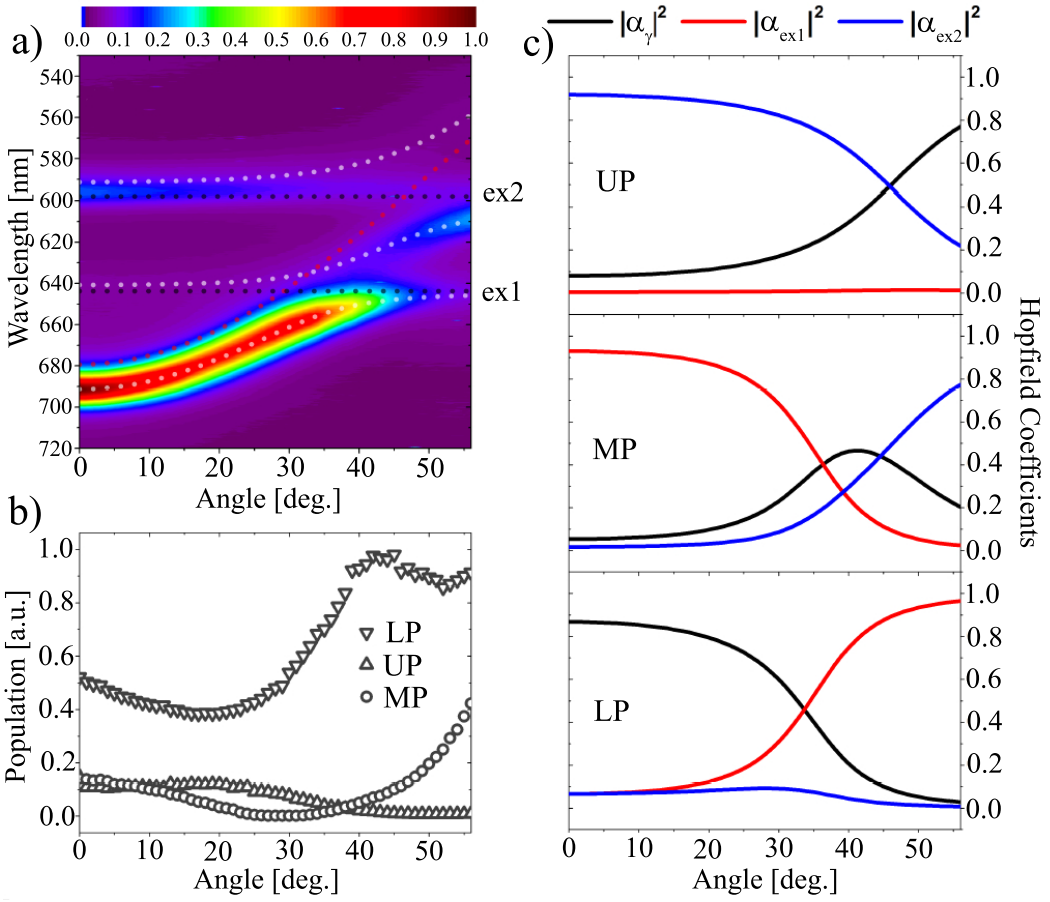

Figure 4.6: a) Angle resolved photoluminescence image. Exciton energies, cavity mode and polariton branches extracted from the coupled oscillator model are displayed on top as black, red and white dotted lines. b,c) Polariton population distribution extracted from the PL intensity in image (a) and mixing fractions for each branch.

large to prevent direct dipole–dipole interaction. Results and related discussion of the optical study accomplished on the full hybrid microcavity structure are presented below. The angular dependent photoluminescence emission is displayed in figure 4.6 **a**. It can be observed that polariton emission, stronger at small angles on the lower branch, becomes more pronounced on the middle for angles above 40^o. Reflectivity spectra for a broad range of angles are presented in figure 4.7 which in a similar manner, show the behavior just described: the LP deep, very pronounced at low wavevectors, decreases at higher angles accompanied by an increase of the MP and UP deeps.

To precisely define exciton and photon energies, polariton branches and mixing coefficients at each $k_{||}$, we fit the PL spectrum with a series of Lorentzian peaks (3 for the polariton branches and 2 for the weakly coupled exciton reservoirs) which are subsequently used to reproduce relative dispersions by mean of equation 4.1. Accordingly to the model, we find that at normal incidence the photon energy is 101 meV below the NK–2707 exciton (ex1) and 250 meV below the TDBC exciton (ex2). A Rabi splitting energy of $2V_{ex1}$= 73 meV is seen between the LP and MP, while the larger splitting of

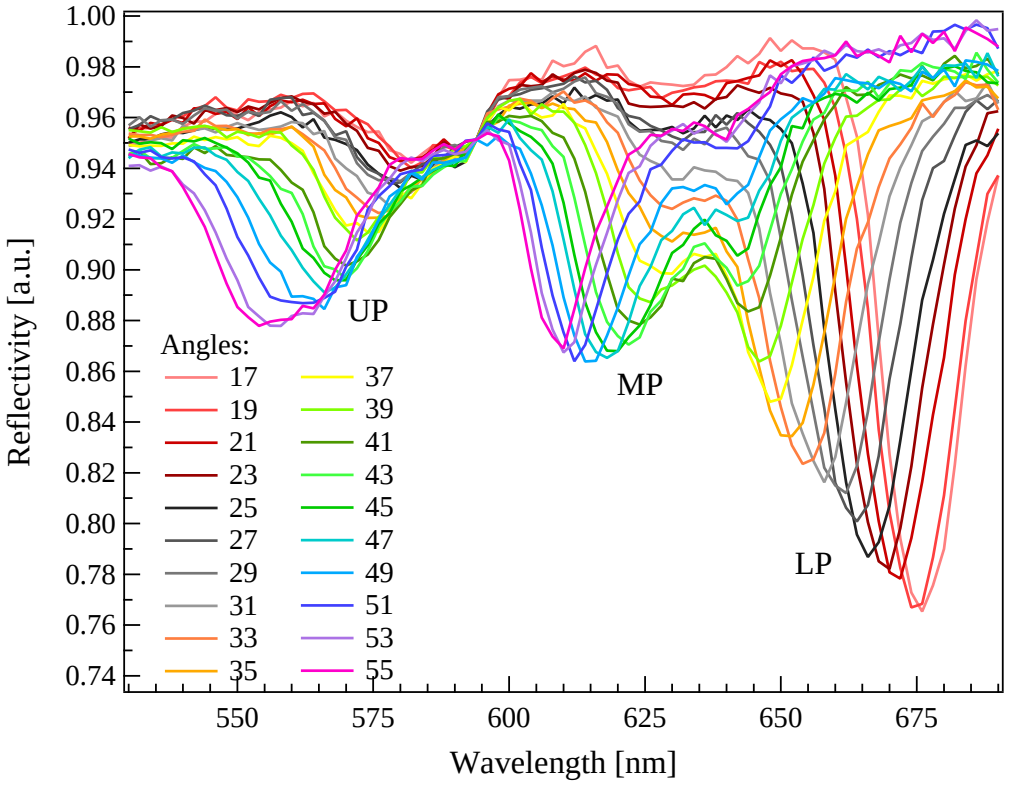

Figure 4.7: Reflectivity spectra at different angles from which the absorption image is extracted. Upper (UP), middle (MP) and lower (LP) polariton branches clearly show the typical anticrossing behavior expected for the strongly coupled system.

$2V_{ex2}$= 155 meV between the MP and UP is motivated by the higher TDBC oscillator strength. Furthermore, population density P_{pol} along the polariton branches can be studied by converting peak emission intensity I_{pol} through the following:

$$P_{pol} \propto \frac{I_{pol}}{|\alpha_\gamma|^2}. \tag{4.2}$$

The relative population dispersions are shown in figure 4.6 **b**. The most interesting features are related to the LP population which presents the general trend of increasing with increasing emission angle. This effect is well documented [46, 90] and is due to the role played by the exciton reservoir in populating polariton states. Following nonresonant pumping, excitons relax through interactions with molecular vibrations into the J–aggregate J–band and form a weakly coupled reservoir of thermalized exciton states. These reservoir states populate the polariton states via two mechanisms. Firstly, as reported in the previous chapter (3) excitons can "dump" energy into molecular vibrations and scatter into lower energy states or gain energy from vibrations to be promoted into higher energy polariton states. The excitons may interact with a low energy continuum of molecular vibrations (usually considered to have energy <10 meV), or higher energy discrete vibrational modes. Remarkably, these scattering processes are limited

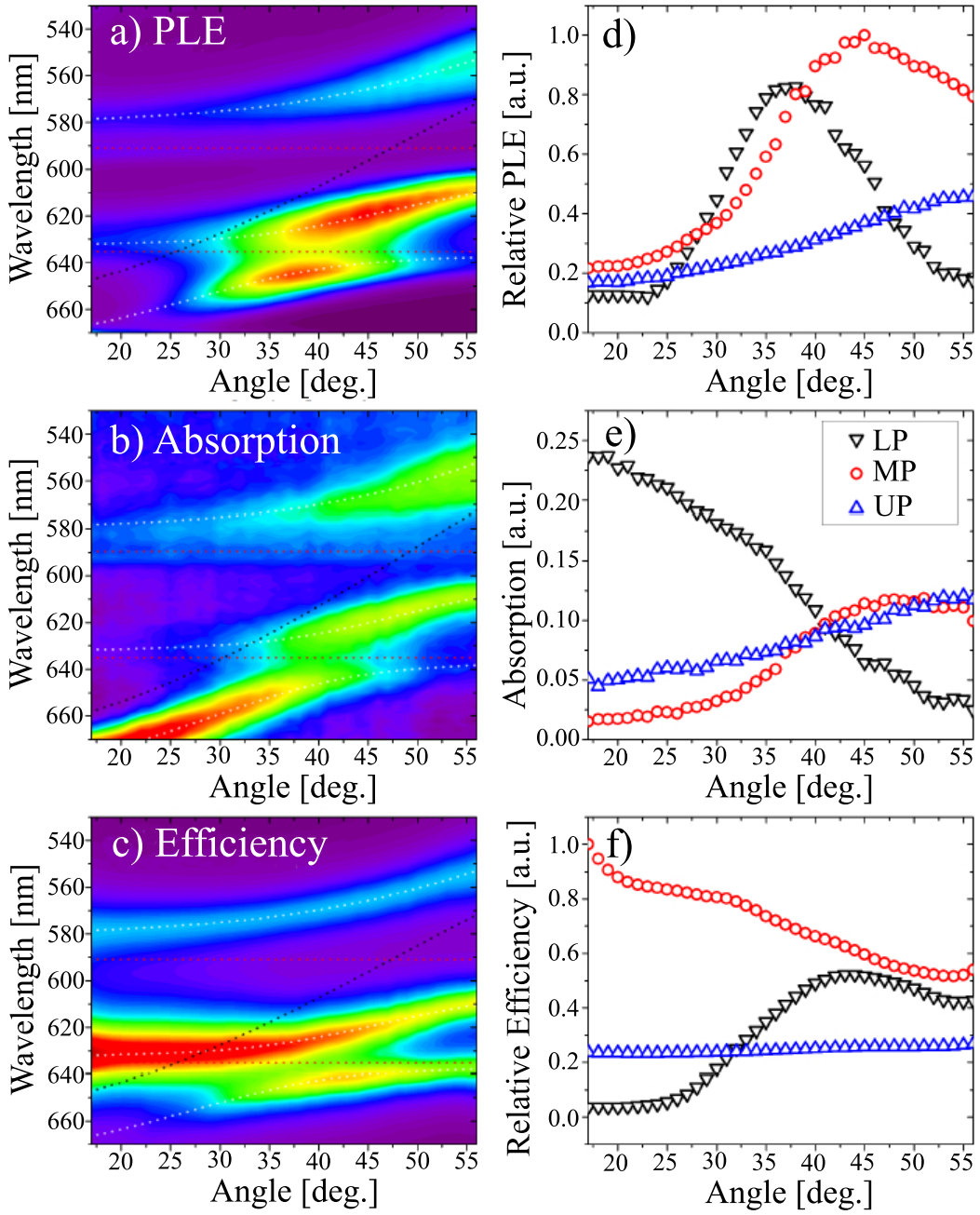

Figure 4.8: a) Angular dependent PLE signal recorded at $k_{||} = 0$ on the LP. b) Angular dependent absorption. c) Angular dependent relative scattering efficiency to $k_{||} = 0$ on the LP. The magnitude of the PLE, absorption and efficiency for each branch are shown in parts (d), (e) and (f) respectively. Red, white and black dotted lines refers respectively to the fitted exciton energies, polariton and cavity dispersions.

by the short polariton lifetime which relates to J–aggregate exciton and cavity lifetime, the first of the order of 10's/100's ps while the second, accordingly to a generally poor cavity quality factor, ≈10's fs. As such, multiple scattering is strongly suppressed and polariton particles remain confined to states close to the reservoir. Nevertheless, highly energetic discrete vibrations can act as fast relaxation mechanism to populate polariton

states far below the exciton energy [1].
The second mechanism which involves exciton reservoirs is "optical pumping": weakly coupled excitons directly populate the photonic components of polaritons through their radiative decay. This is an elastic process so only polariton states that overlap with the reservoir emission are populated in this way. Again, this is limited to states close to the reservoir. Despite the fact that similar reservoirs of ex1 and ex2 excitons are available to populate both lower and middle polariton branch, we find that the relative population of polaritons in LP is significantly greater than that in either UP or MP at all angles. This observation provides qualitative evidence for an efficient energy relaxation pathway that depopulates both UP and MP.
We can study the efficiency of such relaxation process by using PLE spectroscopy. The PLE signal recorded at normal incidence ($k_{||} = 0$) on the lower polariton dispersion is plotted in figure 4.8 **a** and the PLE intensity for each branch (found by Lorentzian fitting) in panel **d**. Starting from the upper branch, we notice that PLE is weak in the proximity of zero degree states and increases with increasing angle. The MP PLE signal also increases with increasing angle but shows a broad peak centered at 45^o. Finally, lower branch PLE signal, weak at small and large angles, presents a strong peak at 37^o. As already described at the beginning of our discussion, to account for the photonic component inherent in the PLE signal we simultaneously measure the angular dependent microcavity absorption. This is shown in figure 4.8 **b** and the magnitude plotted in panel **e**. The UP absorption follows the same trend as the UP PLE signal, while the MP absorption is similar to the MP PLE but with a less pronounced change in magnitude. In contrast, the LP absorption is markedly different from the LP PLE signal. The former, as expected, is in fact strong at small angles and reduces with increasing angle following the photonic fraction of the related polariton particles. Therefore, by dividing the PLE signal by the absorption, we obtain a measure of the scattering efficiency of each polariton state into the bottom of the lower branch dispersion. This is plotted in figure 4.8 **c** with the magnitude of each branch reported in panel **f**.
From a first look at the UP we notice a constant scattering efficiency with respect to the angle. This has been observed in PLE measurements on single exciton cavities and it is attributed to a fast scattering of UP polaritons into the exciton reservoir (on the order of 10's fs) before scattering into lower energy polariton states [45]. Since this scattering rate is faster than the polariton radiative emission rate for all angles, we assume that polaritons can effetively relax to the reservoir from all states on the UP. Once in the reservoir, the excitons lose information about the original polariton state and for this reason it is therefore the scattering efficiency from the reservoir we measure, not from the UP states. Hence, since excitons in the reservoir carry no dispersion and can be considered indistinguishable, the scattering efficiency is constant with angle. The middle polariton scattering efficiency instead, decreases constantly with increasing angle. This behaviour suggests that there must be some other mechanism at play besides scattering to the NK–2707 reservoir followed by scattering to LP. Direct scattering from the MP

to LP is the most likely candidate. In fact, from a look at the mixing fraction related to MP, we observe that the first excitonic component $|\alpha_{ex1}|^2$ strongly dominates at small angles up to $\approx 30^o$. Besides, since polariton particles scatter through their excitonic fraction and the rate of such process is proportional to the overlap of similar exciton mixing fractions in the initial and final states, we can assume that strong and efficient scattering from MP to the NK–2707 reservoir as well as direct scattering from MP to LP states will be increased at small angles. Considering now the lower branch, we notice that the peak seen at first in the PLE signal is not reproduced in the LP absorption; hence the PLE peak is still present in the efficiency, albeit less pronounced. We explain the presence of such strong feature as interplay between two different processes. Firstly, a bottleneck effect due to the increase of the photonic character of polariton particles that scatter down the LP (figure 4.6 **e**). In fact, since polaritons particles interact through their excitonic component while their radiative decay rate is proportional to their photonic fraction, scattering is suppressed towards small angles and radiative decay rates increased, forming a bottleneck region that polaritons cannot easily scatter through. Secondly, we believe that the reduction in the PLE signal towards high angle is due to thermal scattering of polaritons back to the exciton reservoir. Such decrement, in fact, is not observed in a single TDBC exciton cavity due to the impossibility of lower branch polaritons in the high energy states, to jump back in the ER, located much farther with respect to the hybrid system.

After the discussion of the various relaxation pathways and their efficiency, we now proceed with the interpretation of the observed angular–dependent polariton PL intensity shown previously in figure 4.6. We perform such analysis through a simple model based on a series of rate equations which accounts for the processes that populate and deplete states along each polariton branch. Assuming a rapid thermalization of the molecular excitation which follows a non resonant pumping, the steady state exciton reservoirs population can be considered as constant [117]. We describe the time–dependent change of the polariton population N in the lower, middle and upper banches, through the equations 4.3, 4.4 and 4.5 which are solved at the steady state conditions.

$$\frac{\partial N_{LP}}{\partial t} = C_1 \left|\alpha_{ex1}^{LP}\right|^2 (B_1+1)(\frac{\Delta E_1}{J})^{p1} + C_3 P_{LP} \left|\alpha_{\gamma}^{LP}\right|^2 - N_{LP} C_4 \left|\alpha_{\gamma}^{LP}\right|^2 - N_{LP} C_5^{LP} R_{LP} \tag{4.3}$$

$$\begin{aligned}\frac{\partial N_{MP}}{\partial t} = {} & C_2 \left|\alpha_{ex2}^{MP}\right|^2 (B_2+1)(\frac{\Delta E_2}{J})^{p2} + C_1 \left|\alpha_{ex1}^{MP}\right|^2 B_1 (\frac{\Delta E_1}{J})^{p1} \\ & + C_3 P_{MP} \left|\alpha_{\gamma}^{MP}\right|^2 - N_{MP} C_4 \left|\alpha_{\gamma}^{MP}\right|^2 - N_{MP} C_5^{MP} R_{MP}\end{aligned} \tag{4.4}$$

$$\frac{\partial N_{UP}}{\partial t} = C_2 \left|\alpha_{ex2}^{UP}\right|^2 B_2 (\frac{\Delta E_2}{J})^{p2} + C_3 P_{UP} \left|\alpha_{\gamma}^{UP}\right|^2 - N_{UP} C_4 \left|\alpha_{\gamma}^{UP}\right|^2 - N_{UP} C_5^{UP} R_{UP}. \tag{4.5}$$

The equations also include the following term:

$$B_\sigma = \left(exp\left[\frac{\Delta E_\sigma}{kT} - 1\right]\right)^{-1}, \Delta E_\sigma = |E_{pol} - E_{ex\sigma}| \tag{4.6}$$

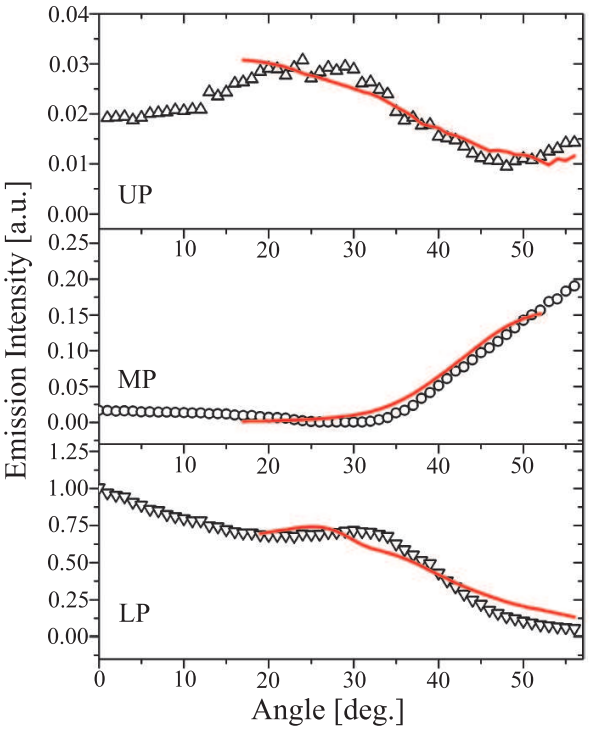

Figure 4.9: Polariton emission intensity (open symbols) and modeled intensity (red solid lines) for the UP, MP and LP.

with σ=1 or 2. These equations are not directly coupled as direct inter branch relaxation is prevented as it is very much slower than (in the linear regime) polariton radiative decay or non–radiative relaxation to exciton–reservoir states at lower energy. The equations instead describe the population exchange between the polariton branches and the two exciton reservoirs. Solving for the steady state condition we fit the predicted polariton photoluminescence emission to the experimental data in figure 4.9.

In all three equations are terms that account for the scattering from exciton reservoir ex_σ to a polariton branch, mediated by the absorption ($\propto B_\sigma$) or emission ($\propto 1 + B_\sigma$) of a molecular vibration, where the "thermal bath" of molecular vibrations is populated according to the Bose–Einstein distribution. These terms are proportional to the parameters C_1 and C_2 when describing exciton reservoirs $ex1$ and $ex2$ respectively, and scale with the excitonic component $|\alpha_{ex\sigma}|^2$ of the polariton (as scattering preferentially occurs into exciton–like states). These terms scale with the polariton exciton energy separation $|\Delta E_\sigma|$, with scattering being more rapid for larger energetic separations. This process is introduced in a phenomenological way [117] so that the terms are proportional to $(\Delta E_\sigma/J)^{p_\sigma}$, where $J = 75$ meV, with p_σ left as a fitting parameter [117]. The LP (UP) mainly contains $ex1$ ($ex2$) excitons, therefore equation 4.3 (4.5) accounts only for the scattering from the $ex1$ ($ex2$) reservoir. The MP has an intrinsic hybrid nature and

$C_1 = 5.64X10^2$	$C_5^{LP} = 1.28X10^{-1}$	$p_1 = 1.80X10^0$
$C_2 = 1.14X10^3$	$C_5^{MP} = 1.22X10^1$	$p_2 = 0$
$C_3 = 1.18X10^1$	$C_5^{UP} = 4.26X10^0$	
$C_4 = 2.01X10^{-2}$		

Table 4.1: Fitting parameters used in equations 4.3, 4.4 and 4.5 to produce the measured PL emission displayed in figure 4.9.

can therefore exchange particles with both $ex1$ and $ex2$ exciton reservoirs, creating a relaxation pathway between the two exciton species.

The terms proportional to the parameter C_3 describe the direct optical pumping of polariton states through radiative decay of weak–coupled excitons in the exciton reservoir, with the emitted photon being absorbed by the photonic component of a polariton state. This process is known to be important in populating polariton states that are close in energy to the reservoir. We describe this term as the product of the photon fraction mixed into the polariton branch $\left|\alpha_\gamma^X\right|^2$, where X = LP, MP or UP, with the relative PL intensity $P_X(\theta)$ from the reservoirs (determined from a non-cavity control film) at each particular polariton energy. We normalize the total PL overlap such that $\sum_X^{LP,MP,UP} \int_{17^o}^{56^o} P_X(\theta)d\theta = 1$. The term described by constant C_4 represents radiative decay of polaritons and is proportional to the photon fraction of each state.

The final term (including the fitting constant C_5) describes polaritons non–radiative scattering to the exciton reservoir; a fast process compared to polariton–polariton scattering (especially for states along the UP and MP) [117]. We describe the relative efficiency of the relaxation process $R_X(\theta)$ using the measured PLE relaxation efficiency data for each polariton branch as a function of angle as plotted in figure 4.8 **f**. We normalize R_X for each branch such that $\int_{17^o}^{56^o} R_X(\theta)d\theta = 1$. The measured PLE relaxation efficiency data describes the efficiency by which any polariton state relaxes to the bottom of the LP (passing through the exciton reservoirs), and its use here to describe the overall probability that any polariton state along the LP undergoes any form of energetic relaxation, it is clearly an approximation.

We solve these equations to determine N for each branch as a function of angle. The photoluminescence intensity from the cavity can then be calculated as a function of angle using equation 4.2. We summarise the parameters used in our model in table 4.1. We note that the fitting value of $p2$ is zero, which is mainly due to the relative small energy separation between the exciton reservoir $ex2$ and the polariton states of UP and MP, which does not allow us to accurately determine this parameter. For the LP, the relatively large energetic separation from the $ex1$ exciton reservoir allows us to determine a finite value for $p1$.

A key results of the model is the ability of excitons to relax to and from states in the middle polariton branch (MP), with such states effectively acting as a pathway between the exciton reservoirs. Indeed, our model indicates that states in the MP are mainly populated via direct scattering from the $ex2$ reservoir and then are depopulated by both

radiative emission and relaxation to the lower–lying $ex1$ reservoir, with the relaxation time of polaritons to $ex1$ predicted to be $\leq$10 fs. Our model also indicates that the number of $ex2$ polariton states that scatter from the MP to the $ex1$ reservoir is greater than 95%; a result that explains the strong suppression of luminescence from most of the middle branch. The good fit between the simple phenomenological model we have described and the PL measurements (figure 4.9), allows us to present the following picture describing the relaxation dynamics in this hybrid polariton system. The UP is populated by both optical pumping and thermal promotion of excitons from the $ex2$ reservoir. The relaxation of UP polaritons to the $ex2$ reservoir is much faster than its radiative emission rate. Indeed, the model suggests that the radiative decay channel is only responsible for depopulating 5% of the polaritons in this branch. The MP is almost entirely populated by the scattering from the higher energy $ex2$ reservoir while it is depopulated through two competing processes: non–radiative relaxation into the $ex1$ reservoir and direct radiative emission. Again we find that non–radiative relaxation accounts for the depopulation of over 95% of the polaritons in this branch. Our results indicate therefore that once an $ex2$ exciton scatters to an MP state, it is highly likely to relax to the $ex1$ reservoir and hence the MP has the crucial function of exchanging population between the two exciton species. Finally, the LP is populated by both scattering and optical pumping from the $ex1$ reservoir.

4.3.3 Energy Transfer and Time Resolved Measurements

The last step in the investigation of exciton relaxation mechanisms and pahtways which follow non resonant excitation of organic–organic hybrid microcavities, is the study of the time resolved polariton emission. Through this analysis we could address the scattering processes discussed in the previous section with their temporal behaviour and hence complete their description. However, a preliminary analysis on the lifetime of both J–aggregate excitons outside the cavity has to be pursued.

Time resolved emission of bare TDBC and NK-2707 J–aggregate films is performed to clarify the presence and role of energy transfer in between the molecules. A simple comparison of these exciton lifetimes with the ones extracted from a film of a mixed solution of both compounds (ratio 3:1) will provide the required informations. The four decay curves are plotted in panels **a** and **b** of figure 4.10 where black circles refers to the single excitons while the red to the blended. From the biexponential decay fits of the experimental curves referred to the isolated compounds it appears that TDBC exciton lifetime is characterized by a fast and a slow component, respectively of 7 ps and 21 ps. NK–2707 excitons instead, posses a longer lifetime which is still defined by a fast and a slow part of 12 ps and 59 ps. It has been suggested that the fast component is due to exciton–exciton annihilation process that occurs at high excitation densities [121] while the slow refers to radiative emission.

We consider now the time resolved emission of both excitons when mixed together in

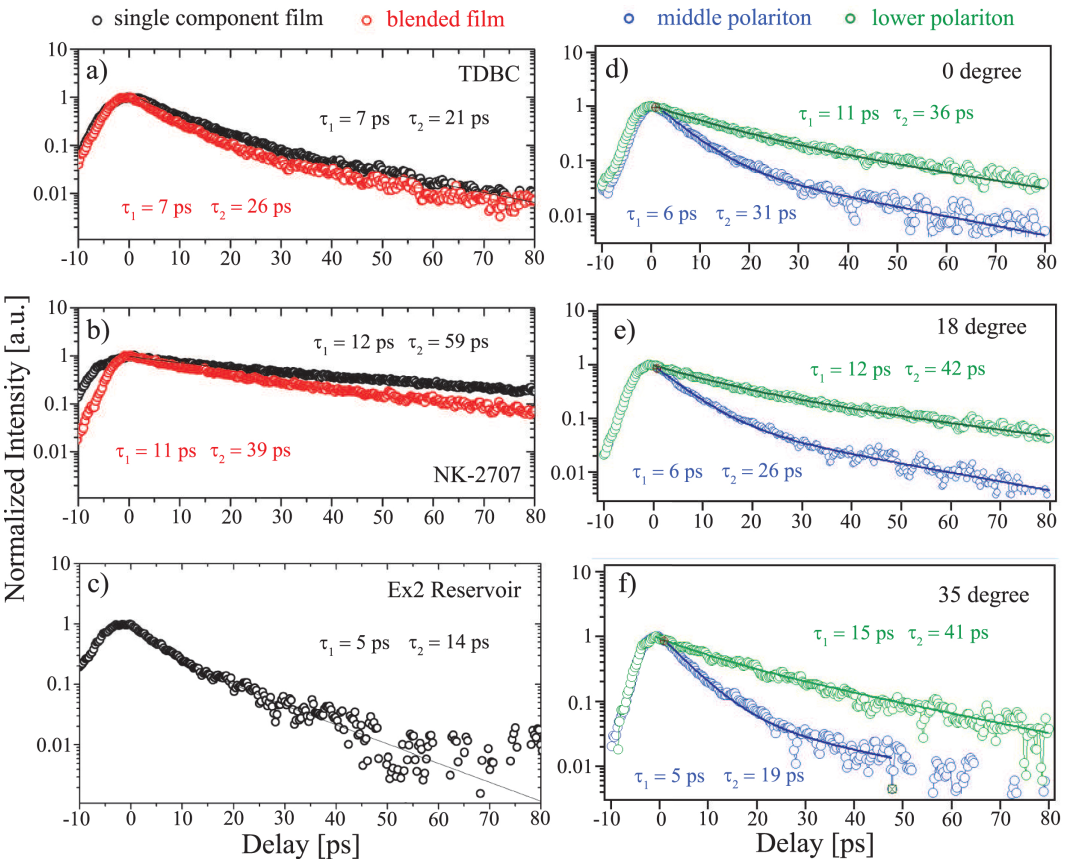

Figure 4.10: Time decays of (a) TDBC (at 587 nm) and (b) NK–2707 (at 636 nm) in single component (black circles) and blended (red circles) films. c) TDBC reservoir emission decay recorded from the cavity sample. Polariton emission decays are also displayed for LP (green circles) and MP (blue circles) at (d) 0^o, (e) 18^o and (f) 35^o.

the same solution (red circles). Specifically we find that the fast component of the TDBC decay possesses the same value (within the resolution of the detector, 3 ps) as extracted from the single compound, while the slow part appears slightly longer lived in the blended film. This modification confirms our previous assumption that excitons are not migrating from TDBC to the longer wavelength NK–2707 compound, i.e. energy transfer does not occur. In fact, the presence of such process would have been manifested by a remarkable shortening of the donor lifetime (TDBC) due to the fast transfer of electronic excitation to the acceptor chromophore (NK–2707) [122]. On the other hand, in case of NK-2707, the fast component seems again insensitive as to whether is in the single or blended film, while a distinct reduction of the slow component occurs (from 59 ps to 39 ps). The nature of this effect is not completely understood, however we speculate that the size of the aggregate domains may differ in the blend film compared to the pure film. If the NK–2707 aggregates are smaller in the blend, then there may well be additional quenching processes that occur that are associated with electronic states at the edge of an individual aggregate.

Additional informations of TDBC exciton lifetime can be extracted by the study of the

emission decay of the uncoupled reservoir states, recorded at 595 nm from the strongly coupled microcavity sample. As reported in figure 4.6, the strong photoluminescence of uncoupled TDBC excitons allows their study also when imbedded in a cavity. From the fit of the decay curve shown in figure 4.10 **c** we extract a value of the slow component which is 7 ps faster with respect to the bare film (from 21 ps to 14 ps). The presence of an additional non-radiative decay mechanism, specifically defined by exciton scattering into polariton states, explains the observed change in the lifetime.

At last, polariton emission is time resolved at specific angles (0^o, 18^o and 35^o) on the middle and lower branch dispersions. The results of such analysis together with relative biexponential decay fits are displayed in figure 4.10 **d**, **e** and **f**; blue and green circles refer respectively to MP and LP. At first we notice that, as observed for TDBC and NK–2707 excitons, also LP and MP decays are characterized by a slow and fast component which is due to exciton–exciton annihilation in the uncoupled reservoir states and therefore not related to polariton decay processes. Specifically to the lower branch emission, we find that the lifetime remains approximately constant (to within 5 ps) at the angles observed. Besides, since the lifetime is measured relative to the arrival of the excitation pulse, this must be seen as the sum of the scattering lifetime into the polariton state plus their intrinsic lifetime. For this reason, the fact that measured lower branch polariton lifetime closely approach the values obtained for the NK–2707 reference film (figure 4.10 **b**) supports our assumption that LP states are populated primarily through scattering from the ex1 reservoir (NK–2707). The shorter polariton lifetime observed, compared to the bare excitonic states, has to be addressed to the fact that polariton particles lifetime is dominated by the short cavity one (10's of fs) which compensate the longer lived exciton component. Following the same trend, middle branch polaritons show an overall shorter lifetime which relates to the one of the proximate TDBC reservoir. Moreover, different population processes which dominate at high and low wavevectors on the MP dispersion are reflected into noticeable decrease in the polariton lifetime at increasing angles. Considering that at large $k_{||}$ MP states are mostly populated through optical pumping from the ex2 reservoir excitons it follows that polariton lifetime tends to converge to the radiative TDBC reservoir lifetime (figure 4.10 **c**). On the other hand, polariton states further down the middle branch are not optically pumped and instead mostly populated from the ex1 reservoir by thermally assisted scattering. As a result their dynamics follow the decay of the ex1 (NK–2707) excitons (31 ps versus 39 ps). This population process is made possible as the energy separation between the MP branch and the ex1 reservoir at 0^o is <10 meV, a value smaller than kT at room temperature (26 meV).

Following the discussion on PL and PLE measurements on a hybrid organic–organic microcavity and subsequent study of J–aggregate excitons and polariton lifetimes we can conclude that the presence of two different strongly coupled excitonic species creates favorable conditions for the efficient relaxation of the polariton population into the lower

branch. Through PLE spectroscopy on the $k_{||} = 0$ states on the LP we demonstrated that relaxation dynamics involve the entire system, comprising high energy states on the upper dispersion. Such relaxation channels involve principally the middle polariton branch which has been observed to mediate between the two exciton reservoirs allowing for a long range energy transfer from one J–aggregate specie to the others. Therefore, we acknowledge the presence of multiple strongly coupled excitons as a remarkable improvement to the relaxation efficiency and final population of $k_{||} = 0$ polariton states in J–aggregate based microcavities.

In this chapter we have demonstrated that introducing in the cavity a host dye to directly pump the J–aggregate dye or creating hybrid polaritons via photon coupling with a mixture of two J–aggregate species provides a successful route to overcome the intrinsic limitations of organic microcavities which active layer is formed by a single specie. On one side intracavity pumping of the J–aggregate dye by means of an ultra–bright optically inactive host dye allows for a remarkable enhancement of the polariton population which results in the experimental observation of thermalized exciton–polaritons at the bottom of the lower branch, phenomena not visible in the organic MCs studied in Chapter 3. Further more, the presence of two different active dyes which simultaneously couple to the optical mode allows for an efficient polariton relaxation at the bottom of the lower branch through a long range energy transfer which involves multiple scattering between the upper, middle and lower branches with the two different exciton reservoirs.
The realization and study of a new microcavity structure which simultaneously exploits these two concepts for even further improvements is presented in the following chapter.

5 Hybrid Organic Inorganic MCs

5.1 Introduction

Most of the impressive and fascinating results published in the past twenty years which involve strong light–matter coupling in planar microcavities, were achieved by exploiting inorganic semiconductor quantum wells as active medium [25]. Parametric scattering [27], Bose–Einstein condensation [29], spin vortices [33, 123] and the most recent electrically pumped polariton laser [86] well embody the great potential of those systems. Meanwhile, investigation of organic based microcavities is extremely active and conveyed especially towards the observation of coherent lasing emission [48, 124]. The big variety and ease of processing of organic molecules and polymers allows for the realization of structures among the entire visible spectra [125, 126] but at the same time makes difficult the observation of any kind of nonlinear phenomena. The main reasons can be addressed to the scattering losses related to structural disorder and to the reduced polariton density of population achievable in organic microcavities (chapter 2). Various designs have been exploited to overcome such limitations: intracavity pumping mediated by host dyes to increase polariton luminescence, strongly coupled organic LED with high Q factor, Tamm plasmon and surface plasmon polaritons to enhanced light–matter coupling [47, 124, 127, 128] are examples of possible routes for improvement.
A completely different approach was for the first time theoretically introduced in the pioneering work of Agranovich *et. al.* in 1997 and subsequentialy expanded by many other research groups [49, 129–131]. The idea consists in the possibility to combine inorganic and organic semiconductors in a unique hybrid system which concentrates advantages of both materials such as high temperature operation and strong nonlinearities. Here, Wannier–Mott and Frenkel excitons are in resonance with each other and coupled through their dipole–dipole interaction at the interface of a multilayered stack or through cavity photons when embedded in a microcavity structure. The new formed eigenstates are described by a coherent linear combination of both excitonic

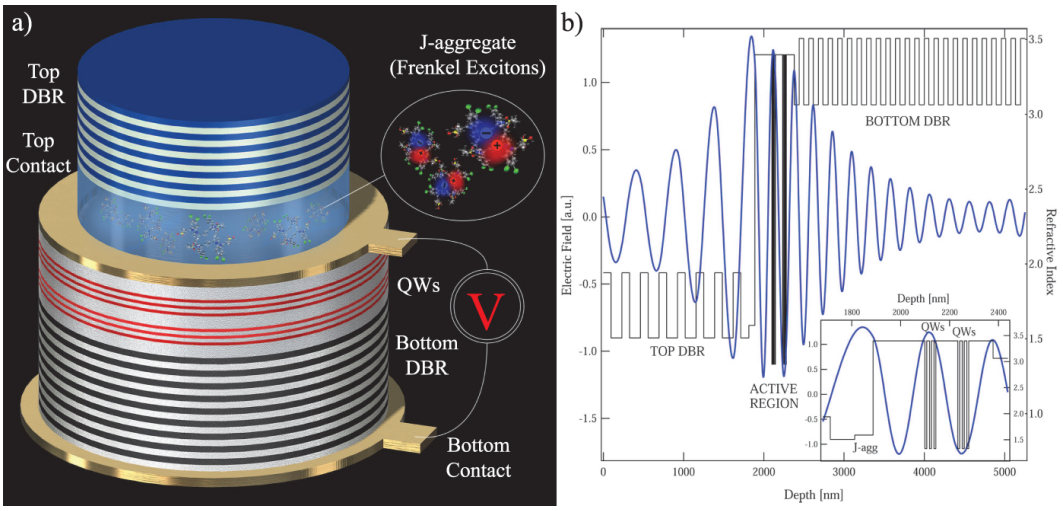

Figure 5.1: a) Schematic representation of the hybrid microcavity LED. b) Electric field profile across the entire microcavity structure as simulated by transfer matrix method. In the inset is shown an enlargement of the active region where field antinode on J–aggregate and QWs positions is enlighten.

species and therefore characterized by many desirable properties: small saturation density which enhances optical nonlinearities, large Bohr radius that favourites exciton–exciton (polariton–polariton) interaction and high oscillator strength for room temperature operation. This concept provides an elegant route to overcome basic limitations often imposed by the optoelectronic properties of pure inorganic and organic materials and provides efficient means to observe nonlinear cooperative phenomena which involve organic semiconductors.

The most straightforward and simpler design that could fulfill the theoretical predictions was suggested in the cited works and consists in a multilayered structure where a crystalline molecular semiconductor is deposited at the interface with inorganic quantum wells. Despite the relative simplicity of the idea, problems related to material purity and structural quality of the crystalline organic layer could arise during the fabrication process. Organic molecular beam deposition (OMBD) in fact, permits to control the deposited film on a scale of single monolayers (few nm) but at the same time purity and crystallinity, at the present state of the art, can be guaranteed only on certain type of surfaces and just by using specific molecules [132, 133].

The very different approach we have followed exploits the possibility to couple together spatially separated organic and inorganic excitations through the optical mode of a planar microcavity for the formation of exciton–polaritons characterized by a mixture of these three components. In addition, we exploit an efficient light–emitting–diode scheme based on the electrical injection of carriers into the inorganic part of the structure. Owing to strong light–matter coupling regime the electrical excitation is rapidly transferred via polariton to the organic counterpart, resulting in electroluminescence of the hybridized polariton states.

The chapter will begin with a full description of the structure design together with details of the fabrication process and results of the optical characterization. We will continue the discussion with the investigation of optical nonlinearities by means of a power dependence study of the polariton emission and conclude with experimental evidences of Frenkel/Wannier–Mott exciton strong coupling under electrical excitation.

5.2 Design

The main microcavity design is based on the principle that in case both inorganic quantum wells and organic layers are positioned at the antinode of the electromagnetic field profile across the cavity, hybridization with the optical mode occurs with resulting Frenkel/Wanier–Mott exciton–polaritons formation. To fulfill this requirement, theoretical simulations have been performed prior to the sample fabrication. The code implemented for the purpose is based on the transfer matrix method which allows to calculate the electric field function across a multilayer stack, based on the refractive index of each layer. In this way it can be possible to reproduce any planar microcavity structure under illumination of a light source at fixed energy and angle of incidence. This method also allows to extract the field antinode positions together with stop band and cavity mode energies to tailor accordingly the thickness of each compound for the final achievement of strong coupling.
The complete microcavity structure displayed in figure 5.1 **a** with related simulation in **b** consists in an active layer, composed by III–V semiconductor quantum wells and a molecular J–aggregate forming cyanine dye film, embedded in between two distributed Bragg reflectors (DBR) mirrors. The first half of the structure, fabricated by molecular beam epitaxy (MBE) growth on a GaAs substrate, is formed by 24 $\lambda/4$ pairs of $n-type$ doped AlAs/GaAs layers (bottom DBR), followed by six GaAs/AlGaAs quantum wells and ultimately by a $p-type$ AlGaAs layer which acts as spacer at the interface with the organic film. Here, both p and n type doped layers guarantee the efficient injection of carriers in the quantum wells from the metallic contacts. The top one deposited via gold evaporation while the bottom obtained by positioning the final device onto an electrically connected mount. Besides, etching was performed to ensure electrical isolation and avoid that the injected carriers would spread horizontally under the top contact. With this process we obtained different size mesas (diameter of 200, 350 and 500 μm) which forced and localized the electrical injection on a small active area. The fabrication of the second part of the microcavity consisted in the deposition of the organic J–aggregate film and subsequently of the top dielectric mirror. The cyanine J–aggregate dye chosen for the purpose is the U3 (3-[(2Z)-5-chloro-2-[((3E)-3-[5-chloro-3-(3-triethylammonium-sulfonatopropyl)-1, 3-benzothiazol-3-ium-2-yl]methylene-2,5,5-trimethylcyclohex- 1-en-1-yl) methylene] -1,3-benzothiazol-3(2H)-yl] propane-1- sulfonate) [134]. After being previously dissolved in a water based polyvinylalcohol matrix solution (33 mg/ml), the

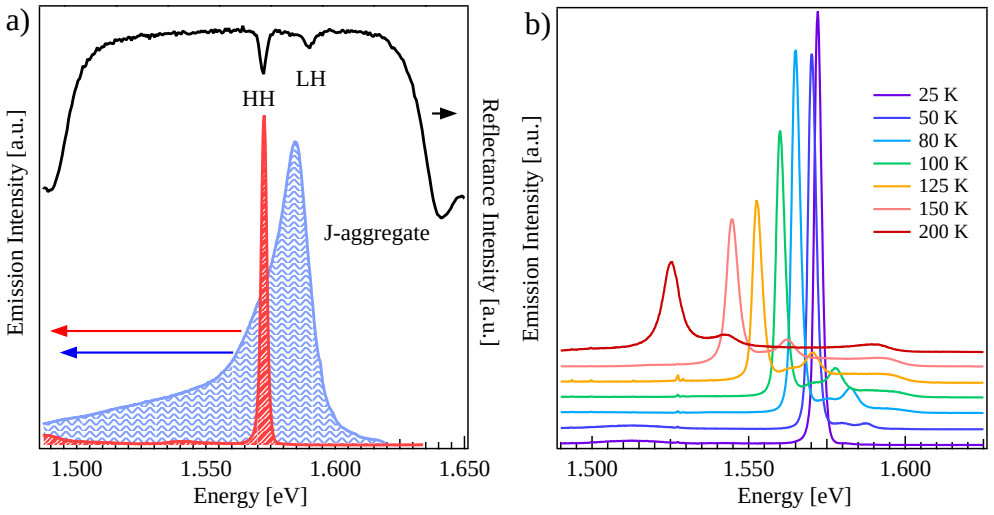

Figure 5.2: a) Measured bottom DBR reflectance together with quantum wells and J–aggregate PL emission. b) Quantum wells emission at various temperature conditions. At 25 Kelvin heavy hole excitons are located at 1.575 eV while light holes at 1.565 eV.

dye was spin casted onto the half inorganic cavity (AlGaAs spacer layer and gold ring contact) to obtain a homogeneous film with ≈90 nm thickness and match the transfer matrix simulation requirements. The choice of U3 J–aggregate guarantees nearly equal Frenkel and W–M exciton energies (figure 5.2 **a**) in such a way that resonance interaction through the electromagnetic field gives rise to polariton states with strong mixture of both species. The top DBR mirror which consists in 8 alternating pairs of tantalum pentoxide (Ta_2O_5) and silicon dioxide (SiO_2), was grown via sputtering deposition in a oxygen plasma atmosphere. High precision and fabrication quality of the process, together with high refractive index contrast of the two dielectric materials, permited to obtain a very broad stop band and a measured overall cavity quality factor of ≈1200. Extremely important for the investigation and interpretation of the final results was the optical characterization of every single component of the structure at each stage of the fabrication process. Therefore, knowing the specific role played by each element at specific conditions, permitted to obtain a clear picture of the general mechanisms which govern the complete system in the strong coupling regime. White light reflectance and photoluminescence spectroscopy were performed after the growth of the first half cavity to investigate quality and energy position of the bottom inorganic stop band and obtain as well detailed information about quantum well emission characteristics: heavy holes and light holes exciton separation, emission linewidth and its energy shift at different temperatures. For the same purpose and with a similar method, J–aggregate PL emission and dielectric top DBR mirror reflectance were investigated. The latter, for increased accuracy and precision, was grown and studied separately on different samples which will be described below. A summary of the bottom DBR reflectivity, quantum wells and J–aggregate emission is shown in figure 5.2.

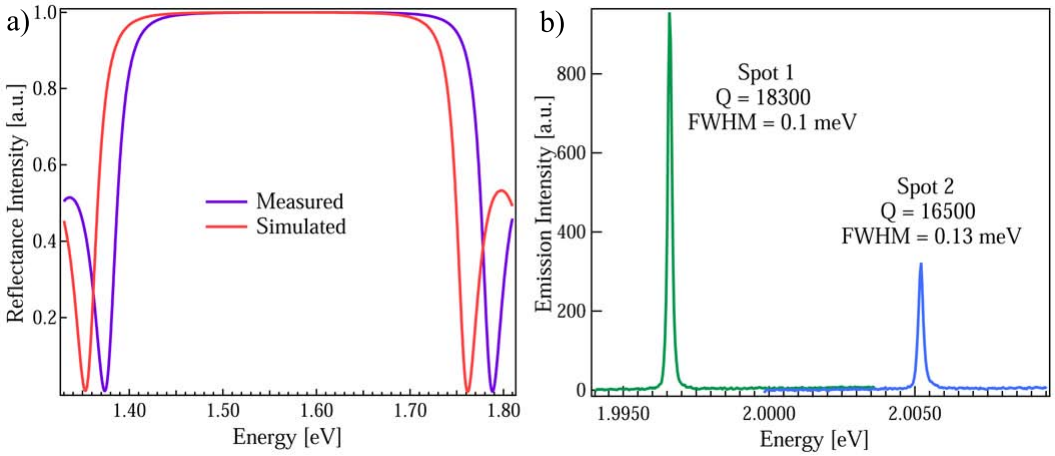

Figure 5.3: a) Measured and simulated top DBR reflectance designed for the full inorganic test microcavity. b) Transmittance measurements on the dielectric cavity which shows extremely narrow cavity mode.

5.2.1 High Q Dielectric Microcavities

During the fabrication of a microcavity structure which implies two different types of DBR mirrors (inorganic and dielectric) one has to take into account that the resulting stop band and the cavity mode energy come from a composition of the two reflectivity spectra in a way that is not easily predictable. As such, extremely high fabrication accuracy is mandatory to fulfill completely the simulation requirements and obtain correct detuning conditions.

Considering also the novelty of the approach we decided to realize different test mirrors to fully match our simulation code parameters (refractive index values and thickness) with measured reflectance spectra. Following the achievement of high fidelity and reproducible samples we also designed and fabricated a full dielectric cavity to test mirror quality and relate measured Q factor with number of DBR pairs. With an active region simply constituted by a SiO_2 spacer layer and bottom/top DBR mirrors respectively made by 15 and 11 pairs of alternating Ta_2O_5 and SiO_2 layers, we achieved a quality factor of ≈18000 (figure 5.3 **b**). The slight spectral difference between the simulated and measured reflectance curves of the top DBR shown in figure 5.3 **a** are simply due to a small variation in the refractive index parameters of the materials which compose the mirror, from the one accounted in the transfer matrix code. Considering an expected Q factor value of 20000, the obtained results emphasize the fidelity of the simulation code, the elevated mirror quality and the great potential of this technique to obtain high Q factor microcavities where both optical and electrical pumping schemes can be successfully implemented. In case of inorganic microcavity LEDs in fact, the common adopted design implies a top $p-type$ doped DBR based on III–V semiconductors which has been identified as structural limitation for the achievement of high Q due to cavity losses related to doping. Thanks to the new approach we have here introduced, this issue could be overcome and both high reflectivity and efficient electrical injection guaranteed.

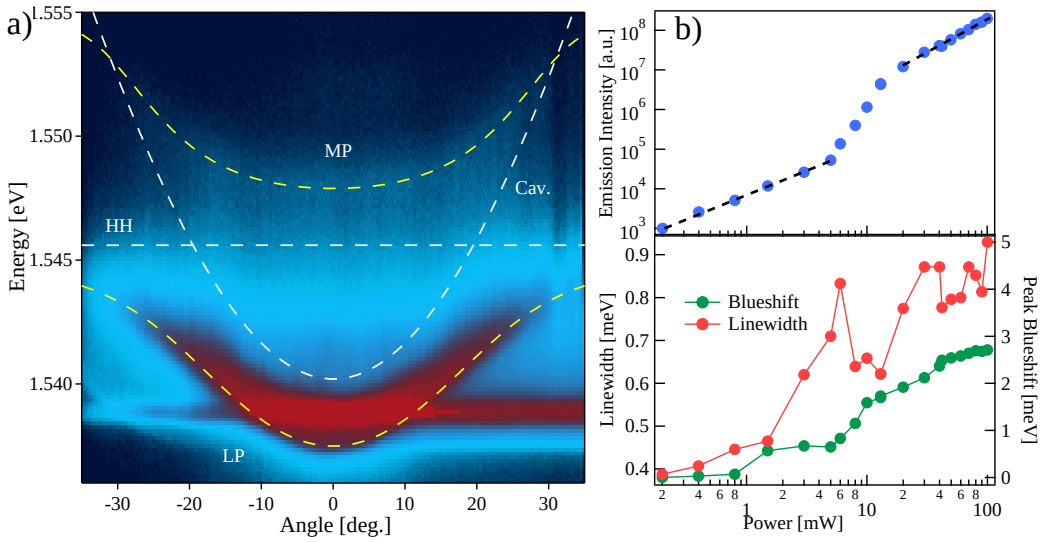

Figure 5.4: Sample 0: full inorganic microcavity in a LED design. a) Angle resolved PL image recorded above threshold (80 mW). Polariton lasing is clearly visible as very bright emission spot located near the bottom of the lower branch. b) Nonlinear emission intensity dependence as function of excitation beam power (threshold at 5 mW, 62 pJ) displayed on top of linewidth variation and peak blueshift.

As a proof, the effect of a top dielectric mirror on a full inorganic microcavity in a light emitting diode design was examined 5.4. The 11 pairs dielectric mirror was deposited on top of 12 GaAs/AlGaAs type quantum wells and 35 pairs of $n-type$ doped AlAs/GaAs bottom DBR (sample 0) to obtain a measured quality factor of about 8000 in spite of an expected value of 14000. This may suggest that problems related to the $p-type$ doped injection layer are still present and limit the overall quality. Nevertheless, clear polariton lasing emission was observed and proved by the power dependence study of the polariton photoluminescence intensity which shows a characteristic nonlinear increase at the threshold power. Line narrowing and peak blueshift, displayed in figure 5.4 **b**, accompany our interpretation. Additionally, theoretical fitting of the polariton branches and cavity position, based on the coupled oscillator model which accounts for the contribution of both heavy and light hole excitons, assures the persistence of strong coupling regime even above threshold and hence confirms the pure polariton lasing emission [135]. The presented analysis was pursued by mean of angle resolved photoluminescence spectroscopy which setup, described in Appendix A 7.2, was combined with an excitation pulsed beam of 1.65 eV and 80 MHz repetition rate. The full analysis of the experimental results will not be presented here since it goes beyond the main purpose of the dissertation. What is worth noting is the strong improvement attained by the use of a top dielectric mirror in a microcavity LED structure which allows for the implementation of an alternative electrical pumping scheme and the achievement of lasing emission due to the robust enhancement of the Q factor.

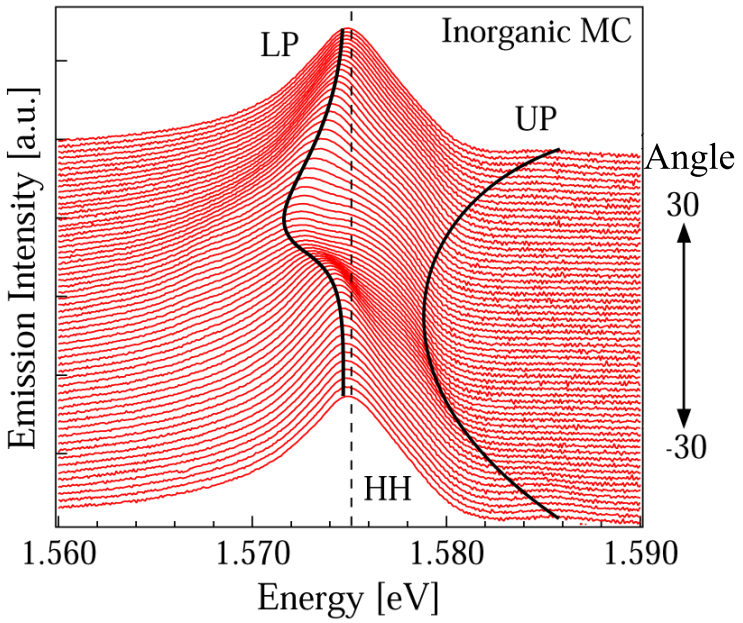

Figure 5.5: Photoluminescence profile spectra of the inorganic sample A, measured from -30^o to 30^o with increment of 1^o. Strong coupling between cavity photons at 0 detuning and heavy hole excitons (dotted line) is demonstrated by the appearance of lower and upper (much weaker PL) polarion branches, fit by the simulated curves (solid lines) extracted from the couple oscillator model.

5.3 Characterization

In this section we will follow the discussion on hybrid (QWs/J–aggregate) microcavity LEDs by presenting, analysing and interpreting the results obtained from the optical characterization. All the photoluminescence images that will be shown below were collected at a temperature of 20 Kelvin by means of angle resolved spectroscopy where a CW laser beam of 1.65 eV energy acted as pump source.

At first, a preliminary investigation was pursued on a microcavity sample (sample A), modified with respect to the design described in section 5.2 to incorporate only Wannier–Mott quantum well excitons: the J–aggregate dye was removed from the polymer matrix solution which was spin coated to preserve the correct cavity thickness. As distinctly appear from the PL profile spectra of figure 5.5, measured from -30^o to 30^o with increment of 1^o, strong coupling between heavy hole excitons (HH) at 1.575 eV and cavity photons (Δ=0 meV detuning) is manifested by the formation of lower and upper polariton branches. Theoretical fit based on the coupled harmonic oscillator model, as explained further, provided a Rabi splitting value of 5 meV, in accordance with typical values of III–V semiconductor based MCs [25] and measured quality factor of $\approx$ 1200.

The full structure (sample B) which includes both inorganic and organic excitons was then characterized and high oscillator strength Frenkel excitons, located at 1.586 eV, were found to strongly interact with the optical mode. The appearence of an additional branch, labeled as LP (lower polariton) in figure 5.6, separated from the J–aggregate

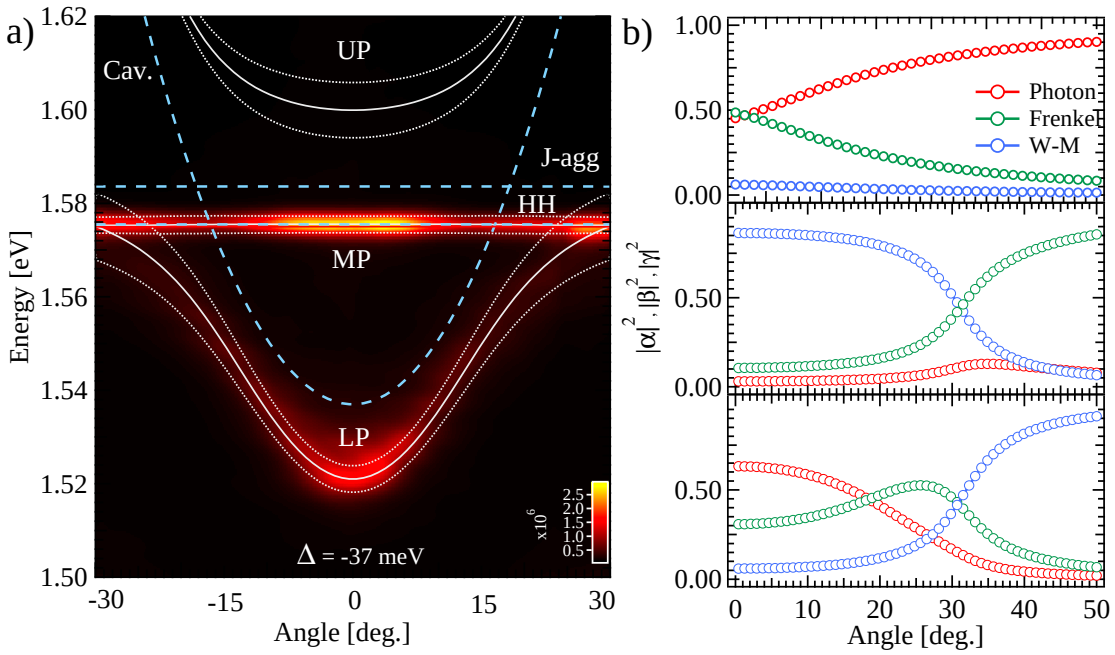

Figure 5.6: a) Photoluminescence imaging of the hybrid sample B at cavity detuning of -37 meV. Blue dotted lines refer to exciton and cavity positions while white lines to polariton dispersions with related FWHM, as calculated from the coupled oscillator model. Detuning is defined as difference between cavity position and heavy holes energy. b) Hopfield cofficients for upper, middle and lower polariton branches as extracted from the couple oscillator matrix.

energy and which exhibits typical anticrossing behaviour clearly suggests the presence of strong coupling regime. At the same time, the middle polariton (MP) branch is found to be very close to the HH exciton energy and still separated in virtue of the W–M exciton/photon coupling demonstrated in figure 5.5. Cavity detuning, for simplicity, is defined as difference between cavity position at $k_{||} = 0$ and heavy holes energy.
For a deeper understanding of the observed behaviour we couple cavity photon, Frenkel and Wannier–Mott excitons via the harmonic oscillator model and study the interaction Hamiltonian for the system:

$$\begin{bmatrix} E_c(\theta) - i\Gamma_c & V_f & V_w \\ V_f & E_f - i\Gamma_f & 0 \\ V_w & 0 & E_w - i\Gamma_w \end{bmatrix} \begin{bmatrix} \alpha \\ \beta \\ \gamma \end{bmatrix} = E(\theta) \begin{bmatrix} \alpha \\ \beta \\ \gamma \end{bmatrix}. \tag{5.1}$$

E_c, E_f and E_w define the energies of unperturbed optical mode, Frenkel (J-aggregate) and Wannier-Mott (QWs) excitons. Related profile linewidths (Γ_c=1.2meV, Γ_f=5meV, Γ_w=1.5meV) are introduced as damping terms while interaction potentials between cavity photons and each of the two excitons are represented by V_f and V_w. Besides, cavity mode dispersion E_c can be expressed, as previously introduced (chapter 2.4 and 4.3), by the following relation: $E_c(\theta) = E_0(1 - sin^2\theta/n)^{-1/2}$ (E_0 is the cutoff energy

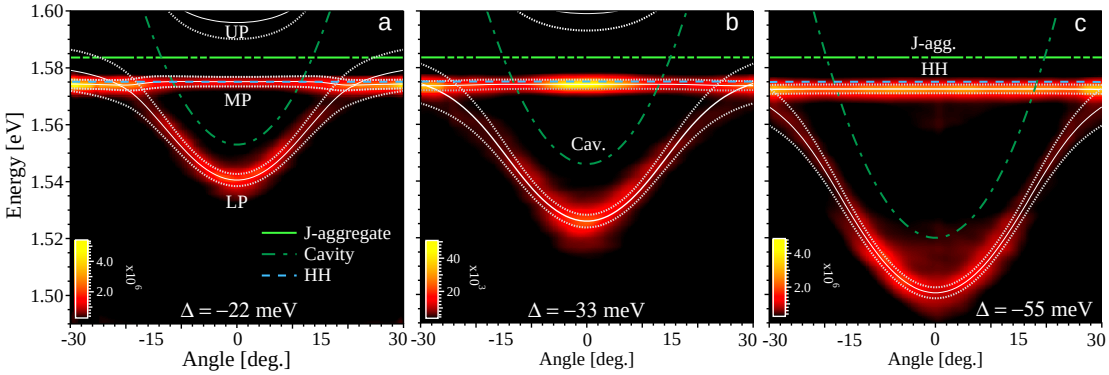

Figure 5.7: Photoluminescence imaging of the hybrid sample B at various cavity detuning (Δ= -22 meV, -33 meV and -55 meV). Exciton positions and polariton dispersions with related FWHM are also displayed as blue, green and white lines.

and n the refractive index). As also appear from equation 5.1 any kind of short range interaction (dipole–dipole) between the two different exciton layers is precluded by the presence of 200 nm thick AlGaAs spacer positioned within. Diagonalization of the coupled system in 5.1 yields to three different polariton modes with energy defined by $E(\theta)$ (eigenvalues of the matrix) and basis functions by α, β and γ. These are the Hopfield coefficients of the optical mode, Frenkel and W–M excitons and describe the weighting of each component in the final eigenstate. By discharging Frenkel exciton contributions, the model was used at first to fit polariton dispersions of the inorganic structure (sample A) and extract a Rabi splitting ($2V_w$) of 5 meV. This value was then input for the study of the full structure (sample B) where matrix (5.1) diagonalization led to a J–aggregate Rabi splitting ($2V_f$) of ≈60 meV, in accordance with values previously reported [134]. The excellent fidelity of our simulation is proved by the theoretical fitting of the experimental data with the three polariton dispersions extracted from the model (figure 5.6 **a** and 5.7).

Hybridization of Frenkel and Wannier–Mott excitons is utterly clear by calculation of $|\alpha|^2$, $|\beta|^2$ and $|\gamma|^2$, shown in panel **b** of figure 5.6 for each polariton branch. The specific cavity detuning is such that upper branch (UP) character is mostly determined by the photonic term in all the range of angle. In contrast, strong exciton mixing of the middle polariton (MP) is found to dominate over the small photon fraction with a maximum Frenkel/W–M hybridization observed at $\approx 30^o$ ($|\beta|^2 = |\gamma|^2$). The lower branch (LP) instead, possesses a substantial mixing of the three components which all play a significant role in the final polariton features. If Frenkel and photon components dominate the polariton character near $k_{||} = 0$, Wannier–Mott excitons contribution becomes remarkable only at large wavevectors. Nonetheless, as it will be extensively described in the next section, even a small percentage of Wannier–Mott fraction at $k_{||} = 0$ in the LP states is found to produce important consequences to the final nonlinear optical properties of the polariton particles.

An additional advantage of the presented system relates to the fact that spin casting

process allows for the study of manifold detuning conditions due to the noticeable variation of the organic layer thickness. As such, simple investigation of different locations across the sample serves as a straightforward approach for altering polariton features by the adjustment of Frenkel/W–M/photon fractions. As presented in figure 5.7, ≈ 30 meV cavity shift can be easily achieved with important effects on the polariton states population and features. For small negative detuning ($\Delta = E_c - E_w < 0$) in fact, we expect that direct scattering from the high density Frenkel exciton reservoir would favour the population of such polariton states which are close in energy. On the other side, as previously discussed in section 3.3, high negative detuning conditions would open ultrafast relaxation channels ($\approx$ 100 ps) driven by J–aggregate molecular phonons [1, 46]. This vibrationally assisted scattering mechanisms are expected to enhance the polariton population at the bottom of the lower branch states, in case of resonance conditions, and hence overcome the slow and inefficient decay ($\approx$1ns) observed in inorganic based microcavities [87,89]. Furthermore, variation of excitonic and photonic fraction for each cavity detuning would also have important consequences on the interbranch exciton–polariton scattering. In fact the interplay between polariton particles at different wavevectors on different branches characterized by a similar excitonic percentage, could modify the scattering processes and at last affect the relaxation efficiency. For instance, high W–M excitonic component found at small wavevector on the MP and at large $k_{||}$ on the lower dispersion (figure 5.8 **b**) could lead to efficient polariton scattering in this direction. Most remarkably, strong Frenkel exciton fraction found at large wavevectors on the MP and at the same time at $k_{||} = 0$ on the LP would open an effective path for direct polariton relaxation which strongly increases particles density towards the required lasing threshold (figure 5.8).

5.3.1 Negative Polariton Dispersion

In the particular hybrid system here investigated, the presence of two excitonic species (Frenkel and W–M excitations) with high contrasting oscillator strength and broadening of the exciton line, is at the origin of the strong polariton dispersion modification that we observed experimentally and report in figure 5.8 **a** and **b**. In case of a cavity detuning value of Δ=-22 meV in fact, the middle polariton dispersion frequency is found to decrease with increasing momenta, at a position located just above the point of equal Frenkel/W–M polariton composition $|\beta|^2 = |\gamma|^2$ ($\approx 20^o$). As occurs in the lower branch [41, 136], exciton–polaritons at the well define inflection point possess a negative mass $M = \hbar^2(\partial^2 E/\partial k^2)^{-1} < 0$, where k is the vector momenta and E the polariton energy. At this point, together with the negative mass, strong exciton–exciton repulsive interaction allows for macroscopic population which hence favourites the observation of nonlinear processes [27, 137, 138].
In our system, the negative mass possessed by such polaritons is dressed by the excitonic fraction of those particular states, in view of the fact that photons are massless particles.

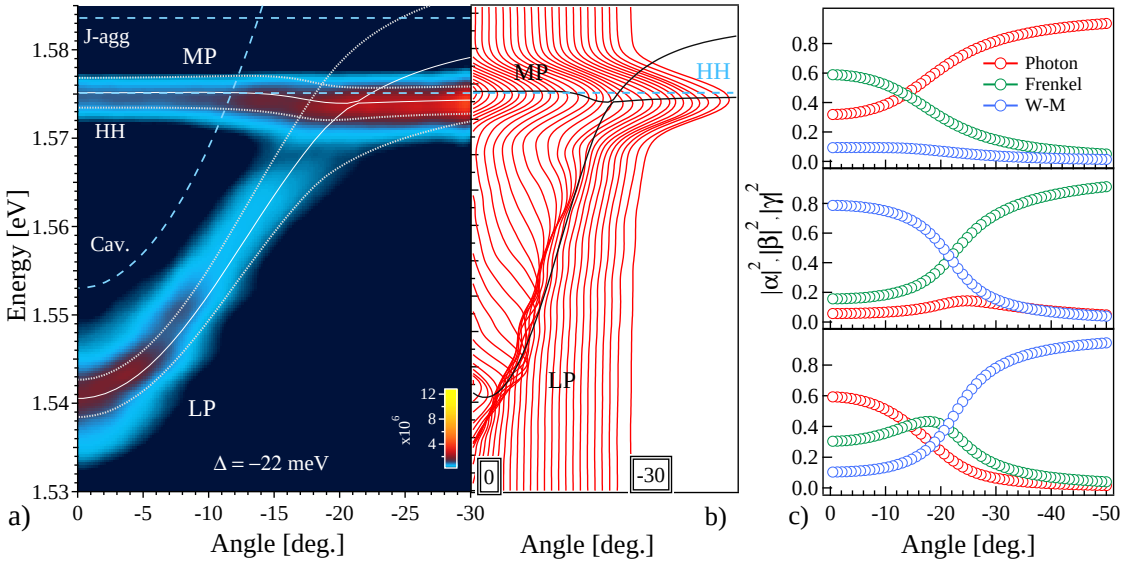

Figure 5.8: a, b) PL image and related integrated profile spectra of the hybrid sample B for small negative detuning (Δ=-22 meV). Theoretical fit of the polariton dispersion and relative broadening are displayed on top of (a) and (b) with white or black continuos and dotted lines. Negative distortion of the middle branch is observed in proximity of the anticrossing with the lower dispersion. c) Photonic and excitonic mixing coefficients calculated for the upper, middle and lower polariton branches.

As previously discussed (chapter 2), while Wannier–Mott type excitations imply a long range interaction and usually possess positive effective mass, $M_w = m_e + m_h > 0$ (m_e and m_h are the effective mass of electrons and holes), exciton radius in organic semiconductors is very small and for this reason the resonant intermolecular interaction strongly depends on the molecular orientation: resulting exciton effective mass can have different signs.

Considering an isotropic medium, the frequency ω depends on the wavevector $\mathbf{k}$ and as consequence the group velocity of the wave packet is defined as

$$\mathbf{v}_g = \frac{d\omega(\mathbf{k})}{d\mathbf{k}} = \frac{\mathbf{k}}{k}\frac{d\omega(k)}{dk}. \tag{5.2}$$

$\mathbf{v}_g$ will be negative and codirected with -$\mathbf{k}$ in case $d\omega(k)/dk < 0$. Following the discussion by considering a medium with small dissipation, in which energy propagation velocity coincides with the group velocity, the so called Poynting vector $\mathbf{S}$ (energy flux vector) is [139, 140]:

$$\mathbf{S} = U\mathbf{v}_g \tag{5.3}$$

where U is the time average energy density which in thermodinamic equilibrium is > 0. It follows that in the case of negative group velocity, the energy flux $\mathbf{S}$ is directed opposite to the wavevector $\mathbf{k}$ with occurance of negative refraction of light. Materials where negative group velocity can be observed are those characterized by large oscillator

strength and strong delocalization of the dielectric response function $\epsilon_{ij}(\omega, \mathbf{k})$ [141, 142]. The presented microcavity system, in addition to negative effective mass polaritons which can be also exploited at specific wavevectors $k_{||}$ on the LP [27, 41], provides additional advanges related to the decrease of the MP dispersion energy with increasing of the wavevector. In fact, at those frequencies, negative group velocity and negative refraction of light are expected. These effects will act in reversing the direction of propagation of the polaritonic wave with respect to the wavevector $k_{||}$ and ensure self–focusing and self–localization at the specific inflection position. Further beyond, reduced group velocity of the wave packet (the so called "slow light") is also responsible for the strong enhancement of third order optical nonlinearities [143–146] which eventually, combined with the mentioned effects, will permit to achieve the population density and conditions required for the occurrence of parametric scattering, solitons formation and other nonlinear phenomena.
As already presented in figure 5.8, the pronunced MP distortion can be modeled with the three elements coupled oscillator matrix discussed above (equation 5.1) only by implementing oscillator strength and dephasing time values characteristic of the specific QWs and J–aggregate excitons which form the microcavity structure we are investigating (sample B). Even if a complete and expanded theoretical dissertation on the observed behaviour will be presented in a separate work [147], it is worth underling that uniquely, contrasting oscillator strength and dephasing time values peculiar of the two different excitonic species allow for the appearance of a negative polariton dispersion in such a limpid and easily accessible way.

5.4 Hybrid Polariton Nonlinearities

In the previous section, introducing the presence of negative middle branch polariton dispersion, we enlighten one of the consequences of the Frenkel/W–M exciton mixing. Therefore we now proceed with the investigation of optical nonlinear properties of such hybrid polaritons with the study of photoluminescence polariton emission dependence on the excitation beam intensity. For the purpose, a femtosecond pulse laser at 1.6 eV and 100 kHz repetion rate was implemented and shone at an angle of 30^o with respect to the sample surface. The excitation energy was chosen in such a way to allow for the best direct pumping condition of the J–aggregate dye and to favour the intracavity pumping by means of the QWs emission. The collection system instead, is based on the angle resolved setup described in Appendix A 7.2. We start our analysis on the hybrid sample B and then compare the obtained results with a separate investigation of the isolated inorganic and organic based microcavities (sample A and sample C).

From an observation at the results displayed in figure 5.9, immediately clear is the presence of nonlinear emission from the lower polariton states at $k_{||} = 0$, where large population density concentrates at high excitation pump intensities. Following panel **a**

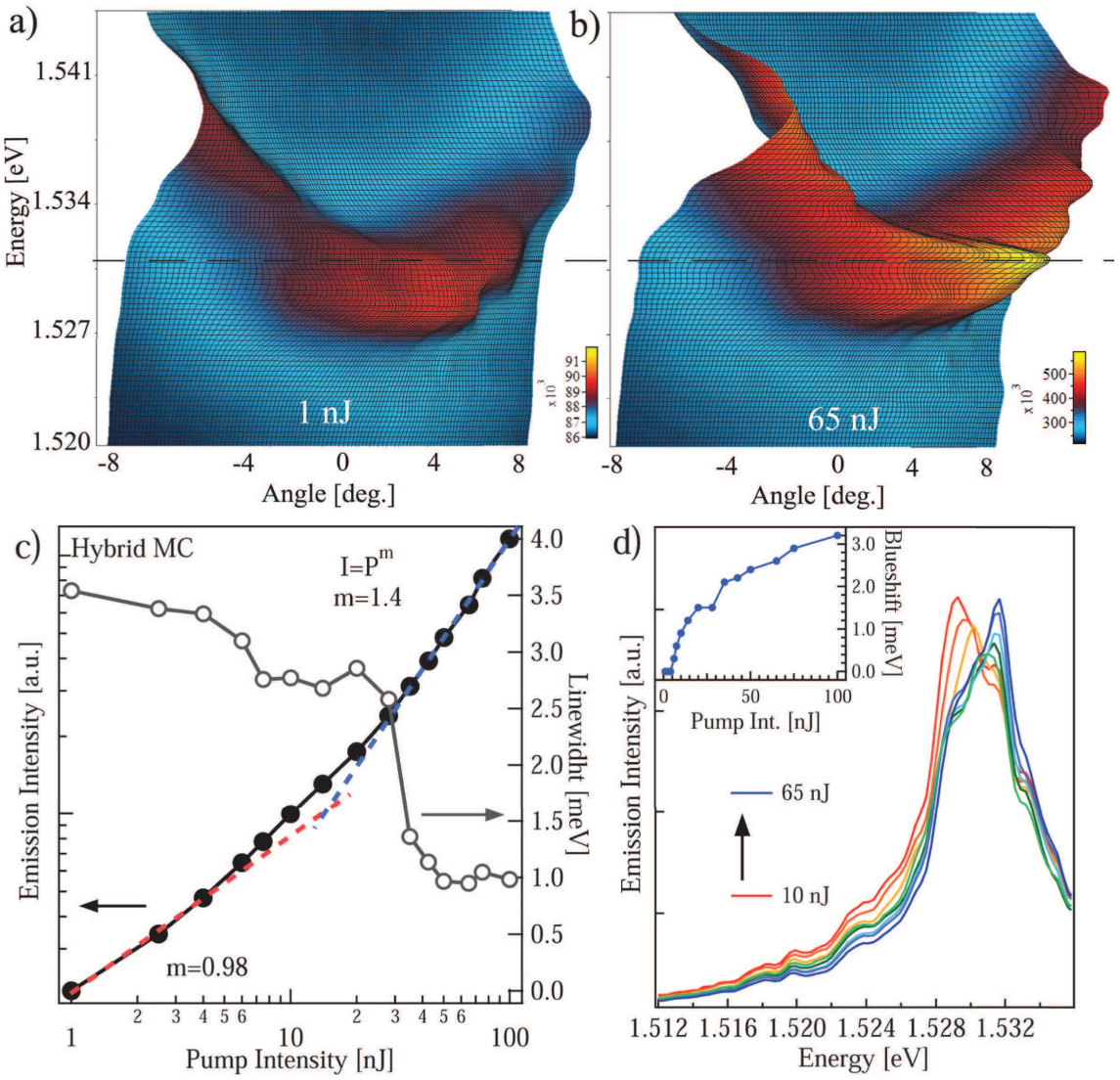

Figure 5.9: a, b) LP photoluminescence images of the hybrid system, at 1 nJ and 65 nJ pump energies. Related profile spectra at $k_{||} = 0$ and normalized to the relative applied power are shown in (d) where peak position is also displayed as inset. c) Emission intensity of the lower polariton branch ($k_{||} = 0$) with relative linewidth variation as function of excitation energy.

and **b**, which correspond to 1 nJ and 65 nJ pump energies, we distinguish a clear evolution of the exciton–polariton population, initially extended on a broad range of states and then gradually blueshifted and condensed with a nonlinear increase of its density. This results in the appearance of an intense and sharp peak located at the high energy side of the emission spectra as can been seen in the PL image of panel **b** and profile spectra of panel **d**.

By relating emission intensity I to applied power P with the following relation, $I = P^m$, we could extract m from the curve slope (panel **c**) and identify the transition from linear (m=0.98) to nonlinear regime (m=1.4) at the energy threshold of $\approx$ 28 nJ. Such increase is accompanied by a significant linewidth narrowing (2.5 meV), displayed in the right

axis of panel **c**. At the same time remarkable blueshift of the peak position ($\approx$ 3 meV), showed as inset in panel **d**, occurs. All these related effects are clear indications of superlinear polariton emission and suggest a possible coherence build–up in the system. Although Bose-Einstein condensation of exciton–polaritons has been observed in inorganic MCs [29], we conjecture that condensation of Frenkel excitons, only theoretically predicted [148, 149], is here prevented by bimolecular quenching. This constraining mechanism occurs frequently in a big variety of molecular compounds [150] and can become very effective in a microcavity system excited by a nonresonant optical pump. In fact, the main part of the excitation is concentrated in incoherent states (exciton reservoir) which possess high probability to undergo such annihilation process [101, 121, 151]. Despite this limitation, our experiment suggests that the unique mixture of properties of both materials, achieved by photon mediated hybridization, is responsible for the observed superlinear emission which has to be considered as a pre–lasing regime that anticipates macroscopic polariton condensation.

The importance of exciton mixing in the observed nonlinear polariton emission is demonstrated experimentally in the following discussion where LP photoluminescence of two different microcavity structures which separately incorporate J–aggregate and QW excitons, showed the absence of polariton nonlinearities. The PL emission is studied as function of pump intensity within identical excitation conditions used for the hybrid sample: samples temperature of 25 Kelvin and excitation at 30^o with a 100 kHz pulse beam at 1.6 eV. The inorganic MC previously introduced (sample A) was studied together with a full organic microcavity fabricated for the purpose (sample C). This was made by following the same design described in section 3.3 which consists in the deposition of the J–aggregate dye layer within bottom and top dielectric DBR mirrors. The investigation of mirror quality and related quality factor accomplished during the main fabrication process (section 5.2), permit us to realize a J–aggregate based MC with very similar Q compared to the hybrid and inorganic ones (sample B and sample A).
We start our discussion with the results shown in panel **a** of figure 5.10 which refers to the inorganic MC (sample A). Here, polariton photoluminescence increases linearly until the intense optical pumping causes saturation of PL emission before any nonlinear process can occur. What follows is a decrease of the emission intensity accompanied by a redshift of the peak position (inset graph). No remarkable variation of the PL bandwidth is reported.
Similar results were obtained for the full organic microcavity where strong coupling arises from cavity/J–aggregate exciton interaction (figure 5.10 **b**). Polariton emission scales linearly with the input power until high excitation densities bring the system to the weak coupling regime. Accordingly, slight PL maxima shifts and significant linewidth broadening occur. This behaviour resembles the power dependence measurements of the previously reported intracavity pumped MCs (chapter 4) and must be addressed to the photobleaching of the organic dye due to intense applied laser powers [152].
The comparison of these individually coupled Wannier–Mott and Frenkel excitons based

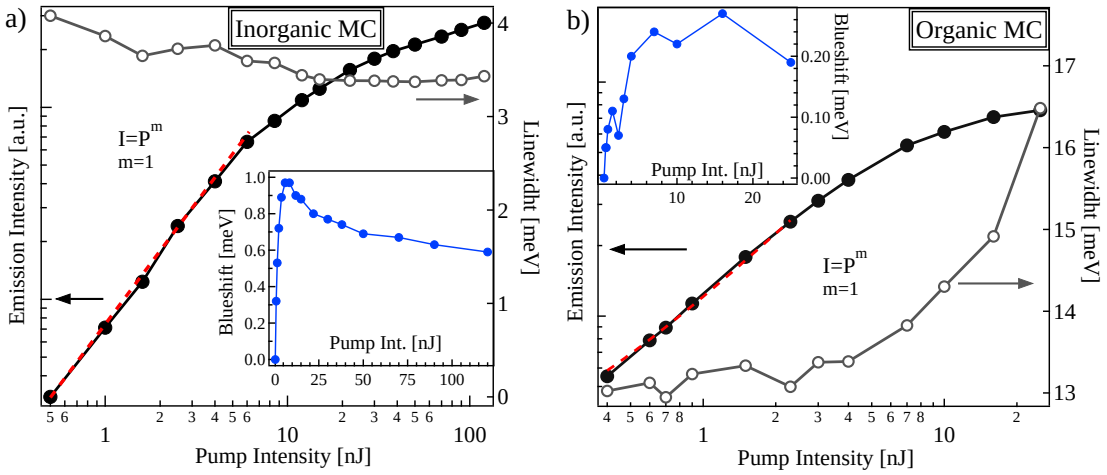

Figure 5.10: Emission intensity of lower polariton branch at $k_{||} = 0$ (black dotted lines), with relative linewidth (grey dotted lines) and peak (inset) variation as function of pump energy. a) Inorganic and b) organic microcavity sample.

MCs to the hybrid system, stresses the advantage of mixing organic and inorganic materials in the same microcavity to overcome the limitations imposed individually by each component. Theoretical demonstration of this effect was previously given by Zoubi *et. al.* [153] who described polariton states formed by substantial excitonic/photonic mixing, as characterized by combination of intrinsic nonlinear features typical of Frenkel and W–M excitons. Direct consequences of the hybridization process can be found in dynamics, properties and at last stage condensation of the final eigenstates.

A closer look to both organic and inorganic nonlinear contributions and to the role played in the studied system would help to understand the origin of the presented enlarged nonlinearities. As commonly found in literature, the traditional approach undertaken for a theoretical description of Frenkel excitons consists in a simplification of their paulion treatise by replacing Pauli operators with Bose type operators [154]. Together with this process one must include in the picture an additional term which compensate the difference between these two statistics. This term describes a short range nonlinear interaction between bosons (kinetic exciton-exciton scattering) which in case of polaritons, treated via effective potential approximation [153], could be represented as product of Frenkel Rabi splitting energy and organic molecular size: $2V_f a_0^2$. On the other side, nonlinear properties of inorganic semiconductors arise from the consideration of the fermionic nature of electrons and holes which compose Wannier–Mott excitons. Following the approach described by Ciuti *et. al.* [155], exciton exachange interactions results in a repulsive polariton–polariton interaction when coupling with photons is included in the theoretical description. In the same way as in the Frenkel polariton case, effective potential approximation will lead to the description of W–M polariton interaction via the following term: $2V_w\lambda_w^2$, where $2V_m$ represent Wannier-Mott Rabi splitting and λ_w exciton Bohr radius.

Considering now both J–aggregate/QWs Rabi splitting values previously extracted from

the system in 5.1 (60 meV and 5 meV) with related molecular size ($a_0 \approx 1$ nm) and electron/hole radius ($\lambda_w \approx 10$ nm), we find that Wannier–Mott interaction potential is approximately 1 order of magnitude bigger than the Frenkel one: $2V_w\lambda_w^2 \approx 8(2V_f)a_0^2$. Since these two components differ in nature and especially in magnitude, it directly follows that Frenkel/W–M exciton weigths in each polariton branch play a crucial role in the final hybrid polariton–polariton interaction strength. In fact, in the case of an external field oscillating with frequency ω close to resonance with the polariton branch s, at fixed in–plane wavevector $\mathbf{k}$, we can define the third order polarization function ($\chi^{(3)}$) as [153]:

$$\chi_{\mathbf{k}}^{s(3)} = \frac{-Q_{\mathbf{k}}^{s}|g_{\mathbf{k}s}|^4}{(V_{\mathbf{k}s} - \omega - i\Gamma_{\mathbf{k}s})^3(V_{\mathbf{k}s} - \omega + i\Gamma_{\mathbf{k}s})} \tag{5.4}$$

with

$$Q_{\mathbf{k}}^{s} \propto (2V_w\lambda_w^2\,|\gamma_{\mathbf{k}}^{s}|^4 + 2V_f\lambda_f^2\,|\beta_{\mathbf{k}}^{s}|^4). \tag{5.5}$$

$\Gamma_{\mathbf{k}s}$ represent the previously introduced damping rates while $|g_{\mathbf{k}s}|^4 \propto |\alpha_{\mathbf{k}}^{s}|^4$. Considering that $|\alpha|^2$, $|\beta|^2$ and $|\gamma|^2$ define the photonic, Frenkel and Wannier–Mott excitonic weights, their strong effect on the polariton nonlinear response $\chi^{(3)}$ is utterly clear.
By simulation of the dispersion image which observed nonlinearities of figure 5.9 refers to, excitons and photon percentages in each polariton branch at each defined angle are extracted. Particularly to the lower polariton states at zero wavevectors ($k_{||} = 0$) we find an effective mixing of all the three components: $|\alpha|^2$= 0.58 $|\beta|^2$= 0.32 and $|\gamma|^2$= 0.1. Considering that the relatively small value of the W–M excitonic fraction can yet provide efficient means for intensification of the nonlinear response, as here reported, due to the high magnitude interaction potential supplied, we conjecture that further design improvements which would increase such percentage could be undertaken for an even larger enhancement of hybrid polariton nonlinearities.

5.5 Electroluminescence

To evaluate the full potential of the microcavity system here presented in the figure of merit of a polariton device one has also to consider the possibility to achieve photon mediated exciton mixing via electrical injection. Simultaneous coupling of organic and inorganic excitons with the optical mode is here attained with resulting formation of polariton particles with very similar features compared to the previously reported photoluminescence measurements. Additionally, increase of the polariton population density is expected due to the particular structural design.

As already mentioned in the previous section 5.2 where a detailed illustration of the device structure was made, a light emitting diode scheme was implemented in the hybrid microcavity device in such a way that high electrical conductivity typical of inorganic semiconductors and strong optical response (oscillator strength) of organic excitons are

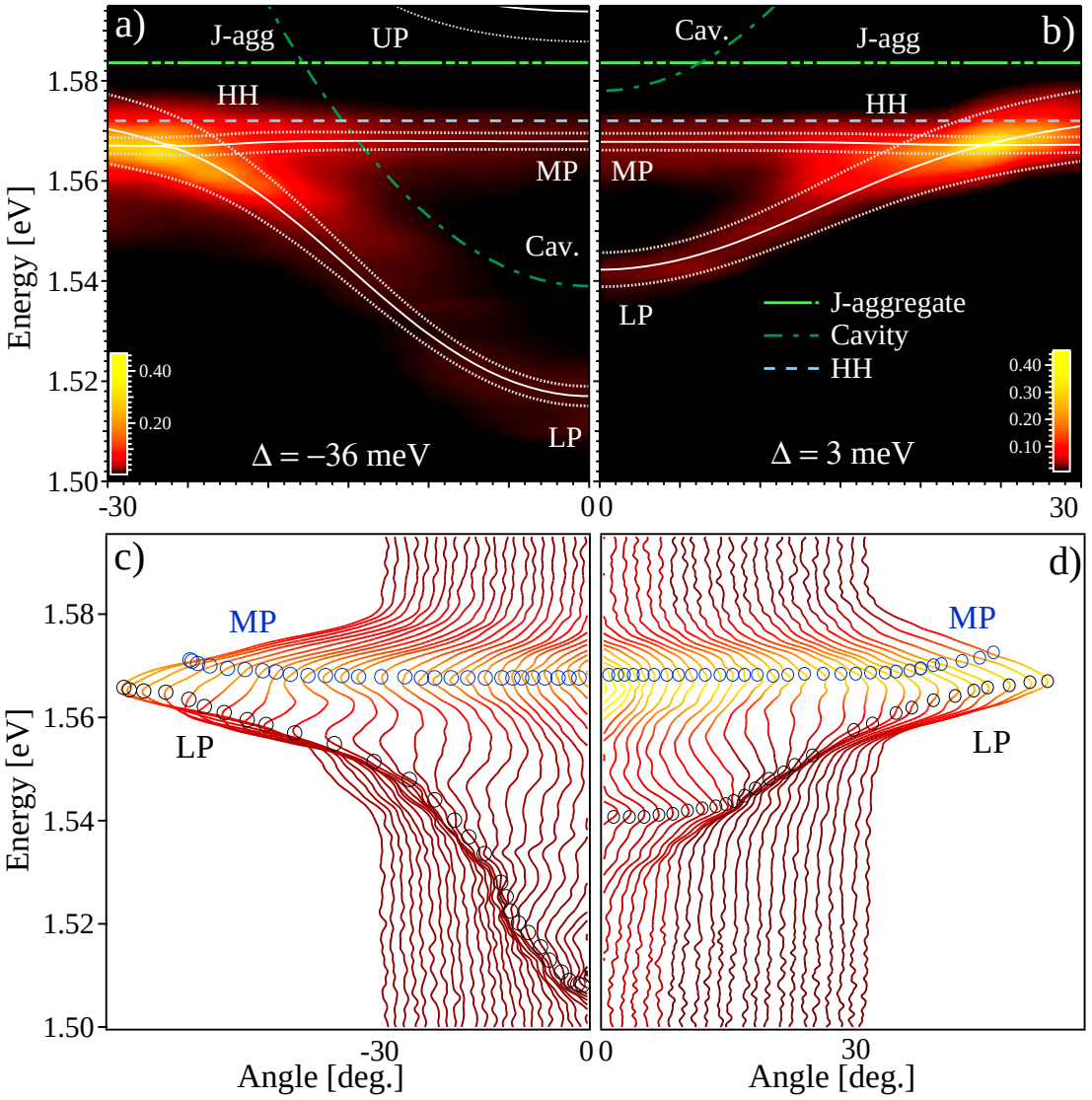

Figure 5.11: Electroluminescence images and related profile spectra of the hybrid MC LED at two different detuning values Δ: (a), (c) -36 meV and (b), (d) 3 meV. Polariton dispersion curves with related broadening, as calculated from the coupled harmonic oscillator, are also displayed in (a) and (b) as continuous and dotted white lines. Excitons and cavity positions are shown with blue and green lines. In a similar way, middle and lower polariton branch position at each angle are indicated with blue and black circles on the profile spectra in (c) and (d).

simultaneously exploited. As such, efficient intracavity injection of carriers in the inorganic QWs through the n^+ and p^+ doped DBR and AlGaAs spacer layer allows for the created excitation to be shared among the three polariton branches as resulting from the exciton–photon coupling regime.

Angle resolved electroluminescence images with extracted profile spectra, displayed in

figure 5.11, present middle and lower polariton branches for two different detuning conditions (Δ=-36 meV, 3 meV) and hence demonstrate the presence of strong coupling regime. Couple oscillator model was used to fit polariton dispersions and bandwidth based on dephasing time and Rabi splitting values previously calculated ($2V_f$=60 meV and $2V_w$=5 meV). Reproducibilty of the experimental data with high level of precision demonstrates that electrical excitation maintains the light–matter interaction strength and suggests that hybrid polariton nonlinear properties previously reported are still preserved. Furthermore visible broadening of middle polariton branch can be interpreted by considering that QWs EL emission is delocalized over a large area ($9,610^4 \mu m^2$) with respect to the spot excited by the laser pump ($\approx 12 \mu m^2$): presence of defects, energy shift and strong luminescence from uncoupled QW excitons emitting from the outer part of the mesa all contribute to dim the emission of pure polaritonic states. For this reason spatial filtering was implemented in the angle resolved collection setup by using an optical diaphragm. Additionally, we could explain the strong polariton emission observed at large wavevectors as due to the high exciton population injected in the QWs which populates highly excitonic MP and LP states located in proximity of the W–M energy. The important advantage of exploiting an intracavity pumping scheme is directly refered to the intrisic disorder and inhomogenety which characterize the J–aggregate compound. In fact, when optically pumped the formation of highly populated and uncoupled Frenkel exciton reservoir states can cause important losses and hence reduce the overall polariton population. Instead, by direct intracavity excitation, formation of such reservoir is prevented since the entire excitonic population is transferred to polariton states. Suppression of nonradiative decay and recombination of uncoupled excitons could therefore guarantee large polariton densities [156, 157].

From an applied current of 0.711 mA which correspond to the measured diode turn on voltage of 2.5 V at 20 Kelvin, we can calculate the polariton population n, considering an average carriers lifetime of 500 ps [158], via the following relation: $n = J\tau/e$. Here e is the electron charge and J the current density. A polariton density of $n = 2.3X10^9 cm^{-2}$ is found. Despite the obtained value can appear small, the very weak turn on voltage reported has to be considered. In fact 2.5 V appears very low in comparison to previously reported organic and inorganic polariton LEDs [47, 159, 160] and therefore provides the important indication that higher current values could be effectively achieved. In fact, a saturation current value of $\approx$10 mA, measured for a weakly coupled test sample, would increase the population density up to $3.2X10^{11} cm^{-2}$ and hence approach the threshold values required for lasing. Direct electroluminescence measurements at high current intensities were not performed to prevent damages of the organic layer due to heat dissipation and hence compromise the device working function. Therefore, precautionary test experiments will be required to evaluate with good accuracy the effect of high applied voltages on the specific organic J–aggregate layer.

In conclusion we have demonstrated that hybridization of inorganic and organic excitons with the optical mode of a planar microcavity allows for the formation of polariton particles which possess enhanced nonlinearities (sample B) with respect to the bare compounds, QWs and J–aggregate, separately strongly coupled (sample A and C). Such improvement is expected to occur even in the case of already pronounced intrinsic polariton nonlinearities, common for inorganic based microcavities. Although, superlinear emission suggests that further engineering improvements must be followed for the achievement of polariton condensation. On the other hand, presence of a MP negative dispersion guarantees polariton self–localization and provides the possibility for a deep investigation of solitonic features, parametric amplification and other cooperative phenomena.

Furthermore, the implementation of an electrical injection scheme which preserves strong coupling strength, polariton nonlinearities and exploits direct intracavity polariton pumping represents a step forward the realization of effective polariton based devices (polariton laser, transistors and switches).

6 Conclusions

Since the first demonstration of strong light–matter coupling [25], organic and inorganic semiconductor microcavities have been undergone a fast and remarkable improvement following the advancements of the fabrication techniques which ameliorate the structural quality. As results, a manifold of fascinating phenomena have been observed and exploited within practical devices [27, 29, 43].
In such interesting and rich scenario, the present thesis aimed at providing altenative approaches which can overcome design and compounds limitations still affecting both classes of microcavities. Although the main discussion was focused on the issues related to organic materials and organic polaritons, a design scheme for extremely high quality inorganic microcavities was also proposed. Besides, inorganic semiconductors were implemented within a hybrid structure for the formation of mixed Frenkel/Wannier–Mott exciton–polaritons.

To enlighten the present state of the art of polariton microcavities, a review on light and matter coupling was at first presented in chapter 2 with particular attention on materials and excitonic properties of organic and inorganic compounds. Starting with a description of molecular and crystallographic structure of both semiconductor species, Frenkel and Wannier–Mott excitons were discussed and their behaviour in response to an optical stimulus analysed. Under these basis it was then possible to picture a general scenario of the main characteristic, advantages and limitations which define inorganic and organic microcavities.
One of the main purposes of the improvement of organic based microcavities which this work followed, was direct towards the observation of nonlinear phenomena which involve Frenkel exciton–polaritons. Condensation of polaritons and observation of lasing emission in a J–aggregate microcavity for example, could be even commercially exploited with the fabrication of a polariton laser device, based on the well developed organic light–emitting–diode scheme which enables electrical excitation and strong coupling even at room temperature.

In chapter 3 the problem was initially approached with a detailed study of optical nonlinearities proper of a J–aggregate cyanine dye (TDBC) which represents the most used and promising class of organic materials for realization of polariton devices. Despite such organic compounds possess relatively high third order nonlinearities (nonlinear refractive index and nonlinear absorption) with respect to other organic materials, it was found that the optical response of the system follows the behavior of *reverse saturable absorbers* (RSA): the optical excitation is strongly absorbed by already excited states which possess larger absorption cross section compared to that of the ground state. It follows that higher energy levels are strongly populated with possible lost of the main percentage of the excitation via nonradiative decay processes. This behavior was confirmed by theoretical simulations here implemented to validate our experimental findings. Additionally, the model was used to qualitatively describe the time evolution of the population density in each energy level. As displayed in figure 3.5 for the three excitation energies used in the experimental analysis, the highest energy excited state, labeled in the text as S_2, always carries the strongest amount of population in comparison with ground and first energy levels hence confirming the RSA behaviour. Furthermore, such analysis unveiled that population redistribution throughout the energy levels is modified accordingly to the laser pump frequency and specifically that the alternation of population density between S_1 and S_0 well describes the oscillations of the nonlinear refractive index sign experimentally observed.
Besides, long–range molecular disorder characteristic of organic J–aggregates is well known to be responsible of Frenkel exciton localization. As a consequence such disorder directly affects the exciton coupling with the electromagnetic radiation of a planar cavity by reducing the polariton population in favour of the uncoupled reservoir states. In this contest the effective exciton coherence length plays an important role over the molecular aggregate. From our analysis on a TDBC J–aggregate thin film, wavefunction delocalization was extracted and the average value of 10 molecules used as input for a new theoretical treatise of the light–matter coupling process. From such experimental indication a direct connection to the molecular disorder parameter was established to revaluate the oscillator strength distribution over the aggregate chain. Indeed it was found that from the commonly assumed value of 0.1 degree of disorder, which corrisponds to an average delocalization length (IPN) of 70 molecules, the statistic has to be changed to a value of 0.8 which reflects the measured IPN value of 10 molecules (figure 3.8). Under this new scenario the oscillator strength was found to be redistributed over higher energy collective states with strong influence on the amount of "bright" states and eventually to the exciton–polariton population density. At the same time strong on–site eigenstate localization was accomplished and the following increase of exciton–exciton mutual interaction understood as the principal origin of the experimentally observed optical nonlinearities.
The particular TDBC J–aggregate dye was then implemented as active layer in a planar cavity where exciton–polariton properties were investigated via optical characterization.

Various intensity peaks at specific energy positions along the lower polariton dispersion were observed in the photoluminescence spectra. A close look on the Raman spectra of the bare film disclosed the experimental observation by evidencing the presence of strong vibrational modes characterized by the same energy which separates the emission intensity peaks from the exciton reservoir energy. Experimental proof of vibrationally assisted polariton scattering was hence obtained. This process was then reproduced by means of a theoretical simulation which also provided important informations about the temporal dynamics of such mechanism. Following these predictions, design and implementation of a pump–probe setup permitted to observe remarkable differences in the rise time of the decay signals related to LP energy states off and on resonance with the vibrational modes. Specifically it was found that in the latter case, signal build–up (rise) times which represent the polariton scattering from bright exciton states, are shorter with respect of scattering times to off resonance energy states.
The results of such analysis enlightened the presence of a vibrationally assisted polariton scattering mechanism which opens a fast and efficient relaxation path from uncoupled states in the exciton reservoir directly to specific positions on the polariton dispersion. This observation also suggests the possibility to exploit such relaxation process to effectively achieve macroscopic polariton population on well defined and localized lower polariton energy states. In fact, by precise cavity tuning it would be possible to position the highly populated resonance states at the bottom of the lower branch and thus benefit for the achievement of the density threshold required for coherent lasing emission. By combining this fine approach with an improvement of the cavity Q factor, being possible by increasing the DBR mirror reflectance, polariton particles lifetime would also increase and hence favour the thermalization process.
Furthermore cavity detuning could be set in such a way to address negative mass polariton states on the lower branch by vibrationally assisted relaxation mechanisms. Resonant optical pumping of those high density LP states would provide an additional means for the enhancement of polariton–polariton scattering interaction aimed at the observation of parametric amplification which is not restricted by momentum conservation due to the localized nature of the final states [161]. Implementation of the pump–probe setup previously described (Appendix A 7.4) would perfectly suit for the purpose: the transmitted probe beam, at different delays and resonant to the final state energy would be investigated following the intense pumping of the phonon–resonant LP states.

Nevertheless, optical limitation due to reverse saturation of absorption, large amount of uncoupled excitons together with design issues which introduces difficulties in the efficient exciton pumping were problematics not yet solved. For this reason, two different microcavity structures, designed and fabricated to individually address the problems, were presented and their properties were described in chapter 4. In both systems the original structure which consists in a J–aggregate layer positioned in between two distributed Bragg reflectors, was modified with the inclusion in the active region of a bright host polymer or a second J–aggregate dye with different exciton energy.

In the first case the polymer dye, optically inactive, acted as spacer and emitting layer, providing a means for effective radiative intracavity pumping due to the spectral overlap of dye emission with the polariton states. Besides, efficient excitation of the host/pumping polymer was assured by the broad absorption spectra located far outside the high reflectance stop band region. The optical characterization resumed in figure 4.2 enlighten the achievement of large occupation densities at the bottom of the polariton dispersion. The relatively low quantum yield of the host dye was assumed as possible cause that prevented observation of polariton condensation. However, the possibility of bypassing the exciton reservoir via direct population of polariton states was proved to strongly favour the thermalization process towards the achievement of the lasing density threshold. Noticeable improvements could be attained by substitution of the host pumping dye with high quantum yield compounds together with a redesign of the microcavity active region aimed at the reduction of the cavity size. In this direction layer–by–layer deposition of the J–aggregate dye would guarantee ultra–thin films which could yet sustain strong photon coupling and thus accomplish the purpose.
The second microcavity structure, fabricated and discussed in chapter 4, consists in a planar cavity with active region defined by two different J–aggregate excitons mixed together to form a single uniform layer. Both excitons are optically active and contribute to the strong coupling process with the formation of hybrid organic polaritons. The system was described with a coupled harmonic oscillator model whose solutions were then used to fit experimetal photoluminescence emission spectra (figure 4.6). The new energy configuration which consists of three polariton branches, was demonstrated to favour polariton relaxation from high energy states into the bottom of the lower branch. Novel pathways which involve efficient multiple scattering between polariton branches and the exciton reservoirs were identified. The middle branch especially, was found to act as important transition channel which strongly depopulates high energy states due to the vicinity to both reservoirs and to its strong excitonic hybridization that facilitates scattering processes. Such dynamics were revealed by combined photoluminescence excitation and reflectance spectroscopy together with time decay measurements of polariton states at different angular positions. Furthermore, time resolving PL emission of bare excitons in separate films and combined in a blend, unveiled the absence of direct molecular energy transfer. Despite of this, the observed relaxation dynamics could be reconsidered in the view of the fact that such mechanisms allow for long range energy transfer mediated by strongly coupled exciton–polariton states. The direct implementation of such approach for light–harvesting purposes has not yet been investigated but its potential impact in both natural and synthetic systems is utterly clear. The first step along this path could be attained by investigating microcavity structures formed by J–aggregate dyes with various exciton energies. A direct relation of the relaxation efficiency with respect to the exciton energy separation would draw the limiting boundaries of such long–distant energy transfer and dictate further developments and applications.

An alternative approach was then followed in chapter 5 where a novel microcavity structure was realized. The main idea which inspired the system is based on the concept proposed by Agranovich and coworkers [49] in 1997 who demostrated that strong coupling of Frenkel and Wannier–Mott excitons via the electromagnetic mode of an optical cavity could lead to the formation of hybrid polariton particles which unify favourable properties of both semiconductor species in a unique system. On the other hand, positive achievements enlighten in chapter 4 suggested the correct path to undertake to develop the most efficient and practical structural design.
Inorganic quantum wells and a J–aggregate dye were enclosed in between two distributed Bragg reflectors to form the active region of the cavity; furthermore, a light–emitting–diode scheme was implemented to permit electrical excitation of the system. Exciton energies were chosen in such a way to guarantee the effective mixing of inorganic and organic exciton species and to favor population of polariton states via intracavity pumping. At the same time accurate modeling and tuning of the layers thickness assured hybridization of Frenkel and Wannier–Mott excitons through the photonic mode for the formation of hybrid polaritons. It is worth mentioning that the fabrication of such complex device required combination of state of the art of inorganic and organic semiconductor processing techniques. Particular attention was focused on the top dielectric DBR mirror which required preliminary deposition tests to ensure reflectance quality and correspondence of stop band position to the simulated spectra. An empty dielectric cavity with extremely high quality factor, simulated (20000) and measured (≈18000) was fabricated for the purpose. Furthermore, the implementation of the dielectric mirror as top DBR of an inorganic microcavity LED device allowed for the observation of polariton lasing emission under optical pumping. Besides the good quality and fidelity of the model, these results provided further indications on the importance of the novel approach. In inorganic MC LEDs in fact, achievement of high quality factor is limited by doped inorganic DBRs losses. Implementing a top dielectric mirror on the injection layer guarantees at the same time good electrical contact and extremely high reflectance, which could possibly lead to lasing emission also under electrical excitation.
Characterization and discussion of the organic–inorganic hybrid microcavity was presented in section 5.3. Strong coupling was observed in the photoluminescence spectra and for a complete understanding, experimental data were modeled with a coupled harmonic oscillator. The simulated curves nicely reproduce energy and linewidth of the three polariton dispersions hence confirming the simultaneous coupling of both excitons with the optical cavity mode. This theoretical analysis has been possible only after optical characterization of a secondary sample, devoided of J–aggregate excitons. Here, PL profiles at different angles enlighten strong quantum wells exciton–photon coupling with a Rabi splitting of 5 meV. The value was then implemented in the coupled oscillator model of the full system which provided a J–aggregate Rabi splitting of about 60 meV, in full accordance with typical organic microcavity structures [134].

Enhanced polariton nonlinearities which are predicted to arise from Frenkel/Wannier–Mott exciton mixing, were studied by means of photoluminescence dependence on the optical excitation power, as displayed in figure 5.9. Despite of the fact that a clear intensity threshold was not observed, superlinear emission accompanied by remarkable PL spectra narrowing and peak blueshift were understood as important signs of a pre–lasing regime that anticipates macroscopic polariton condensation. Most remarkable, identical spectroscopic analysis repeated on two separately strongly coupled organic and inorganic microcavities did not show any kind of nonlinearity. Sublinear dependence of emission intensity, PL broadening and appearence of weak coupling regime undoubtedly confirm the improvements achieved by Frenkel/W–M exciton hybridization. This conclusive statement acquires even more importance by considering that the hybrid system proposed in this work represents a rich playground for the observation of interesting and unusual phenomena. Clear experimental evidence of negative polariton dispersion was in fact attained under particular cavity detuning conditions due uniquely to the photon mediated hybridization of excitonic species (Frenkel and Wannier–Mott) characterized by contrasting oscillator strength and broadening of the exciton line. The importance of the observation, fully discussed in section 5.3.1, resides in the fact that in addition to the particle negative mass possessed at the inflection point, the presence of negative group velocity implies a negative refraction of light which acts in reversing the polariton direction of motion and causing self–localization. Therefore, this system can favour the investigation of various cooperative phenomena because of high population density, strong polariton–polariton repulsive interaction and enhanced nonlinear optical effects located at a well defined position on the middle polariton branch [138, 145]. Furthermore, the accessibility of these states compared to the experimental difficulties presented by the fine searching of the so called "magic angle" [27] could represent an important advantage for the realization of double beam experiments aimed at the study of parametric amplification. Besides, the contrasting features of Frenkel and W–M excitons would eventually introduce interesting modifications in the physics of the mentioned phenomena, as only theoretically predicted for the case of organic polaritons [161]. Such study, which will be supported by a detailed theoretical simulation of the system, is effectively under consideration.

The last section of chapter 5 was entirely dedicated to the characterization of polariton electroluminescence of the hybrid microcavity LED. The light–emitting–diode scheme implemented in the structure allows for efficient carriers injection through the inorganic conductive layers, directly into the quantum wells. As such, high conductivity typical of inorganic semiconductors was exploited together with robust oscillator strength of the organic dye. Owing to strong light–matter interaction the electrically injected excitation is distributed among the upper, middle and lower polariton branch states preventing the formation of the uncoupled Frenkel exciton reservoir (ER) which forms under nonresonant optical pumping and that provides important loss channels. Finally, through the simulation of the observed results, the electrically driven strong coupling regime was

shown to maintain identical coupling strength as observed in the case of optical excitation and therefore preserve polariton nonlinear features.
Among the advantages discussed along the present work, this study also provides all the ingredients for a simple reproduction of a hybrid structure which comprehend semiconductors able to sustain strong coupling even at room temperature. Strong optical coupling based on GaN (InGaN) quantum wells and near UV organic compounds (NTCDA and anthracene) have been already shown [3, 31, 48] and therefore their simultaneous implementation in a single microcavity structure could present only engineering related issues. This consists in one of the main potentiality of our approach. Implementation of such materials for the achievements of hybrid polaritons which possess strong particle nonlinearities suggests the realistic possibility to attain Bose–Einstein condensation of polariton at room temperature. Such experimental discovery would surely represents a breakthrough in the physics of planar microcavities which will open alternative routes to traditional inorganic or organic based systems. Due to the mixed nature of the hybrid bosonic particles one should also consider that the interpretation of related phenomena could possibly vary from the present knowledge of organic or inorganic strong photon coupling. In fact, as already demonstrated by the negative middle polariton dispersion here reported, unexpected phenomena could origin from the hybridization process and give rise eventually to a new interesting and unexplored physics.

7 Appendix A: Experimental Methods

7.1 Z-scan Experiment

In the Z-scan technique the far field sample transmittance of a focused Gaussian beam is measured through a finite aperture as function of the position of the material relative to the beam waist. A scheme of the experimental setup is shown for simplicity in figure 7.1. Transmittance variation is recorded with a large area photodiode (Newport, 818-SL photodetector) capable of pW sensibility and then plotted as function of the sample position Z in relation to the beam focus. The laser source used in our experiment is provided by the frequency doubled signal of an optical parametric oscillator (OPO) pumped by a femtosecond Titanium:Sapphire laser. Via OPO and subsequent second harmonic generation (SHG), we obtained a wide range energy tuneable pulse beam with 200 fs width and 80 MHz repetition rate. For our analysis we used three different excitation energies: off resonance (1.97 eV and 2.39 eV) and near resonance (2.17 eV) of the first excitonic transition of the dye here investigated, where 50% change in the linear absorption was observed in the measured spectra.

Starting the scan from a distance far away from the focus, the beam irradiance is low; negligible non–linear refraction occurs and the transmittance remains constant. As the sample moves towards the focus the beam irradiance increases (in case of negative non-linear refractive index) due to sample self–focusing: beam narrowing occurs at the aperture positioned in front of the collection system and increased of the transmittance is observed.
As the scan continues and the sample passes the focal plane, self–defocusing increases the beam divergence leading to beam broadening and further reduction of transmittance. The Z–scan is then completed as the sample is moved away from the focus where the transmittance becomes once again linear due to low irradiance. If the aperture shown in figure 7.1 is removed, the Z-scan becomes insensitive to nonlinear refraction and results in a null signal unless absorptive nonlinearity is present. In this case, the so called "open aperture Z–scan", nonlinear absorption coefficient can be extracted from

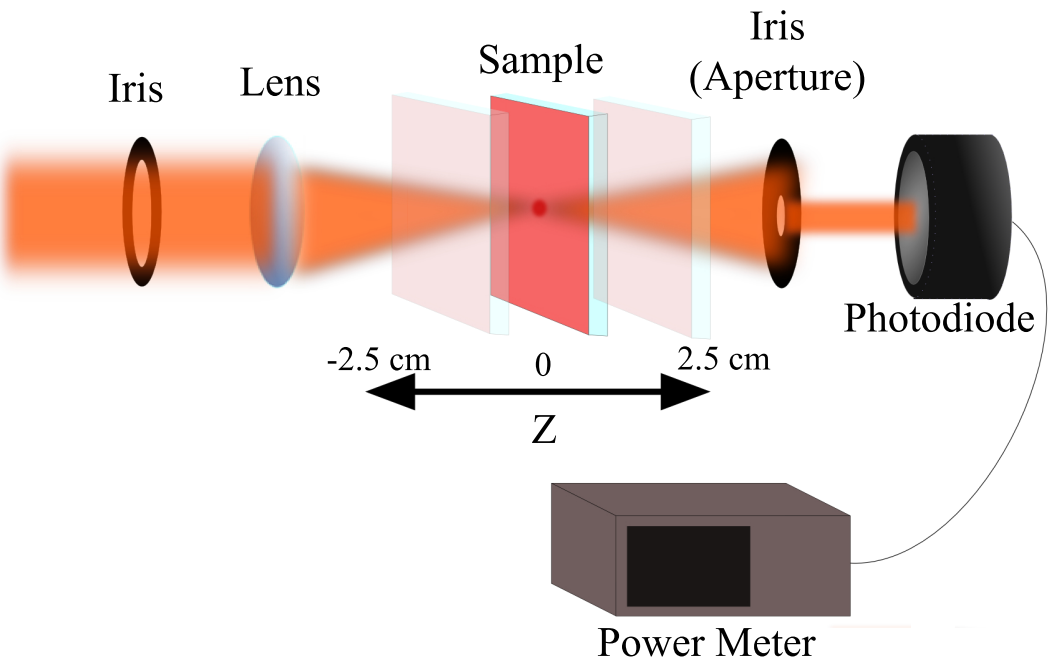

Figure 7.1: Schematic drawing of the Z–scan setup. While the first iris modifies the beam waist, the second aperture (open or close) permits to swap in between nonlinear absorption or nonlinear refraction type measurements. The sample was moved along the focal point with a total path length of 5 cm and sensibility of 0.1 mm provided by a piezoelectric translational stage.

the resulting transmittance curve. On the other side, the "close aperture Z–scan" can be used separately to determine nonlinear refraction which is sensitive to the size of the aperture. This could be done only by previous removal of nonlinear absorption contribution by dividing the close aperture transmittance curve by the open one.
For each of the two analysis a separate approach has to be use in order to extract values for nonlinear absorption and nonlinear refractive index.

We report below the equations which describe a close aperture Z–scan and refer the reader to section 3.2 for the treatise of the open aperture case.

In case of a close aperture Z–scan the transmitted signal is sensitive to the beam distortion and nonlinear refractive index can be extracted.
In the assumption of thin samples, the electric field induced phase distortion is described as:

$$\frac{d\phi(Z,t)}{dz'} = \frac{2\pi}{\lambda} n_2 I(Z,t). \tag{7.1}$$

Here z' is the propagation depth in the sample, λ is the laser wavelength, I the beam intensity and $\Delta\phi_0(0,0)$ is the peak–on–axis phase shift, empirically detemined by measuring the peak to valley difference in the transmittance curve:

$$\Delta T_{pv} \cong 0.406(1-S)^{0.27} \left|\Delta\phi_0\right|. \tag{7.2}$$

While S is related to the aperture size, assumed $S = 0.4$ in case of close aperture and $S = 1$ in case of the open one, relation 7.2 is directly calculated from the normalized transmittance function in the limit of far field condition, small nonlinear phase change ($|\Delta\phi_0| << 1$) and assuming no radial variation of the electric field profile $E_a(r = 0)$:

$$T(z, \Delta\phi_0) = 1 - \frac{4\Delta\phi_0 x}{(x^2 + 9)(x^2 + 1)}. \tag{7.3}$$

Here $x = z/z_0$.

An extended and detailed description of the Z–scan technique and theory can be found in references [103, 162].

7.2 Angle Resolved Photoluminescence/Electroluminescence

Characterization and investigation of organic, inorganic and hybrid microcavities properties were performed along this thesis by angularly resolving polariton emission which followed optical or electrical excitation. The sample was held on a translational stage and kept either at room temperature (organic MCs) or cooled at cryogenic temperatures (≈15 Kelvin) via a standard cold–finger cryostat (inorganic and hybrid MCs) to prevent exciton dissociation in GaAs quantum wells which usually occurs at about 100 Kelvin. In case of optical pumping the sample was excited at an angle of $\approx 30^o$ with respect to the surface, by a 5 cm focal length lens. Photoluminescence emission instead was collected through a microscope objective lens of NA 0.7. The Fourier plane behind the objective which contains the k–space of the polariton emission (angular emission is mapped to the radial position on the plane) is imaged directly onto the slit of a monochromator equipped with a water–cooled charge coupled device (CCD) to obtain energy Vs wavevector ($k_{||}$) resolution, i.e. wavelength Vs angle (figure 7.2). Before monocromation, a longpass filter was used to remove any residual of the laser pump.
Different laser configurations were used along this work depending on the active layer which composed the microcavity device under investigation. A tuneable Titanium–Sapphire oscillator which delivers ≈100 fs pulses with a repetition rate of 80 MHz or a tuneable Titanium:Sapphire continuous wave source were implemented to excite inorganic and hybrid microcavities with near IR beam energies (chapter 5). On the other hand, for power dependence measurements presented in the same chapter (section 5.4), the previous system was coupled to an amplifier to reduce the repetition rate to 100 kHz. Besides, in case of organic based MCs, the compressed and amplified pulses were subsequently coupled to an Optical Parametric Amplifier (OPA) to allow for frequency tuning in the visible range (400nm–650nm). The Ti:Sapph–amplifier–OPA system was chosen to efficiently pump the organic dyes and reduce at the same time characteristic photobleaching effects by means of low repetition rate pulses (250 kHz).

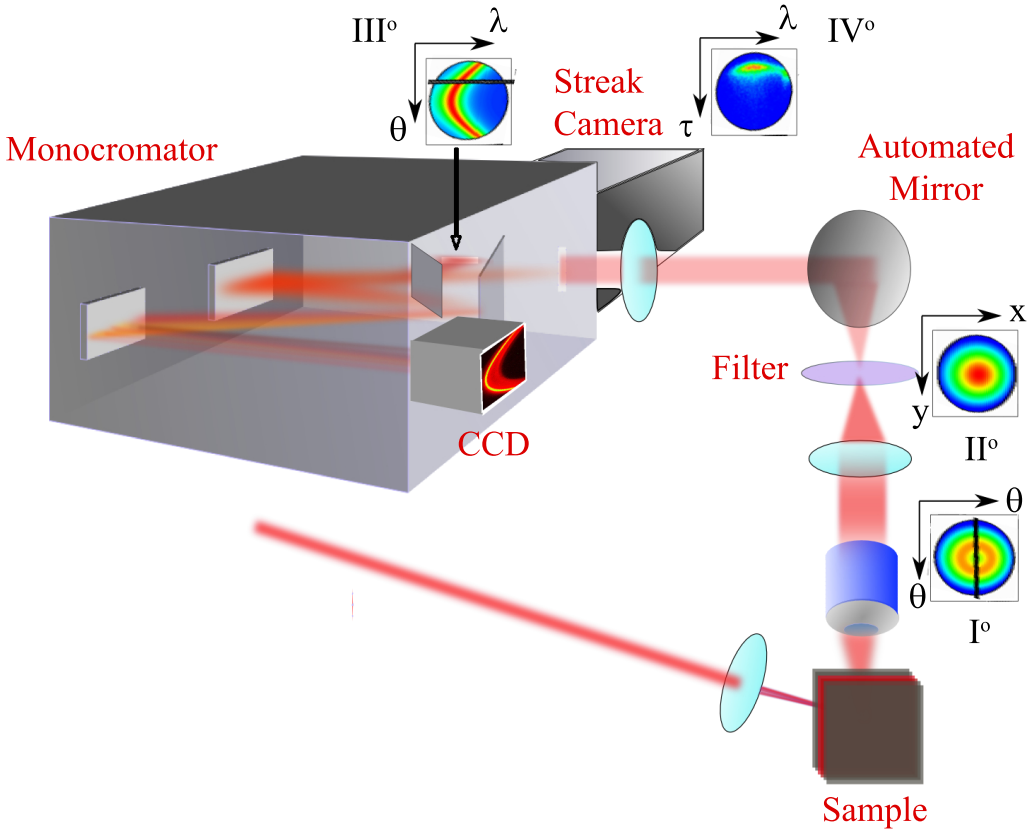

Figure 7.2: Cartoon representation of the full experimental setup used for angle resolved photoluminescence/electroluminescence imaging and time resolved analysis. For guidance, (I^o, III^o) k–space, (II^o) real space and (IV^o) energy Vs time dispersions are shown at the specific positions along the setup.

In case of hybrid microcavity light emittion diodes, strong coupling regime was investigated also by means of electrical excitation.
Through injection of carriers into the semiconductor quantum wells, formation of hybrid polariton particles was achieved under conditions and processes specifically described in chapter 5.5. A voltage generator which provides DC voltage and low current values was used for the purpose. This allowed to prevent damages on the sensible organic layer and hence maintain stable strong coupling regime conditions. Besides, polariton emission was collected through the same modalities explained above and sketched in figure 7.2 for the case of optical excitation.

7.3 Time Resolved Analysis

The setup described above was also equipped with a streak camera which provided the oppurtunity to investigate temporal dynamics of the angularly dispersed polariton photoluminescence and electroluminescence emission. The k–space signal in fact, following monocromation, was directly imaged onto an horizontal slit used to select the desired

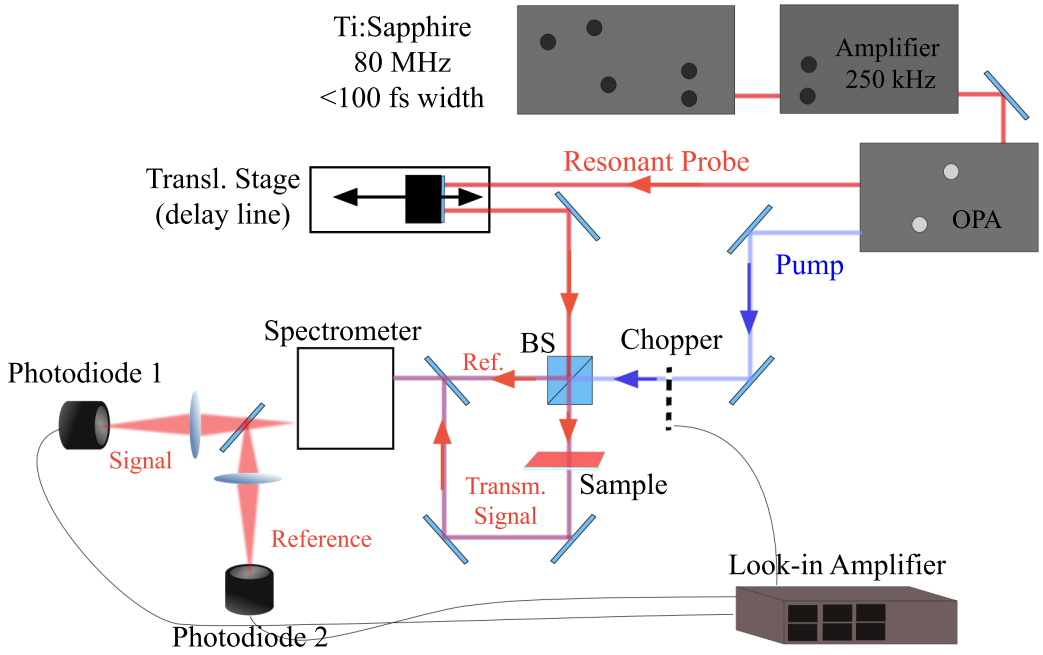

Figure 7.3: Schematic drawing of the two beam pump–probe setup fully described in the main text.

range of angles to couple to the streak camera. A fully automated mirror positioned outside the monocromator allowed to selectively resolve in energy and time specific polariton states on the branch dispersion. Experimental results of such analysis are presented and extensively discussed in chapter 4.3.
A schematic representation of the entire setup is displayed in figure 7.2

7.4 Pump-Probe Spectroscopy

In the presence of systems governed by ultra–fast dynamics, transient pump–probe spectroscopy represents the simpliest way to study their temporal evolution.
This technique is based on an initial ultrashort pulse beam which is then split into two terms, used to "pump" and "probe" the process under study. In our case, the initial Ti:Sapph femtosecond pulse (≈100 fs at 80 MHz and 1.55 eV) is at first amplified and compressed to achieve a repetion rate of 250 kHz. Through optical parametric amplification (OPA) two different beams are then obtained: a strong nonresonant pump term at 3.1 eV, used to excite the system, and a weaker probe constantly adjusted to resonantly follow the lower polariton dispersion energy. At the same time the sample was rotated to follow the angular dispersion of the LP branch. By monitoring the transmittance variation of the probe as function of its delay (≈35 fs time resolution) with respect to the arrival of the pump, detailed informations about relaxation time of each polariton state on the lower branch can be extracted (section 3.3).

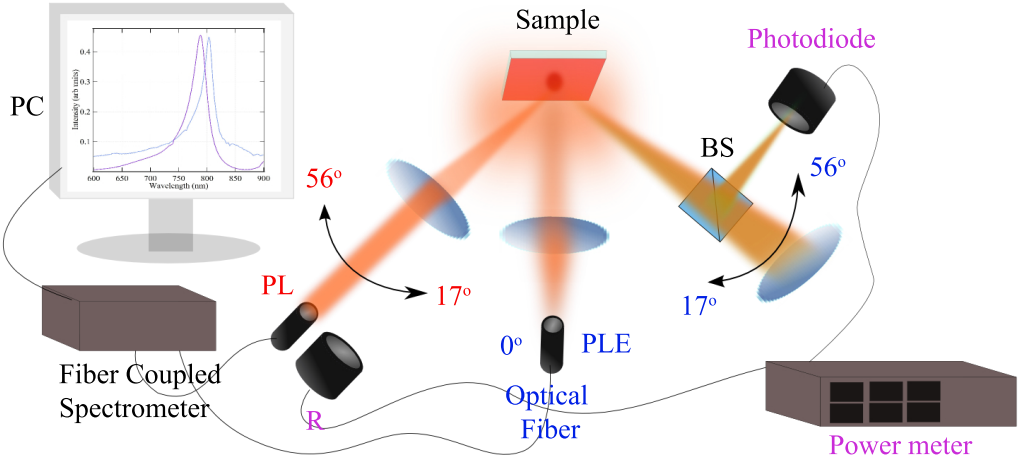

Figure 7.4: Simplified scheme of the PL, PLE, reflectivity setup used to characterize hybrid organic–organic MCs. Excitation/collection systems for photoluminescence, PLE and reflectance are displayed in red, blue and purple colors respectively.

The full scheme of the setup is presented in figure 7.3. Due to the difficult purpose of the experiment, the setup was designed to allow sample excitation with collinear pump and probe beams. By combining this configuration with small spot sizes, we are able to focus the analysis on tiny portions of the sample (area $\approx 320\mu m^2$) and hence study polariton states with high energy precision. At the same time, we made use of a single grating spectrometer coupled with a balance detection scheme to remove any scattered light due to the pump term and enhance the signal–to–noise ratio. As result, we obtained clear decay curves which theoretical fitting provide important informations about polarito build–up times (section 3.3).

7.5 PL and PLE spectroscopy

In the present section we describe the experimental techniques and related setup exploited for the characterization and study of hybrid organic–organic microcavities, extensively discussed in chapter 4.3. The full setup configuration, schematically displayed in figure 7.4, allowed for angular resolved photoluminescence (PL), photoluminescence excitation (PLE) spectroscopy and reflectance measurements. The sample was mounted in a cryostat with wide angular access window positioned in the optical axis of a two rotating arms goniometer. For PL measurements, the sample was maintained at a pressure of $< 1 \times 10^{-4}$ mbar in order to reduce the effect of photo-oxidation while nonresonantly excited at a large angle (out of the plane of collection, $\approx 40^o$) with a 473 nm CW diode laser focused on a spot of diameter $\approx 200\mu m$. Photoluminescence emission was collected on the second arm of the goniometer and coupled with a 5 mm liquid–core optical fiber to a spectrometer. The collection arm was automatically scanned through the range of

angles from 0^o to 56^o in increments of 1^o. This permitted to energy resolve the entire polariton branches up to the anticrossing point.

For PLE measurements instead, optical excitation was provided by a quasi–CW laser system with 6 ps pulses at 40 MHz. The excitation spot was focused to a point of approximately $500\mu m$ in diameter centered on the same position on the sample as the PL excitation spot. The collection angle was fixed at normal incidence while a fiber coupled spectrometer was used, as before for PL, to collect the emission. Additionally, a longpass filter was implemented to block the scattered excitation light from the collection fiber. The excitation angle was spanned from 17^o to 56^o in increments of 1^o while, at each angle, the excitation wavelength was scanned between 530 nm and 670 nm with a resolution of 2 nm to encompass the entire polariton region.
In case of the microcavity sample, lower polariton branch emission in each PL spectrum was fit with a Lorentzian curve, which amplitude represents a single point of the PLE image.

Furthermore, for the reason explained in the text above (chapter 4.3), the excitation light reflected by the sample was collected with a silicon photodiode and the intensity measured with a dual source power meter.
The excitation beam intensity was also sampled and measured prior to reach the sample with a second photodiode in order to normalize the reflected light and hence obtain the reflectivity of the sample R. Assuming no transmission through the sample, cavity absorption would be simply given by 1-R.

References

[1] N. Somaschi, L. Mouchliadis, D. Coles, I. E. Perakis, D. G. Lidzey, P. G. Lagoudakis, and P. G. Savvidis, Ultrafast polariton population build-up mediated by molecular phonons in organic microcavities **99**, 143303 (2011).

[2] M. Schwoerer and H. C. Wolf, Organic Molecular Solids, John Wiley and Sons (2007).

[3] M. Litinskaya, P. Reineker, and V. Agranovich, Exciton–polaritons in organic microcavities, *Journal of Luminescence* **119120**, 277 (2006).

[4] J. Frenkel, On the transformation of light into heat in solids. II, *Phys. Rev.* **37**, 1276 (1931).

[5] A. Herz, Aggregation of sensitizing dyes in solution and their adsorption onto silver halides, *Advances in Colloid and Interface Science* **8**, 237 (1977).

[6] L. V. H. van Amerongen and R. van Grondelle, Photosynthetic Excitons, World Scientific, Singapore (2000).

[7] M. Kasha and B. di Bartolo (Ed.), Spectroscopy of the Excited State, Vol. B12, Plenum, New York (1976).

[8] S. de Boer, K. J. Vink, and D. A. Wiersma, Optical dynamics of condensed molecular aggregates: An accumulated photon-echo and hole-burning study of the j-aggregate, *Chemical Physics Letters* **137**, 99 (1987).

[9] B. Coffey and R. Friedberg, Effect of short-range coulomb interaction on cooperative spontaneous emission, *Phys. Rev. A* **17**, 1033 (1978).

[10] B. I. Greene, J. Orenstein, and S. Schmitt-Rink, All-optical nonlinearities in organics, *Science* **247**, 679 (1990), PMID: 17771884.

[11] S. Schmitt-Rink, D. S. Chemla, and D. A. B. Miller, Theory of transient excitonic optical nonlinearities in semiconductor quantum-well structures, *Phys. Rev. B* **32**, 6601 (1985).

[12] H. M. Gibbs, Optical Bistability: Controling Light with Light, Academic Press, New York (1985).

[13] S. P. S. (Ed.), Dye Lasers, Springer-Verlag, Berlin (1990).

[14] F. J. Duarte and L. W. H. (Eds.), Dye Laser Principles, Academic, New York (1990).

[15] A. Bernanose, M. Comte, and P. Vouaux, A new method of emission of light by certain organic compounds, *J. Chem. Phys.* **50**, 64 (1953).

[16] M. Pope, H. Kallmann, and P. Magnate, Light emission from organic material, *J. Chem. Phys.* **38**, 2 (1963).

[17] N. C. Greenham, S. C. Moratti, D. D. C. Bradley, R. H. Friend, and A. B. Holmes, Efficient light-emitting diodes based on polymers with high electron affinities, *Nature* **365**, 628 (1993).

[18] M. Pope and C. E. Swenberg, Electronic Processes in Organic Crystals, Oxford University Press (1999).

[19] G. E. Moore, Cramming more components onto integrated circuits, reprinted from electronics, volume 38, number 8, april 19, 1965, pp.114 ff., *IEEE Solid-State Circuits Society Newsletter* **11**, 33 (2006).

[20] J. D. Bernal, The Social Function of Science, George Routledge and Sons Ltd., London (1939).

[21] R. R. (Ed.), Civilization at the Crossroads, ME Sharp, New York (1969).

[22] D. Bell, Sociological Journeys: Essays 19601980, Heinmann, London (1980).

[23] K. Iga, Vertical-cavity surface-emitting laser: Its conception and evolution **47**, 1 (2008).

[24] P. R. Berman and D. E. Bates, Cavity Quantum Electrodynamics (Advances in Atomic, Molecular and Optical Physics), Academic Press, Inc., San Diego (1994).

[25] C. Weisbuch, M. Nishioka, A. Ishikawa, and Y. Arakawa, Observation of the coupled exciton-photon mode splitting in a semiconductor quantum microcavity, *Phys. Rev. Lett.* **69**, 3314 (1992).

[26] A. Imamoglu, R. J. Ram, S. Pau, and Y. Yamamoto, Nonequilibrium condensates and lasers without inversion: Exciton-polariton lasers, *Phys. Rev. A* **53**, 4250 (1996).

[27] P. G. Savvidis, J. J. Baumberg, R. M. Stevenson, M. S. Skolnick, D. M. Whittaker, and J. S. Roberts, Angle-resonant stimulated polariton amplifier, *Phys. Rev. Lett.* **84**, 1547 (2000).

[28] R. M. Stevenson, V. N. Astratov, M. S. Skolnick, D. M. Whittaker, M. Emam-Ismail, A. I. Tartakovskii, P. G. Savvidis, J. J. Baumberg, and J. S. Roberts, Continuous wave observation of massive polariton redistribution by stimulated scattering in semiconductor microcavities, *Phys. Rev. Lett.* **85**, 3680 (2000).

[29] J. Kasprzak, M. Richard, S. Kundermann, A. Baas, P. Jeambrun, J. M. J. Keeling, F. M. Marchetti, M. H. Szymaska, R. Andr, J. L. Staehli, V. Savona, P. B. Littlewood, B. Deveaud, and L. S. Dang, BoseEinstein condensation of exciton polaritons, *Nature* **443**, 409 (2006).

[30] S. Christopoulos, G. B. H. von Hgersthal, A. J. D. Grundy, P. G. Lagoudakis, A. V. Kavokin, J. J. Baumberg, G. Christmann, R. Butt, E. Feltin, J.-F. Carlin, and N. Grandjean, Room-temperature polariton lasing in semiconductor microcavities, *Phys. Rev. Lett.* **98**, 126405 (2007).

[31] G. Christmann, R. Butt, E. Feltin, J.-F. Carlin, and N. Grandjean, Room temperature polariton lasing in a GaN/AlGaN multiple quantum well microcavity, *Applied Physics Letters* **93**, 051102 (2008).

[32] I. Shelykh, K. V. Kavokin, A. V. Kavokin, G. Malpuech, P. Bigenwald, H. Deng, G. Weihs, and Y. Yamamoto, Semiconductor microcavity as a spin-dependent optoelectronic device, *Phys. Rev. B* **70**, 035320 (2004).

[33] K. G. Lagoudakis, M. Wouters, M. Richard, A. Baas, I. Carusotto, R. Andr, L. S. Dang, and B. Deveaud-Pldran, Quantized vortices in an exciton-polariton condensate, *Nat Phys* **4**, 706 (2008).

[34] A. Amo, T. C. H. Liew, C. Adrados, R. Houdr, E. Giacobino, A. V. Kavokin, and A. Bramati, Excitonpolariton spin switches, *Nat Photon* **4**, 361 (2010).

[35] T. C. H. Liew, A. V. Kavokin, T. Ostatnick, M. Kaliteevski, I. A. Shelykh, and R. A. Abram, Exciton-polariton integrated circuits, *Phys. Rev. B* **82**, 033302 (2010).

[36] F. London, The lambda–phenomenon of liquid helium and the bose-einstein degeneracy, *Nature* **141**, 634 (1938).

[37] P. Kapitza, Viscosity of liquid helium below the lambda–point, *Nature* **141**, 913 (1938).

[38] A. Kavokin, G. Malpuech, and F. P. Laussy, Polariton laser and polariton superfluidity in microcavities, *Physics Letters A* **306**, 187 (2003).

[39] I. Carusotto and C. Ciuti, Probing microcavity polariton superfluidity through resonant rayleigh scattering, *Phys. Rev. Lett.* **93**, 166401 (2004).

[40] A. Amo, J. Lefrre, S. Pigeon, C. Adrados, C. Ciuti, I. Carusotto, R. Houdr, E. Giacobino, and A. Bramati, Superfluidity of polaritons in semiconductor microcavities, *Nat Phys* **5**, 805 (2009).

[41] O. A. Egorov, D. V. Skryabin, A. V. Yulin, and F. Lederer, Bright cavity polariton solitons, *Phys. Rev. Lett.* **102**, 153904 (2009).

[42] D. G. Lidzey, D. D. C. Bradley, M. S. Skolnick, T. Virgili, S. Walker, and D. M. Whittaker, Strong excitonphoton coupling in an organic semiconductor microcavity, *Nature* **395**, 53 (1998).

[43] J. R. Tischler, M. S. Bradley, V. Bulovi, J. H. Song, and A. Nurmikko, Strong coupling in a microcavity LED, *Phys. Rev. Lett.* **95**, 036401 (2005).

[44] S. I. Tsintzos, N. T. Pelekanos, G. Konstantinidis, Z. Hatzopoulos, and P. G. Savvidis, A GaAs polariton light-emitting diode operating near room temperature, *Nature* **453**, 372 (2008).

[45] T. Virgili, D. Coles, A. M. Adawi, C. Clark, P. Michetti, S. K. Rajendran, D. Brida, D. Polli, G. Cerullo, and D. G. Lidzey, Ultrafast polariton relaxation dynamics in an organic semiconductor microcavity, *Physical Review B* **83**, 245309 (2011).

[46] D. M. Coles, P. Michetti, C. Clark, W. C. Tsoi, A. M. Adawi, J.-S. Kim, and D. G. Lidzey, Vibrationally assisted polariton-relaxation processes in strongly coupled organic-semiconductor microcavities, *Advanced Functional Materials* **21**, 36913696 (2011).

[47] N. Christogiannis, N. Somaschi, P. Michetti, D. M. Coles, P. G. Savvidis, P. G. Lagoudakis, and D. G. Lidzey, Characterizing the electroluminescence emission from a strongly coupled organic semiconductor microcavity LED, *Advanced Optical Materials* **1**, 503509 (2013).

[48] S. Kena-Cohen and S. R. Forrest, Room-temperature polariton lasing in an organic single-crystal microcavity, *Nat Photon* **4**, 371 (2010).

[49] V. Agranovich, H. Benisty, and C. Weisbuch, Organic and inorganic quantum wells in a microcavity: Frenkel-wannier-mott excitons hybridization and energy transformation, *Solid State Communications* **102**, 631 (1997).

[50] V. M. Agranovich, D. M. Basko, G. C. L. Rocca, and F. Bassani, Excitons and optical nonlinearities in hybrid organic-inorganic nanostructures **10**, 9369 (1998).

[51] M. Born and E. Wolf, Principles of Optics 7th ed., Cambridge University Press (1999).

[52] G. H. Wannier, The structure of electronic excitation levels in insulating crystals, *Phys. Rev.* **52**, 191 (1937).

[53] H. Haken, Quantum Field Theory of Solids: An Introduction, Elsevier Science and Technology (1976).

[54] L. Apker and E. Taft, Photoelectric emission from f-centers in KI, *Phys. Rev.* **79**, 964 (1950).

[55] E. Knapp, Lineshapes of molecular aggregates, exchange narrowing and intersite correlation, *Chemical Physics* **85**, 73 (1984).

[56] E. Knapp, P. Scherer, and S. Fischer, On the lineshapes of vibronically resolved molecular aggregate spectra. application to pseudoisocyanin (PIC), *Chemical Physics Letters* **111**, 481 (1984).

[57] M. van Burgel, D. A. Wiersma, and K. Duppen, The dynamics of onedimensional excitons in liquids **102**, 20 (1995).

[58] P. O. Scherer, J–aggregates (Ed. T. K. Kobayashi), Singapore: World Scientific (1996).

[59] E. E. Jelley, Spectral absorption and fluorescence of dyes in the molecular state : Abstract : Nature, *Nature* **138** (1936).

[60] E. E. Jelley, Molecular, nematic and crystal states of i: I-diethyl–cyanine chloride : Abstract : Nature, *Nature* **139** (1937).

[61] G. Scheibe, ber die vernderlichkeit des absorptionsspektrums einiger sensibilisierungsfarbstoffe und deren ursache., *Angew.Chem.* **49** (1936).

[62] G. Scheibe, ber die vernderlichkeit der absorptionsspektren in lsungen und die nebenvalenzen als ihre ursache **50**, 212219 (1937).

[63] D. F. O'Brien, J–aggregate in monomolecular layers of cyanine dyes, *Photogr.Sci.Eng.* **18** (1974).

[64] M. C. Petty, Langmuir–Blodgett Films, Cambridge University Press (1996).

[65] H. Fukumoto and Y. Yonezawa, Layer-by-layer self-assembly of polyelectrolyte and water soluble cyanine dye, *Thin Solid Films* **327329**, 748 (1998).

[66] S. De Boer and D. A. Wiersma, Dephasing-induced damping of superradiant emission in j-aggregates, *Chemical Physics Letters* **165**, 45 (1990).

[67] H. Fidder, J. Knoester, and D. A. Wiersma, Superradiant emission and optical dephasing in j-aggregates, *Chemical Physics Letters* **171**, 529 (1990).

[68] V. L. Bogdanov, E. N. Viktorova, S. V. Kulya, and A. S. Spiro, *JETP Lett.* **53** (1991).

[69] R. Markov, A. Plekhanov, V. Shelkovnikov, and J. Knoester, Giant nonlinear optical response of interacting one-dimensional frenkel excitons in molecular aggregates **221**, 529533 (2000).

[70] A. D. Kachkovskii, The nature of electronic transitions in linear conjugated systems, *Russ. Chem. Rev.* **66**, 647 (1997).

[71] E. G. McRae and M. Kasha, Enhancement of phosphorescence ability upon aggregation of dye molecules **28**, 721 (1958).

[72] M. Kasha, Relation between exciton bands and conduction bands in molecular lamellar systems, *Rev. Mod. Phys.* **31**, 162 (1959).

[73] V. M. Agranovich and G. F. Bassani, Thin Films and Nanostructures: Electronic Excitations in Organic Based Nanostructures, Volume 31 (Ed. V. M. Agranovich and G. F. Bassani), Elsevier Science and Technology (2003).

[74] N. W. Ashcroft and N. D. Mermin, Solid State Physics, Saunders College (1976).

[75] J. Singh, Optical Properties of Condensed Matter and Applications, John Wiley and Sons (2006).

[76] V. Savona, L. Andreani, P. Schwendimann, and A. Quattropani, Quantum well excitons in semiconductor microcavities: Unified treatment of weak and strong coupling regimes, *Solid State Communications* **93**, 733 (1995).

[77] J. J. Hopfield, Theory of the contribution of excitons to the complex dielectric constant of crystals, *Phys. Rev.* **112**, 1555 (1958).

[78] A. Kavokin, G. Malpuech, and W. Langbein, Theory of propagation and scattering of excitonpolaritons in quantum wells, *Solid State Communications* **120**, 259 (2001).

[79] V. M. Agranovich, M. Litinskaia, and D. G. Lidzey, Cavity polaritons in microcavities containing disordered organic semiconductors, *Phys. Rev. B* **67**, 085311 (2003).

[80] P. Michetti and G. C. La Rocca, Polariton states in disordered organic microcavities, *Phys. Rev. B* **71**, 115320 (2005).

[81] V. Agranovich and G. La Rocca, Electronic excitations in organic microcavities with strong lightmatter coupling, *Solid State Communications* **135**, 544 (2005).

[82] M. Litinskaya, Propagation and localization of polaritons in disordered organic microcavities, *Physics Letters A* **372**, 3898 (2008).

[83] M. Litinskaya and P. Reineker, Loss of coherence of exciton polaritons in inhomogeneous organic microcavities, *Phys. Rev. B* **74**, 165320 (2006).

[84] F. Tassone and Y. Yamamoto, Exciton-exciton scattering dynamics in a semiconductor microcavity and stimulated scattering into polaritons, *Phys. Rev. B* **59**, 10830 (1999).

[85] R. Balili, V. Hartwell, D. Snoke, L. Pfeiffer, and K. West, Bose-einstein condensation of microcavity polaritons in a trap, *Science* **316**, 1007 (2007), PMID: 17510360.

[86] C. Schneider, A. Rahimi-Iman, N. Y. Kim, J. Fischer, I. G. Savenko, M. Amthor, M. Lermer, A. Wolf, L. Worschech, V. D. Kulakovskii, I. A. Shelykh, M. Kamp, S. Reitzenstein, A. Forchel, Y. Yamamoto, and S. Hfling, An electrically pumped polariton laser, *Nature* **497**, 348 (2013).

[87] F. Tassone, C. Piermarocchi, V. Savona, A. Quattropani, and P. Schwendimann, Bottleneck effects in the relaxation and photoluminescence of microcavity polaritons, *Phys. Rev. B* **56**, 7554 (1997).

[88] A. I. Tartakovskii, M. Emam-Ismail, R. M. Stevenson, M. S. Skolnick, V. N. Astratov, D. M. Whittaker, J. J. Baumberg, and J. S. Roberts, Relaxation bottleneck and its suppression in semiconductor microcavities, *Phys. Rev. B* **62**, R2283 (2000).

[89] P. G. Lagoudakis, M. D. Martin, J. J. Baumberg, A. Qarry, E. Cohen, and L. N. Pfeiffer, Electron-polariton scattering in semiconductor microcavities, *Phys. Rev. Lett.* **90**, 206401 (2003).

[90] P. Michetti and G. C. La Rocca, Exciton-phonon scattering and photoexcitation dynamics in j-aggregate microcavities, *Phys. Rev. B* **79**, 035325 (2009).

[91] J. Chovan, I. E. Perakis, S. Ceccarelli, and D. G. Lidzey, Controlling the interactions between polaritons and molecular vibrations in strongly coupled organic semiconductor microcavities, *Phys. Rev. B* **78**, 045320 (2008).

[92] D. G. Lidzey, A. M. Fox, M. D. Rahn, M. S. Skolnick, V. M. Agranovich, and S. Walker, Experimental study of light emission from strongly coupled organic semiconductor microcavities following nonresonant laser excitation, *Phys. Rev. B* **65**, 195312 (2002).

[93] D. G. Lidzey, D. D. C. Bradley, T. Virgili, A. Armitage, M. S. Skolnick, and S. Walker, Room temperature polariton emission from strongly coupled organic semiconductor microcavities, *Phys. Rev. Lett.* **82**, 3316 (1999).

[94] P. G. Savvidis, L. G. Connolly, M. S. Skolnick, D. G. Lidzey, and J. J. Baumberg, Ultrafast polariton dynamics in strongly coupled zinc porphyrin microcavities at room temperature, *Phys. Rev. B* **74**, 113312 (2006).

[95] S. Kena-Cohen, M. Davano, and S. R. Forrest, Strong exciton-photon coupling in an organic single crystal microcavity, *Phys. Rev. Lett.* **101**, 116401 (2008).

[96] H. P. Lovercraft, Exciton Dynamics in Cylindrical Molecular Aggregates (Chapter 4), Academic Press, Inc., San Diego (1994).

[97] T. Pritchett, Models for Saturable and Reverse Saturable Absorption in Materials for Optical Limiting, Adelphi (2002).

[98] C. Li, L. Zhang, R. Wang, Y. Song, and Y. Wang, Dynamics of reverse saturable absorption and all-optical switching in c60, *J. Opt. Soc. Am. B* **11**, 1356 (1994).

[99] N. K. M. N. Srinivas, S. V. Rao, and D. N. Rao, Saturable and reverse saturable absorption of rhodamine b in methanol and water, *J. Opt. Soc. Am. B* **20**, 2470 (2003).

[100] D. N. Christodoulides, I. C. Khoo, G. J. Salamo, G. I. Stegeman, and E. W. Van Stryland, Nonlinear refraction and absorption: mechanisms and magnitudes, *Adv. Opt. Photon.* **2**, 60 (2010).

[101] G. M. Akselrod, Y. R. Tischler, E. R. Young, D. G. Nocera, and V. Bulovic, Exciton-exciton annihilation in organic polariton microcavities, *Physical Review B* **82**, 113106 (2010).

[102] D. C. Hutchings, M. Sheik-Bahae, D. J. Hagan, and E. W. V. Stryland, Kramers-krnig relations in nonlinear optics, *Optical and Quantum Electronics* **24**, 1 (1992).

[103] M. Sheik-Bahae, A. Said, T.-H. Wei, D. Hagan, and E. W. Van Stryland, Sensitive measurement of optical nonlinearities using a single beam, *IEEE Journal of Quantum Electronics* **26**, 760 (1990).

[104] T. H. Wei, D. J. Hagan, M. J. Sence, E. W. Stryland, J. W. Perry, and D. R. Coulter, Direct measurements of nonlinear absorption and refraction in solutions of phthalocyanines, *Appl.Phys.B* **54**, 46 (1992).

[105] L. Yang, R. Zamboni, C. Taliani, R. Dorsinville, Q. Z. Wang, P. X. Ye, and R. R. Alfano, Excited-state nonlinearity in polythiophene thin films investigated by the z-scan technique, *Opt. Lett.* **17**, 323 (1992).

[106] Z. R. Chen, H. W. Hou, X. Q. Xin, K. B. Yu, and S. Shi, A half-open cage-shaped cluster, (NEt4)3[WOS3(CuBr)3(.mu.2-Br)].cntdot.2H2O: synthesis, structure, and nonlinear optical properties, *J. Phys. Chem.* **99**, 8717 (1995).

[107] G. Fang, Y. Song, Y. Wang, X. Zhang, C. Li, L.-C. Song, and P.-C. Liu, Z-scan of excited-state nonlinear materials with reverse saturable absorption, *Optics Communications* **183**, 523 (2000).

[108] G. Fang, Y. Song, Y. Wang, X. Zhang, Chunfei Li, C. Zhang, and X. Xin, Nonlinear optical and optical limiting properties of a novel cluster [WS4Cu4I2(py)6], *Optics Communications* **181**, 97 (2000).

[109] C. Zhang, Y. Song, F. E. Khn, Y. Wang, H. Fun, X. Xin, and W. A. Hermann, Sign alteration of the nonlinear refraction of isomorphous cubane-shaped heterothiometallic clusters originating from a skeleton atomic effect, *New J. Chem.* **26**, 58 (2002).

[110] M. Bednarz and J. Knoester, The linear absorption and PumpProbe spectra of cylindrical molecular aggregates, *J. Phys. Chem. B* **105**, 12913 (2001).

[111] V. V. Egorov and M. V. Alfimov, Theory of the j-band: from the frenkel exciton to charge transfer, *Phys.-Usp.* **50**, 985 (2007).

[112] D. N. Krizhanovskii, R. Butt, L. G. Connolly, A. I. Tartakovskii, D. G. Lidzey, M. S. Skolnick, and S. Walker, Photoluminescence emission and raman scattering polarization in birefringent organic microcavities in the strong coupling regime, *Journal of Applied Physics* **93**, 5003 (2003).

[113] H. Fidder, J. Knoester, and D. A. Wiersma, Optical properties of disordered molecular aggregates: A numerical study, *J. Chem. Phys.* **95**, 7880 (1991).

[114] V. Malyshev and P. Moreno, Hidden structure of the low-energy spectrum of a one-dimensional localized frenkel exciton, *Phys. Rev. B* **51**, 14587 (1995).

[115] S. M. Vlaming, V. A. Malyshev, and J. Knoester, Localization properties of one-dimensional frenkel excitons: Gaussian versus lorentzian diagonal disorder, *Phys. Rev. B* **79**, 205121 (2009).

[116] F. Rossi and T. Kuhn, Theory of ultrafast phenomena in photoexcited semiconductors, *Rev. Mod. Phys.* **74**, 895 (2002).

[117] P. Michetti and G. C. La Rocca, Simulation of j-aggregate microcavity photoluminescence, *Physical Review B* **77**, 195301 (2008).

[118] G. M. A. V. Kavokin, J. J. Baumberg and F. P. Laussy, Microcavities, Oxford University Press (2006).

[119] J. Wainstain, C. Delalande, D. Gendt, M. Voos, J. Bloch, V. Thierry-Mieg, and R. Planel, Dynamics of polaritons in a semiconductor multiple-quantum-well microcavity, *Phys. Rev. B* **58**, 7269 (1998).

[120] D. G. Lidzey, D. D. C. Bradley, A. Armitage, S. Walker, and M. S. Skolnick, Photon-mediated hybridization of frenkel excitons in organic semiconductor microcavities, *Science* **288**, 1620 (2000), PMID: 10834836.

[121] D. V. Brumbaugh, A. A. Muenter, W. Knox, G. Mourou, and B. Wittmershaus, Singlet exciton annihilation in the picosecond fluorescence decay of 1, 1'-diethyl-2,2'-cyanine chloride dye j-aggregate, *Journal of Luminescence* **3132, Part 2**, 783 (1984).

[122] T. Forster, Intermolecular energy transfer and fluorescence .

[123] A. Amo, D. Sanvitto, F. P. Laussy, D. Ballarini, E. d. Valle, M. D. Martin, A. Lematre, J. Bloch, D. N. Krizhanovskii, M. S. Skolnick, C. Tejedor, and L. Via, Collective fluid dynamics of a polariton condensate in a semiconductor microcavity, *Nature* **457**, 291 (2009).

[124] R. Brckner, A. A. Zakhidov, R. Scholz, M. Sudzius, S. I. Hintschich, H. Frb, V. G. Lyssenko, and K. Leo, Phase-locked coherent modes in a patterned metal-organic microcavity, *Nat Photon* **6**, 322 (2012).

[125] P. Schouwink, H. Berlepsch, L. Dhne, and R. Mahrt, Dependence of rabi-splitting on the spatial position of the optically active layer in organic microcavities in the strong coupling regime, *Chemical Physics* **285**, 113 (2002).

[126] N. Takada, T. Kamata, and D. D. C. Bradley, Polariton emission from polysilane-based organic microcavities **82**, 1812 (2003).

[127] M. S. Bradley and V. Bulovi, Intracavity optical pumping of j-aggregate microcavity exciton polaritons, *Phys. Rev. B* **82**, 033305 (2010).

[128] J. Dintinger, S. Klein, F. Bustos, W. L. Barnes, and T. W. Ebbesen, Strong coupling between surface plasmon-polaritons and organic molecules in subwavelength hole arrays, *Phys. Rev. B* **71**, 035424 (2005).

[129] R. J. Holmes, S. Kna-Cohen, V. M. Menon, and S. R. Forrest, Strong coupling and hybridization of frenkel and wannier-mott excitons in an organic-inorganic optical microcavity, *Phys. Rev. B* **74**, 235211 (2006).

[130] Y. Zhang, G. M. Dalpian, B. Fluegel, S.-H. Wei, A. Mascarenhas, X.-Y. Huang, J. Li, and L.-W. Wang, Novel approach to tuning the physical properties of organic-inorganic hybrid semiconductors, *Phys. Rev. Lett.* **96**, 026405 (2006).

[131] C. Symonds, J. Bellessa, J. C. Plenet, A. Brhier, R. Parashkov, J. S. Lauret, and E. Deleporte, Emission of hybrid organic-inorganic exciton/plasmon mixed states **90**, 091107 (2007).

[132] S. R. Forrest, P. E. Burrows, E. I. Haskal, and F. F. So, Ultrahigh-vacuum quasiepitaxial growth of model van der waals thin films. II. experiment, *Phys. Rev. B* **49**, 11309 (1994).

[133] S. R. Forrest, Ultrathin organic films grown by organic molecular beam deposition and related techniques, *Chem. Rev.* **97**, 1793 (1997).

[134] J. Wenus, S. Ceccarelli, D. G. Lidzey, A. I. Tolmachev, J. L. Slominskii, and J. L. Bricks, Optical strong coupling in microcavities containing j-aggregates absorbing in near-infrared spectral range, *Organic Electronics* **8**, 120 (2007).

[135] P. Tsotsis, P. Eldridge, S. Tsintzos, N. Somaschi, Z. Hatzopoulos, P. G. Lagoudakis, and P. G. Savvidis, Polariton lasing in a strongly coupled hybrid dielectric mirror semiconductor microcavity, *UNPUBLISHED* (2013).

[136] M. Sich, D. N. Krizhanovskii, M. S. Skolnick, A. V. Gorbach, R. Hartley, D. V. Skryabin, E. A. Cerda-Mndez, K. Biermann, R. Hey, and P. V. Santos, Observation of bright polariton solitons in a semiconductor microcavity, *Nat Photon* **6**, 50 (2012).

[137] M. Saba, C. Ciuti, J. Bloch, V. Thierry-Mieg, R. Andr, L. S. Dang, S. Kundermann, A. Mura, G. Bongiovanni, J. L. Staehli, and B. Deveaud, High-temperature ultrafast polariton parametric amplification in semiconductor microcavities, *Nature* **414**, 731 (2001).

[138] P. G. Savvidis, C. Ciuti, J. J. Baumberg, D. M. Whittaker, M. S. Skolnick, and J. S. Roberts, Off-branch polaritons and multiple scattering in semiconductor microcavities, *Phys. Rev. B* **64**, 075311 (2001).

[139] L. I. Mandel'shtam, Group velocity in a crystal lattice, *Zh.Eksp.Teor.Fiz* **15**, 475 (1945).

[140] L. Brillouin, Wave Propagataion and Group Velocity, Academic Press, New York (1960).

[141] L. Silvestri, O. A. Dubovski, G. C. La Rocca, F. Bassani, and V. M. Agranovich, Negative refraction in crystals with spatial dispersion, *Nuovo Cimento C* **27**, 437 (2004).

[142] V. M. Agranovich and Y. N. Gartstein, Spatial dispersion and negative refraction of light, *Phys.-Usp.* **49**, 1029 (2006).

[143] M. Soljacic, S. G. Johnson, S. Fan, M. Ibanescu, E. Ippen, and J. D. Joannopoulos, Photonic-crystal slow-light enhancement of nonlinear phase sensitivity, *Journal of the Optical Society of America B* **19**, 2052 (2002).

[144] M. Soljacic and J. D. Joannopoulos, Enhancement of nonlinear effects using photonic crystals, *Nature Materials* **3**, 211 (2004).

[145] T. Baba, Slow light in photonic crystals, *Nature Photonics* **2**, 465 (2008).

[146] C. Monat, B. Corcoran, D. Pudo, M. Ebnali-Heidari, C. Grillet, M. Pelusi, D. Moss, B. Eggleton, T. White, L. O'Faolain, and T. Krauss, Slow light enhanced nonlinear optics in silicon photonic crystal waveguides, *IEEE Journal of Selected Topics in Quantum Electronics* **16**, 344 (2010).

[147] N. Somaschi, S. Tsintzos, D. Coles, D. G. Lidzey, Z. Hatzopoulos, P. G. Lagoudakis, and P. G. Savvidis, Superlinear polariton emission of hybrid organic-inorganic microcavities, *UNPUBLISHED* (2013).

[148] V. M. Agranovich and B. S. Toshich, Collective properties of frenkel excitons, *Soviet Phys. Jetp* **26**, 104 (1968).

[149] J. P. etraji, D. V. Kapor, and D. Mirjani, On the possibility of bose-einstein condensation and the superfluidity of frenkel excitons, *Physica Status Solidi B* **124**, 235239 (1984).

[150] M. A. Baldo, D. F. O'Brien, Y. You, A. Shoustikov, S. Sibley, M. E. Thompson, and S. R. Forrest, Highly efficient phosphorescent emission from organic electroluminescent devices, *Nature* **395**, 151 (1998).

[151] V. M. Agranovich, Y. N. Gartstein, and M. Litinskaya, Hybrid resonant OrganicInorganic nanostructures for optoelectronic applications, *Chemical Reviews* **111**, 5179 (2011).

[152] I. P. Kaminow, L. W. Stulz, E. A. Chandross, and C. A. Pryde, Photobleaching of organic laser dyes in solid matrices, *Appl. Opt.* **11**, 1563 (1972).

[153] H. Zoubi and G. C. La Rocca, Microscopic theory of nonlinear polariton interactions in strongly coupled hybrid organic-inorganic microcavities, *Phys. Rev. B* **76**, 035325 (2007).

[154] V. M. Agranovich and B. S. Toshich, *Zh. Eksp. Teor. Fiz.* **53**, 149 (1967).

[155] C. Ciuti, P. Schwendimann, and A. Quattropani, Theory of polariton parametric interactions in semiconductor microcavities, *Semiconductor Science and Technology* **18**, S279 (2003).

[156] G. H. Lodden and R. J. Holmes, Electrical excitation of microcavity polaritons by radiative pumping from a weakly coupled organic semiconductor, *Phys. Rev. B* **82**, 125317 (2010).

[157] G. H. Lodden and R. J. Holmes, Thermally activated population of microcavity polariton states under optical and electrical excitation, *Phys. Rev. B* **83**, 075301 (2011).

[158] N. Ollier, F. Natali, D. Byrne, P. Disseix, M. Mihailovic, A. Vasson, J. Leymarie, F. Semond, and J. Massies, Spectroscopy of a bulk GaN microcavity grown on si(111), *Jpn. J. Appl. Phys.* **44**, 4902 (2005).

[159] S. Coe, W.-K. Woo, M. Bawendi, and V. Bulovic, Electroluminescence from single monolayers of nanocrystals in molecular organic devices, *Nature* **420**, 800 (2002).

[160] L. Sapienza, A. Vasanelli, R. Colombelli, C. Ciuti, Y. Chassagneux, C. Manquest, U. Gennser, and C. Sirtori, Electrically injected cavity polaritons, *Phys. Rev. Lett.* **100**, 136806 (2008).

[161] P. Michetti and G. C. La Rocca, Polariton-polariton scattering in organic microcavities at high excitation densities, *Phys. Rev. B* **82**, 115327 (2010).

[162] M. Sheik-bahae, A. A. Said, and E. W. Van Stryland, High-sensitivity, single-beam n2 measurements, *Optics Letters* **14**, 955 (1989).